INVESTIGATION OF THE MECHANISM OF PHOSPHOTRIESTERASE: CHARACTERIZATION OF THE BINUCLEAR METAL ACTIVE SITE BY ELECTRON PARAMAGNETIC RESONANCE SPECTROSCOPY

A Dissertation

by

CYNTHIA RENEE SAMPLES

Submitted to the Office of Graduate Studies of
Texas A&M University
in partial fulfillment of the requirements for the degree of

DOCTOR OF PHILOSOPHY

December 2005

Major Subject: Chemistry

INVESTIGATION OF THE MECHANISM OF PHOSPHOTRIESTERASE: CHARACTERIZATION OF THE BINUCLEAR METAL ACTIVE SITE BY ELECTRON PARAMAGNETIC RESONANCE SPECTROSCOPY

A Dissertation

by

CYNTHIA RENEE SAMPLES

Submitted to the Office of Graduate Studies of
Texas A&M University
in partial fulfillment of the requirements for the degree of

DOCTOR OF PHILOSOPHY

Approved by:

Chair of Committee,	Victoria DeRose
Committee Members,	Frank Raushel
	Kim Dunbar
	Paul Fitzpatrick
Head of Department,	Emile Schweikert

December 2005

Major Subject: Chemistry

ABSTRACT

Investigation of the Mechanism of Phosphotriesterase: Characterization of the Binuclear Metal Active Site by Electron Paramagnetic Resonance Spectroscopy. (December 2005)

Cynthia Renee Samples, B.S., Harding University

Chair of Advisory Committee: Dr. Victoria DeRose

Phosphotriesterase (PTE) from *Pseudomonas diminuta* is a zinc metalloenzyme found in soil bacteria capable of organophosphate hydrolysis at rates approaching the diffusion controlled limit. Interest in PTE for degradation of chemical warfare agents and disposal of pesticides supports the need to understand the mechanism by which it performs hydrolysis. For further mechanistic clarity, this work will provide direct confirmation of the solvent bridge identity and the protonated species resulting in loss of catalytic identity. Inhibitor and product binding to the metal center will also be addressed; as well as the evaluation of the catalytic activity of Fe(II)-substituted PTE.

This work has determined that the Mn/Mn-PTE electron paramagnetic resonance (EPR) spectrum exhibits exchange coupling that is facilitated through a hydroxide bridge. Protonation of the bridging hydroxide results in the loss of the exchange coupling between the two divalent cations and the loss of catalytic activity. The reversible protonation of the bridging hydroxide has an apparent pK_a of 7.3 based upon changes in the EPR spectrum of Mn/Mn-PTE with alterations in pH. The pH-rate profile for the hydrolysis of paraoxon by Mn/Mn-PTE shows the requirement of a single function group that must be unprotonated with a pK_a of 7.1. The comparable pK_a values are proposed to result from the protonation of the same ionizable species.

The effects of inhibitor and product binding on the magnetic properties of the metal center and the hydroxyl bridge are investigated by accessing new EPR spectral

features. This work concludes that the binding of inhibitor occurs at the metal center and results in an increase of non-bridged hydroxyl species. These results, in conjunction with kinetic and crystallographic data, suggest that substrate binding via the phosphoryl oxygen at the β-metal weakens the hydroxyl bridge coordination to the β-metal. This loss of coordination would increase the nucleophilic character of the bridge, and binding of the substrate to the metal center would result in a stronger nucleophile for hydrolysis.

Lastly, Fe(II) binding and activation of apoenzyme is evaluated under anaerobic conditions. This work concludes Fe/Fe-PTE is not catalytically active, but can bind up to 2 equivalent Fe(II) ions per active site.

DEDICATION

This dissertation is dedicated to the women who have laid the foundation which made this work possible: Myrtie Biggs, Edna Heavrin, and Sue Samples

TABLE OF CONTENTS

CHAPTER Page

LIST OF FIGURES

FIGURE Page

FIGURE Page

LIST OF TABLES

CHAPTER I

INTRODUCTION: PHOSPHOTRIESTERASE*

Phosphotriesterase (PTE) is an enzyme capable of hydrolyzing organophosphates which are used as chemical warfare agents and pesticides. The use of organophosphates as pesticides has proven to be effective in the fight against crop damage as well as diminishing the threat of human diseases like malaria by controlling the mosquito population (*1*). While the use of organophosphates has far reaching positive aspects in maintaining our quality of life, the aftermath of these toxins must be addressed. The contamination of the water supply and leakage from mass storage of chemical warfare agents are potential threats to human health. Therefore, the removal of threats posed by the accumulation of organophosphates is of high priority. Nature has provided a response to the existence of these organophosphates in the form of the enzyme phosphotriesterase. The ability to investigate, interpret, understand, and utilize this enzyme belongs to the researcher that recognizes its importance. Much research and understanding of PTE has been accomplished in the past four decades, but there is still more to know.

This chapter highlights the present knowledge of this enzyme and provides a basis for the mechanistic questions addressed and answered in the chapters to follow.

This thesis follows the style of *Biochemistry*.

.

Electron paramagnetic resonance spectroscopy (EPR) is the major technique applied in this investigation of the binuclear active site of Mn(II)-substituted PTE. The theory and use of EPR in the study of binuclear enzymes will be discussed in Chapter II.

Organophosphates contribute to half of all pesticides, mostly insecticides, used in the United States (*1*). The majority of organophosphates are used for major crops such as corn and cotton. Other uses involve pesticides for fruits, vegetables, livestock, and lawn care. Despite the usefulness of pesticides, they reportedly cause 500,000 illnesses and 20,000 deaths worldwide per year are reportedly due to pesticides (*1*). The overstimulation of nerve cells initiated by organophosphates can result in symptoms ranging from nausea, dizziness, and confusion to respiratory paralysis and death. Detoxification and bioremediation of organophosphates is of great interest.

Organophosphates were first synthesized by Clermont in 1854 (*2*). Their use as insecticides was established by Schrader in 1937, with the more toxic organophosphates such as soman, tabun, and sarin, developed for chemical warfare usage during World War II. Ironically, some organophosphates have a therapeutic use for treatment of glaucoma and Alzheimer's disease (*2*). Organophosphates are toxic to most cellular organisms due their ability to inhibit acetylcholinesterase. Hydrolysis of organophosphates by acetylcholinesterase results in the formation of a stable phosphorylated-enzyme intermediate that renders the enzyme catalytically dead. The addition of oxime, such as pralidoxime (2-PAM), can regenerate the enzyme by nucleophilic attack on the phosphorus center by the oxime resulting in cleavage of the phosphoester-enzyme bond. Conformational change of the enzyme may occur upon 'aging', resulting in the irreversible bonding of the phosphate in the active site. PTE serves in detoxification by hydrolysis of organophosphates before they inhibit acetylcholinesterase. PTE can potentially be used for detoxification of organophosphate

poisoning, bioremediation of land, destruction of chemical warfare agent stockpiles, and as biosensors for organophosphate detection.

PTE was isolated in the 1970s from two unrelated strains of soil bacteria. The enzyme isolated from *Flavobacterium* was identified from rice patties in the Philippines that had been treated with the insecticide diazinon (*3*). PTE isolated from *Pseudomonas diminuta* was identified upon hydrolysis of parathion (*4*). The gene encoding PTE, opd (organophosphate-degrading), was found in extra chromosomal plasmids in both bacteria. It was subcloned into *E. coli* for extensive characterization of this enzyme. PTE can hydrolyze organophosphates at rates approaching diffusion-controlled limits; however, the natural substrate for this enzyme as not been identified. The enzymatic hydrolysis of the insecticide paraoxon, diethyl p-nitrophenyl phosphate, is presented in Scheme 1. Paraoxon is the best substrate known for PTE, to date.

Scheme 1

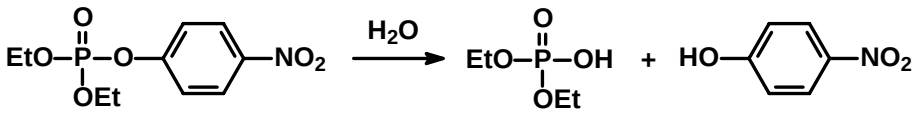

PTE is a member of the aminohydrolase superfamily. Other members of this superfamily that contain dinuclear metal centers include dihydroorotase and urease. Members of this superfamily have active sites located within a TIM-barrel motif (Figure 1) and the reactions they catalyze occur by nucleophile attack at a phosphorus or carbonyl center by an activated solvent molecule. A conserved H-X-H motif also characterizes this superfamily. The high resolution X-ray crystal structure of Zn-containing enzyme reveals that PTE is a homodimeric protein containing an active site with two divalent metal ions embedded within a $(\beta/\alpha)_8$-barrel motif (*5*). The α-metal ion is ligated by His-55, His-57, and Asp-301 while the β-metal ion is coordinated to His-

201 and His-230 as illustrated in Figure 2. The two metal ions are bridged by a carboxylated Lys-169 and a molecule from solvent that is either hydroxide or water. The α-metal has a ligand coordination number of five and is considered to be more buried within the protein. The β-metal is more solvent-exposed and acquires additional water ligands, resulting in penta- or hexa-coordination, depending upon the identity of the bound metal (*5*).

The crystal structure of Zn-PTE with diisopropyl methyl phosphonate, an inhibitor of PTE, shows the phosphoryl oxygen of the inhibitor 2.5 Å from the β-metal site (Figure 3) (*6*). Two other crystal structures of Zn-PTE complexed with the inhibitors triethyl phosphate and diethyl 4-methyl benzyl phosphonate also revealed the phosphoryl oxygens to be ~3.4 Å from the β-metal (*6, 7*). These structures suggest binding of substrate would occur at the β-metal site via the phosphoryl oxygen of triester phosphates.

Apoenzyme can be produced upon addition of 1,10-*o*-phenanthroline or EDTA and is found to be kinetically inactive (*8, 9*). Studies on the self-assembly of the metal active site have established that the formation of the carboxylated lysine precedes metal binding (*9*). Carbon dioxide reacts with Lys-169 to form the bridging carboxylated lysine. Catalytic activity increases linearly upon addition of metal up to 2 equivalent after which it remains constant. The binding of metal was found to be a synergistic process in which the second metal bound has the greater binding affinity for the active site (*9*).

Both metals are required for full catalytic activity. Zinc is the apparent native metal ion, but substantial catalytic activity is observed with the Co-, Cd-, Mn-, or Ni-substituted forms of the enzyme (*8*). Kinetic studies have shown that the kinetic constants, k_{cat} and k_{cat}/K_m, are dependent upon the identity of the specific metal ions

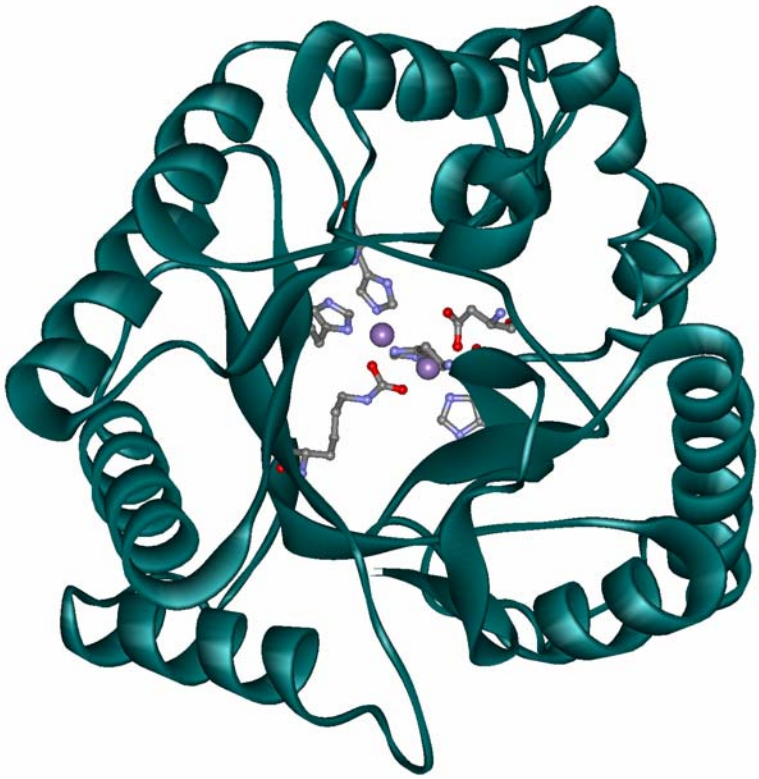

Figure 1. Crystal structure of phosphotriesterase highlighting the active site metals and residues within the $(\alpha/\beta)_8$-TIM barrel motif. Coordinates taken from PDB file 1I0B.

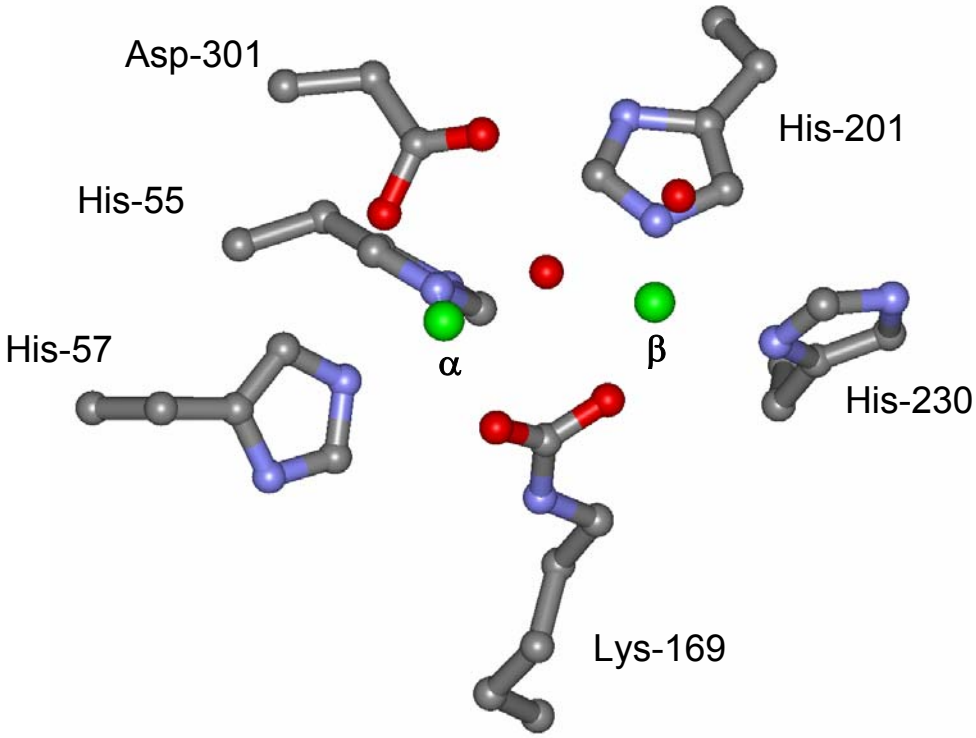

Figure 2. Binuclear active site of Zn/Zn-substituted phosphotriesterase. Coordinates taken from PDB file 1HZY.

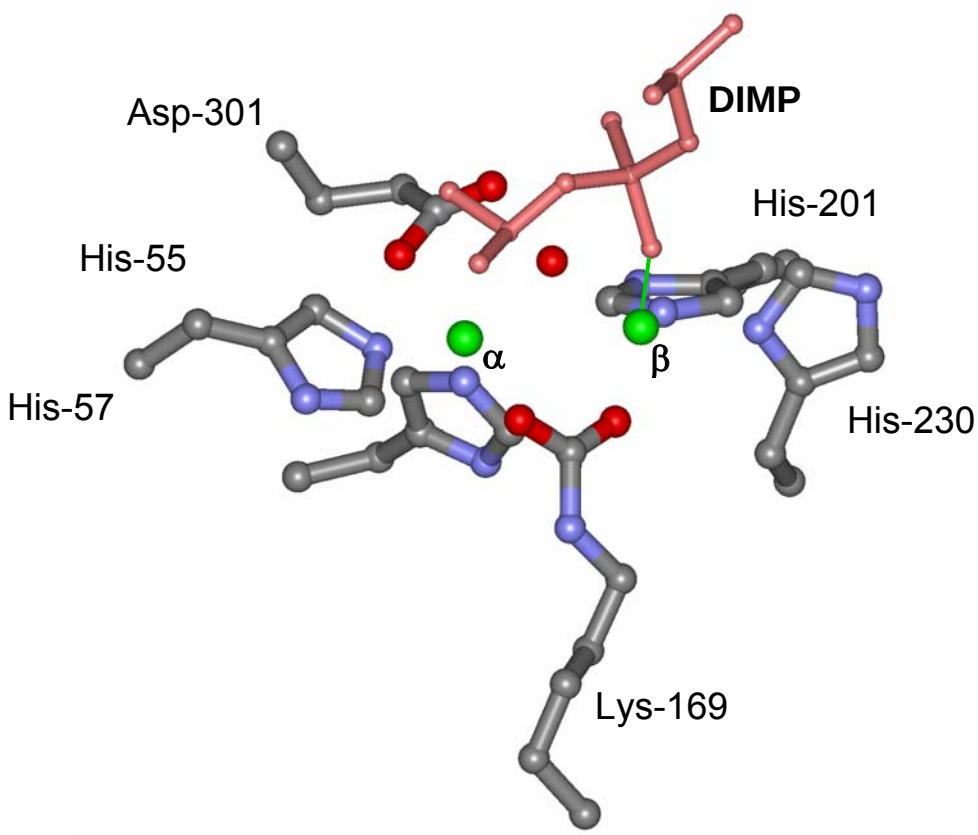

Figure 3. Binuclear active site of Zn/Zn-substituted phosphotriesterase with the inhibitor diisopropyl methyl phosphonate (DIMP) present. The phosphoryl oxygen of DIMP is 2.5 Å from the β metal. The distance of 2.5 Å is highlighted in green. Coordinates taken from PDB file 1EZ2.

Table 1. Kinetic parameters for the hydrolysis of paraoxon with various metal-substituted phosphotriesterases. Kinetic values taken from Omburo *et al.* (*10*).

Metals	K_m (μM)*	k_{cat} (s^{-1})*	k_{cat}/K_m (M^{-1} s^{-1})*	pK_a for k_{cat}*
Co/Co	200	7800	4.0×10^7	6.5
Cd/Cd	400	4600	1.2×10^7	8.1
Zn/Zn	90	2400	2.7×10^7	5.8
Mn/Mn	80	1800	2.2×10^7	7.0
Ni/Ni	150	6000	3.9×10^7	7.4

*** Paraoxon**

within the active site (*8*). The kinetic parameters are shown in Table 1. All catalytically active metal substitutions had efficiencies approaching the diffusion control limit. While Co(II)-substituted PTE had the greatest activity, Zn(II) exhibited the greatest affinity for the active site and was capable of displacing all other metals previously bound. The crystal structure of the hybrid metal-substituted enzyme, Zn/Cd-PTE, demonstrated the preference of the Zn(II) for the α-metal site over the β-metal site (*5*). The hybrid was confirmed by ^{113}Cd NMR to be a single mixed-metal hybrid (*11*).

The loss of catalytic activity is observed at lower pH, and a pK_a value associated with this loss of activity is dependent upon the identity of the active site metal (Table 1). The pH-rate profiles indicate protonation of a single species. This species is associated with the enzyme since the substrate does not ionize in the range of pK_a values determined for different metal substitutions. These values fall within the expectations associated with water coordinated to two metals (*12*). The pK_a value for Zn/Cd-PTE is 6.2. This value nears the Zn/Zn-PTE value of 5.9 rather than the Cd/Cd-PTE value of 8.0. The pK_a value for the hybrid reflects the dominant influence of the α-metal on the protonated species (*13*). Asp-301 was mutated to both an alanine and asparagine residue. No variance in the pK_a from the wild type enzyme was observed for either mutant and confirmed protonation did not occur at the Asp-301 residue (*13*).

A mechanism for organophosphate hydrolysis by PTE has been proposed (Figure 4) (*13*). The initiation of hydrolysis occurs upon binding of substrate at the β-metal site in the presence of the hydroxyl bridge of the resting enzyme. Binding at this site is supported by the crystal structure of diisopropyl methyl phosphonate in the active site of PTE (*6*). Nucleophilic attack at the phosphorus center, by the activated hydroxyl, results in cleavage of the phosphoester bond of phosphate triesters and release of the leaving group. Attack occurs by a S_N2-type mechanism resulting in net inversion of

configuration at the phosphorus center. The enzymatic hydrolysis of the Sp-isomer of *O*-ethyl *O*-*p*-nitrophenyl phenylphosphonothioate (EPN) in oxygen-18-labeled water resulted in the ^{18}O-labeled Sp-isomer of the thiophosphonic acid product demonstrating the net inversion of stereochemistry at the phosphorus center (*14*). The reactivity of the hydroxyl bridge is enhanced by proton transfer to Asp-301. After the proton from the attacking hydroxide is transferred to Asp 301, it is further shuttled to His-254, Asp233, and bulk solvent. After release of the leaving group, the proposed bridging phosphate product is released and the hydroxyl bridge is formed by incoming solvent.

The minimal reaction mechanism for PTE is shown in Scheme 2. Formation of the enzyme-substrate complex is reversible. The hydrolysis of substrate to product is an irreversible process represented as k_3 or the chemical event. The irreversible release of each of the two products is combined as k_5 and referred to as the physical event of dissociation.

Scheme 2

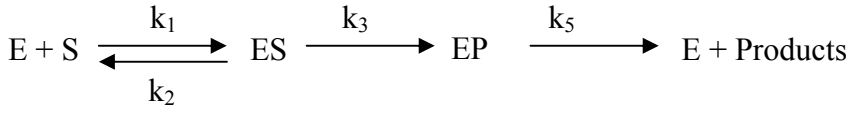

The rate limiting step in this mechanism was determined using substrates in which only the pK_a of the leaving group phenol was varied (*15, 16*). The Brønsted plot of this experiment determined that the rate limiting step changes from the physical event of dissociation to the chemical event of hydrolysis as the pK_a of the leaving group increases. Substrates with leaving groups having low pK_a values can be utilized to report on the diffusion-limited events, while those with higher pK_a values give information on events that influence the ease and mode of bond cleavage of substrate. Paraoxon, with a leaving group pK_a of 7.1, is considered a fast substrate with a k_{cat} of

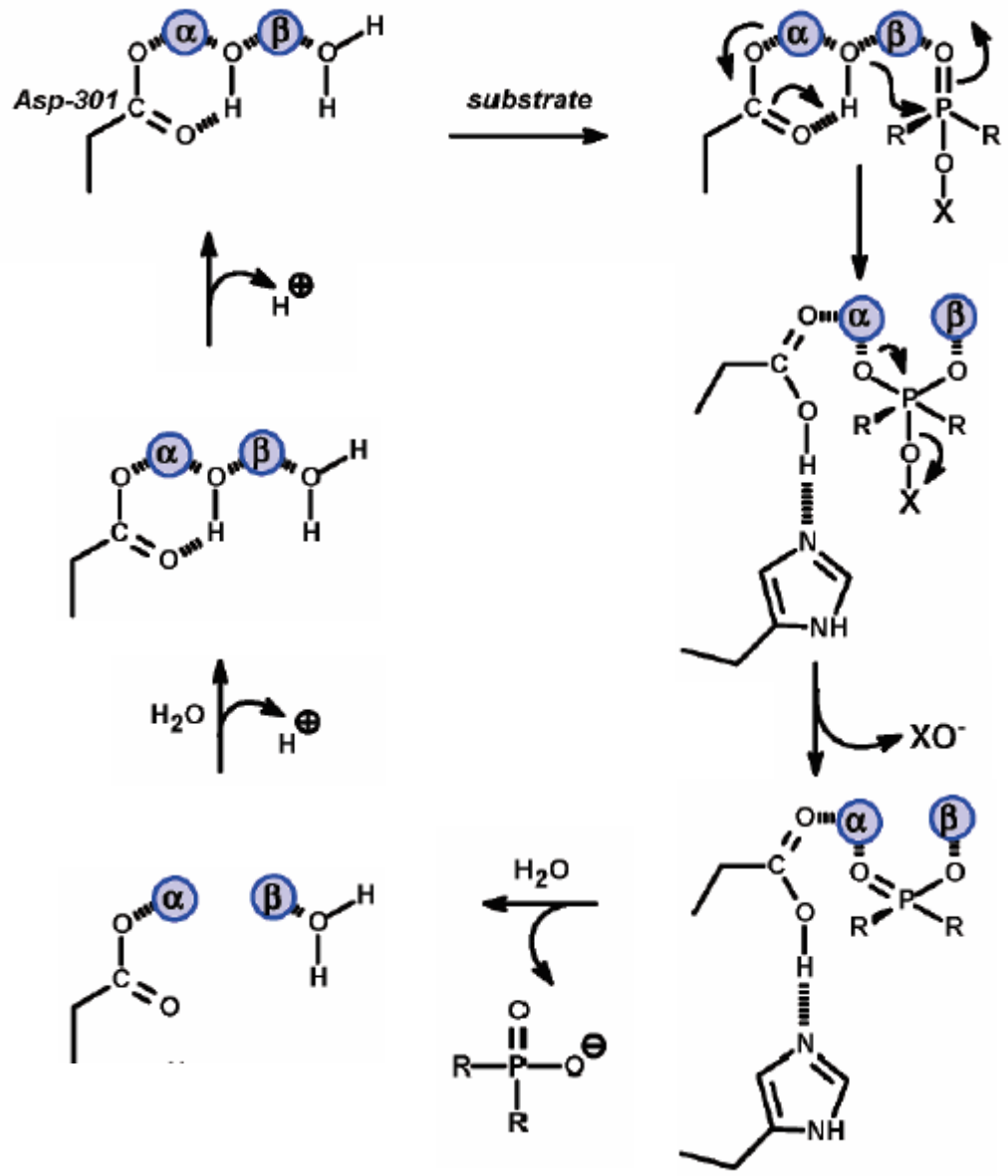

Figure 4. Proposed catalytic mechanism for the hydrolysis of paraoxon by phosphotriesterase. (Reproduced with permission from Aubert *et al.* (*13*). Copyright 2004 Am. Chem. Soc.)

2300 s^{-1} and a k_{cat}/K_m of 7 x 10^{-7} $M^{-1}s^{-1}$ for Zn/Zn-PTE. Diethyl p-chlorophenyl phosphate is a slow substrate with a leaving group pK_a of 9.4, a k_{cat} of 0.36 s^{-1} and a k_{cat}/K_m of 220 $M^{-1}s^{-1}$ for Zn/Zn-PTE (*13*, *15*). Since the β-value obtained from the Brønsted plot was large relative to non-enzymatic hydrolysis by KOH, a substantial portion of charge is assigned to the leaving group phenol resulting in a transition state that looks more like product.

The influence of the active site metal or metals on the phosphorus center of substrate during hydrolysis was investigated by observing the hydrolysis of two slow substrates, diethyl p-chlorophenyl phosphate and diethyl p-chlorophenyl thiophosphate, by Zn/Zn-PTE, Zn/Cd-PTE, and Cd/Cd-PTE. The hydrolysis of the thiophosphate triester was enhanced over the hydrolysis of the phosphate triester for the three different metal-substituted enzymes (*13*). The enhancement in kinetic ratio of k_{cat}/K_m for the thiophosphate triester over the phosphate triester was greatest when Cd(II) was substituted for Zn(II). The interaction of substrate with the divalent cation polarizes the phosphorus-oxygen (sulfur) bond increasing the electrophilicity at the phosphorus center and ease of bond cleavage upon nucleophilic attack by the hydroxyl bridge.

Proton transfer following substrate hydrolysis was investigated using the diffusion control limited substrate paraoxon. The crystal structure of PTE shows the oxygen of Asp-301 to be 2.3 Å from the oxygen of the hydroxyl bridge. Asp-301 is thought to be protonated after nucleophilic attack of substrate by the bridging hydroxide. The residue is proposed to receive the proton formerly serving as the hydrogen of the hydroxyl bridge. Removal of the hydrogen bonding interaction and potential for proton transfer was achieved with the mutants D301A and D301N. A loss of 1-2 orders of magnitude in catalytic activity was observed for these mutants and supports the enhanced reactivity of the hydroxyl bridge with Asp-301 present as well as its potential

involvement in proton shuttling. His-254 has been shown to be catalytically essential by chemical modification and mutagenesis studies (*17, 18*). The ε2 nitrogen of His-254 resides 2.7 Å from the oxygen of Asp-301, and the δ1 nitrogen of His-254 is 2.9 Å from the oxygen of Asp-233. This residue is readily available to serve in shuttling the proton from the hydroxyl bridge to bulk solvent. Both His-254 and Asp-233 were separately mutated to alanine and asparagine resulting in a loss of 1-2 orders of magnitude in catalytic activity for His-254 mutants and diminished activity for Asp-233 mutants. Mutagenesis studies confirm the involvement of Asp-301, His-254, and Asp-255 in proton shuttling to bulk solvent. Removal of the proton from the active site might be expected since protonation of the leaving group phenol is not needed because its pK_a is below the pH of the assay.

PTE has a broad substrate specificity that can be attributed to the lack of electrostatic and hydrogen bonding interactions between substrate and enzyme at the active site (*7*). However, a selective orientation for substrate binding is observed in crystal structures for enzyme-inhibitor complexes. Three binding pockets, shown in Figure 5, within the active site were differentiated from the orientation of the inhibitor diethyl 4-methylbenzyl phosphonate in Zn/Zn-PTE (*7*). The large binding pocket is designated by His-254, His-257, Leu-271, and Met-317. The small binding pocket is lined by Gly-60, Ile-106, Leu-303, and Ser-308. The leaving group binding pocket contains Trp-131, Phe-132, Phe-306, and Tyr-309. Various paraoxon analogues in which one of the ethyl functional groups was replaced with methyl, isopropyl, or phenyl were hydrolyzed to determine stereoselectivity by PTE (*19*). Hydrolysis of these analogues ranged from 18,000 s^{-1} to 220 s^{-1} for Co/Co-PTE. A 100-fold preference for the S_p-isomer over the R_p-isomer was observed for all of the paraoxon analogues.

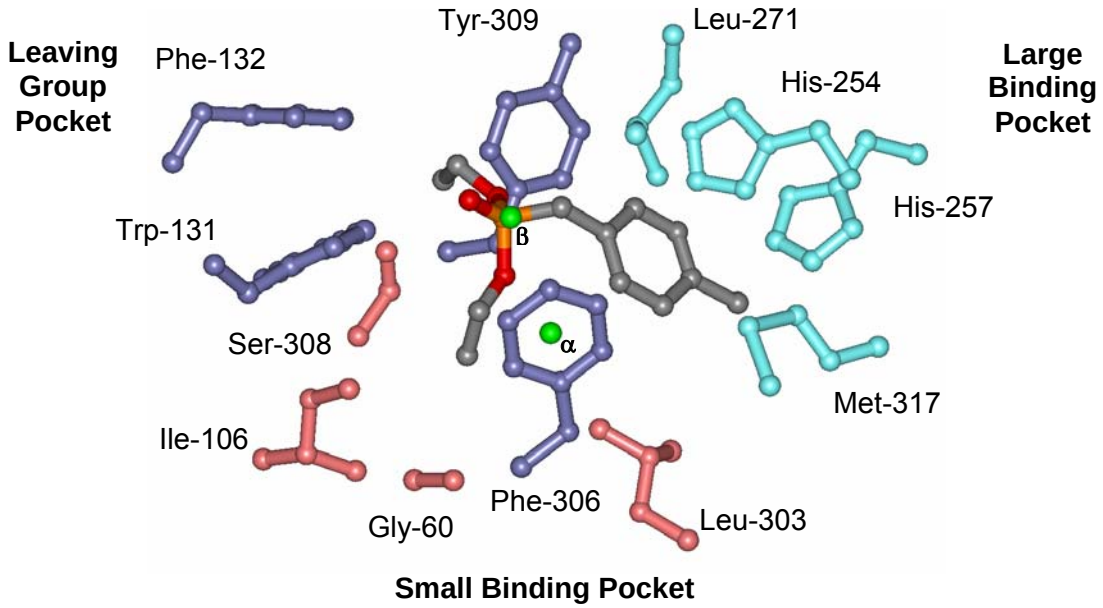

Figure 5. The substrate binding pocket of phosphotriesterase with the inhibitor diethyl 4-methyl benzyl phosphonate bound. The small binding pocket (shown in salmon) is designated by residues Gly-60, Ile-106, Ser-308, and Leu-303. The large binding pocket (shown in aqua) is lined by residues His-254, His-257, Met-317, and Leu-271. The leaving group pocket (shown in blue) contains residues Phe-132, Trp-131, Phe-306, and Tyr-309. Coordinates taken from PDB file 1DPM.

However, the more toxic isomer of these analogues was the R_p-isomer. Among the chemical warfare agents, the more toxic stereoisomer for sarin is the S_p-isomer; while the R_p-isomer is predicted to be the preferred isomer by PTE based on the stereochemical preference for the R_p-isomer of the sarin analogue, diisopropyl methyl phosphonate (*19*).

The discrepancy between the more toxic isomer and the preferred isomer hydrolyzed by PTE sparked the interest in manipulating the binding site pockets in order to adjust the stereoselective preference of the enzyme. Site directed mutagenesis in these binding pockets has resulted in enhancement, relaxation, and reversal of stereoselectivity. Enhanced stereoselectivity was observed for the mutant G60A, which is located in the small binding pocket (*20*). The substrate methyl phenyl p-nitrophenyl phosphate was used to determine the catalytic activity for wild type enzyme and mutants demonstrating adjusted stereoselective preference. A ratio of 90:1 in favor of the Sp- verses Rp-stereoisomer of this substrate was determine for wild type enzyme, while the G60A mutant had an enhancement of 13,000:1 in favor of the Sp-stereoisomer. This was accomplished by a 100-fold reduction in the k_{cat}/K_m for the Rp-isomer. This enhancement apparently resulted from a decrease in the size of the small binding pocket. The relaxation of stereoselectivity was accomplished using the mutant I106G located in the small binding pocket (*21*). This mutation increased the size of the small binding pocket. The preference of Sp- to Rp-stereoisomer was reduced to a ratio of 1.7:1, in favor of the Sp-isomer. Relaxation was achieved by a 100-fold increase in the k_{cat}/K_m of the Rp-stereoisomer. A reversal of stereoselective preference was accomplished using the quadruple mutant, I106G/F132G/H257Y/F308G (*21*). An increase in the size of the small binding pocket coupled with a decrease in the size of the large binding pocket resulted from these four mutations. The reversal of stereoselective preference was

reflected in the ratio of 1:190 in favor of the Rp-isomer. These three mutants demonstrate the flexibility and ease in manipulation of the active site to be custom designed for stereoselectivity according to the toxin of interest to be hydrolyzed.

Extensive investigation of the mechanism for organophosphate hydrolysis by PTE has successfully divulged the chemistry utilized by this enzyme for efficient organophosphate degradation. Mutagenesis of this enzyme has demonstrated PTE's versatility in broad and targeted toxin degradation as a method for removal of unwanted organophosphates. For further mechanistic clarity, this work will provide direct confirmation of the solvent bridge identity and the protonated species resulting in loss of catalytic identity. Substrate and product binding to the metal center will also be addressed.

CHAPTER II

EPR THEORY AND APPLICATION FOR BIMETALLOENZYMES*

Electron paramagnetic resonance spectroscopy (EPR) is extensively used in the study of biomolecules that utilize paramagnetic metal ions. The advantage in employing EPR spectroscopy in the investigation of metalloproteins is in the ability to exclude the relatively vast expanse of biomolecule and monitor the environment of the metal site. For metalloenzymes, this technique is useful for characterizing catalytic metal cores and monitoring changes in metal concentration, oxidation, coordination, and coupling of multiple metals in efforts to elucidate a mechanism of catalysis.

EPR utilizes the magnetic character of unpaired electrons and its sensitivity to change in environment. An unpaired electron generates a magnetic field since it is a charged particle with an intrinsic angular momentum, spin. The spin of an electron within an orbital has two possible orientations expressed as M_s values of +1/2 and -1/2. The energies associated with these orientations are degenerate in the absence of an external field. In the presence of an applied magnetic field, the magnetic moment of the electron aligns with or against the field resulting in non-degenerate spin states in which the M_s -1/2 state is the ground state (Figure 6). The influence of a magnetic field on the energy of an unpaired electron is called the Zeeman interaction. The Hamiltonian

---

*Reproduced in part with permission from Khangulov, S. V., Pessiki, P. J., Barynin, V. V., Ash, D. E., and Dismukes, G. C. Determination of the metal ion separation and energies of the three lowest electronic states of dimanganese (II,II) complexes and enzymes: catalase and liver arginase. *Biochemistry 34*, 2015-25. Copyright 1995 American Chemical Society.

*Reproduced in part with permission from Reczkowski, R. S., and Ash, D. E. EPR evidence for binuclear Mn(II) centers in rat liver arginase. *J. Am. Chem. Soc. 114*, 10992-10994. Copyright 1992 American Chemical Society.

equation describing this interaction is shown in equation 1. In the following equation, **H** is the Hamiltonian operator, g_e is the Zeeman free electron value of 2.0023, β_e is the electron Bohr magneton value of 9.27×10^{-21} erg·gauss^{-1}, $\mathbf{B_o}$ is the applied field, and **S** is the spin operator.

$$\mathbf{H} = \beta_e \mathbf{B_o} \cdot g_e \cdot \mathbf{S} \quad (1)$$

An additional term can be added to the Hamiltonian that takes into account the influence of the magnetic field on the nuclear moment of nuclei with spin. This interaction is referred to as the nuclear Zeeman interaction and is shown in equation 2, where g_n is the nuclear g-value, β_n is the nuclear Bohr magneton value of 5.05×10^{-24} erg·gauss^{-1}, and **I** is the nuclear spin operator. The nuclear Zeeman interaction adjusts the energies of the spin states a thousand fold less than the electron Zeeman interaction, and therefore, is considered negligible in comparison to its electron counterpart.

$$\mathbf{H} = \beta_e \mathbf{B_o} \cdot g_e \cdot \mathbf{S} - \beta_n \mathbf{B_o} \cdot g_n \cdot \mathbf{I} \quad (2)$$

EPR spectroscopy measures the absorbance of radiation by unpaired electrons in an applied magnetic field. A paramagnetic sample is placed between two magnets and irradiated with microwave radiation. In a classical EPR experiment, the microwave frequency is held constant and the magnetic field strength is increased over time. The energy difference between the two spin states of the unpaired electron increases with increased field strength (Figure 6). A transition is observed in the EPR spectrum when the applied microwave radiation, ν, is in resonance with the energy difference between the two spin states. The absorption of energy results in a change in spin orientation from the ground state to the excited state and meets the required criteria of $\Delta M_S = \pm 1$ for an EPR transition. The energy difference between states is shown in equation 3 and the condition for resonance is expressed in equation 4. In the following equation, E is energy, h is plank's constant, and ν is the applied frequency.

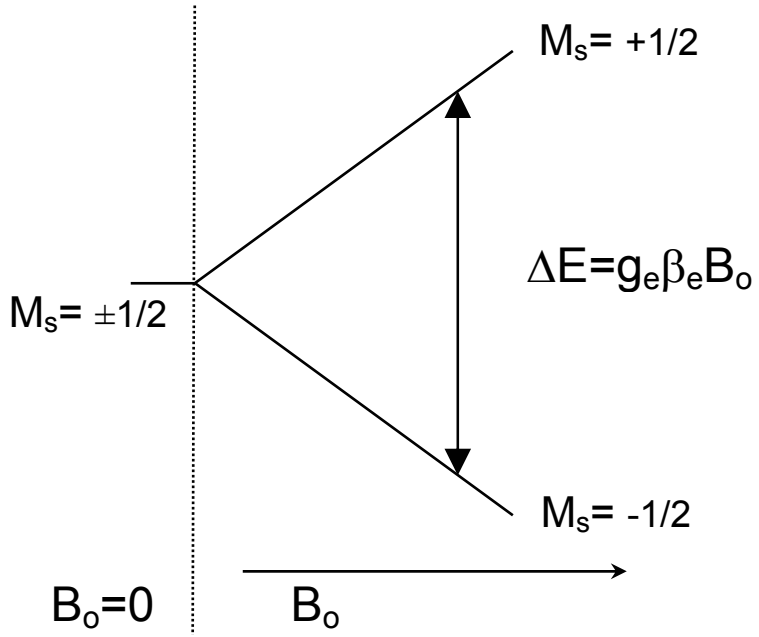

Figure 6. Zeeman splitting for a S = 1/2 system. The ΔM_s = ± 1 transition is shown.

$$\Delta E = E_{+1/2} - E_{-1/2} = +\tfrac{1}{2} g_e \beta_e B_o - (-\tfrac{1}{2} g_e \beta_e B_o) \quad (3)$$

$$\Delta E = g_e \beta_e B_o = h\nu \quad (4)$$

The absorbance of radiation by the paramagnetic species is an absorption spectrum; however, the first derivative of the spectrum is recorded for technical reasons. Small changes which may be subtle in the absorbance spectrum are highlighted in the first derivative spectrum. The most commonly used frequency is 9 GHz and is referred to as X-Band frequency. A commonly used higher frequency is 35 GHz or Q-Band frequency. Use of higher frequency requires a stronger magnet in order to observe the absorption due to resonance described in equation 4.

Transition metals having more than two unpaired electrons produce multiple-line EPR spectra reflecting the transitions between multiple spin states. For a S = 5/2 spin system, the Zeeman interaction removes the degeneracy of the M_s ±5/2, ±3/2, ±1/2 spin states and, EPR transitions between these states are observed with a $\Delta M_s = \pm 1$. When unpaired electrons reside in a symmetric environment, all transitions are of equal energy; and therefore, are excited at the same field position. Only one transition will be observed in the EPR spectrum with the signal amplitude representing the sum all five transitions. The energy diagram for a S = 5/2 system with high symmetry is shown in Figure 7.

The interaction between nuclei with spin and the unpaired electron is called hyperfine interaction. Coupling of the nuclear and electron magnetic moments adjusts the energies associated with the spin states. The magnitude of this interaction is dependent on the overlap between the electron and nuclei and the alignment of their spin orientations relative to one another. An additional term is added to the Hamiltonian to describe the hyperfine interaction (equation 5), in which **I** is the nuclear spin operator

and the magnitude of the interaction is represented by the hyperfine splitting constant, a, expressed in gauss.

$$\mathbf{H} = \beta_e \mathbf{B_o} \cdot g_e \cdot \mathbf{S} + \mathbf{S} \cdot a \cdot \mathbf{I} \quad (5)$$

There are 2I + 1 possible orientations, M_I values, for a given nucleus, and therefore, there are 2I + 1 resulting hyperfine interactions per electron spin orientation, M_s value. The magnitude of this coupling is less than that observed for the Zeeman interaction, therefore, the energy of each electron spin state is split into 2I + 1 energy levels. The energy diagram of the S = 5/2 spin states for a Mn(II) ion in Figure 8 shows a new set of spin states resulting from the coupling of the ^{55}Mn nuclei, I = 5/2 (100% abundance), with the five unpaired electrons of the Mn(II) ion. Allowed EPR transitions are accompanied by $\Delta M_s = \pm 1$ and $\Delta M_I = 0$. The energy diagram in Figure 8 shows 5 allowed transitions which are further split into 5 sets of 6 transitions. A total of 30 allowed transitions are possible. In an EPR spectrum, hyperfine coupling splits each line in the spectrum into the appropriate number of 2nI + 1 hyperfine lines, where n is the number of identical nuclei. The separation between these lines is dependent upon the strength of the interaction between the nuclei and electron. The g-value associated with a set of hyperfine splittings is determined from the magnetic field position in the center of the splittings. The EPR spectrum of $Mn(H_20)_6^{2+}$ is shown in Figure 9. There are 6 lines separated by 90 G with a g-value of ~2. Although 30 transitions are predicted from the energy diagram due to the high symmetry of this metal ion, each set of 6 transitions are equivalent in energy and so only 1 set of six transitions is observed in the spectrum.

The g_e-value for an unpaired electron in a magnetic field is 2.0023 and is observed in an X-band EPR spectrum at ~3350 G. However, multiple g-values are often observed within an EPR spectrum due to spin-orbit coupling and spin-spin (dipole-dipole) interactions. The movement of an unpaired electron in a molecular orbital

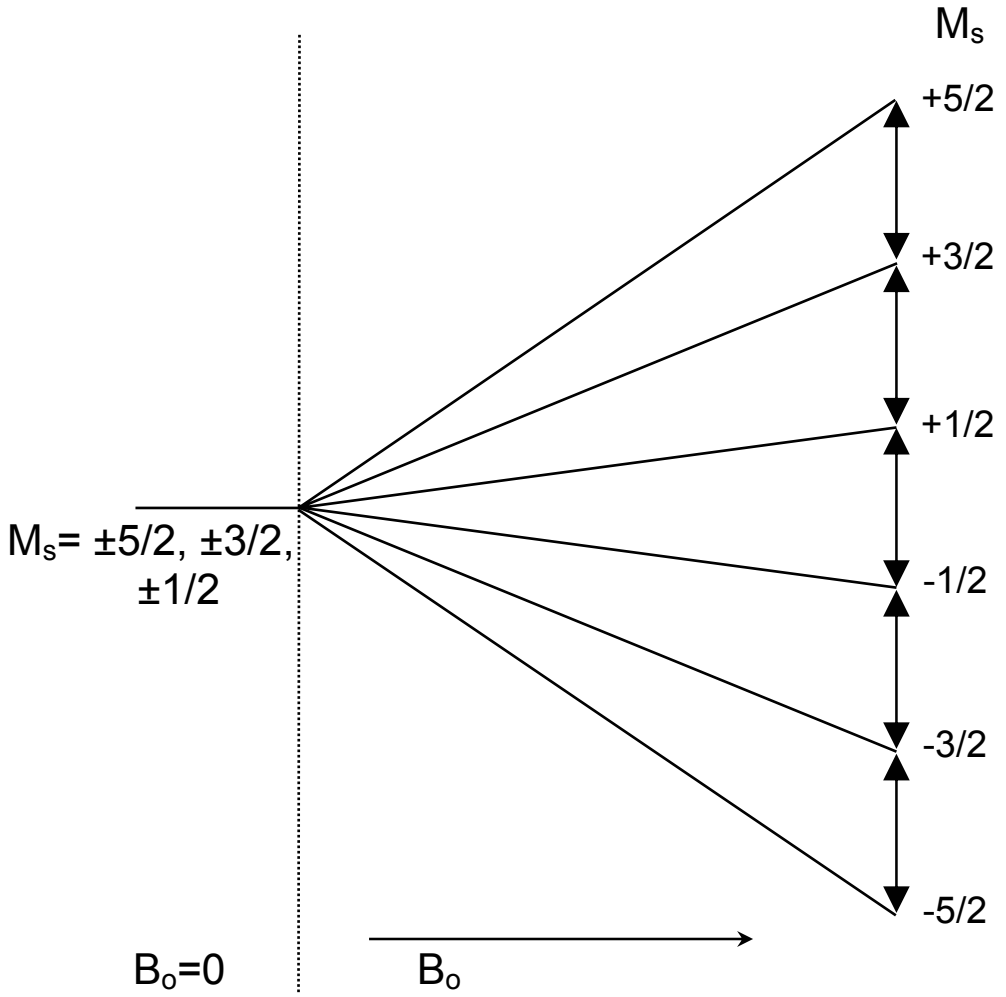

Figure 7. Zeeman splitting for a S = 5/2 system. All transitions are degenerate and designated with arrows between spin levels.

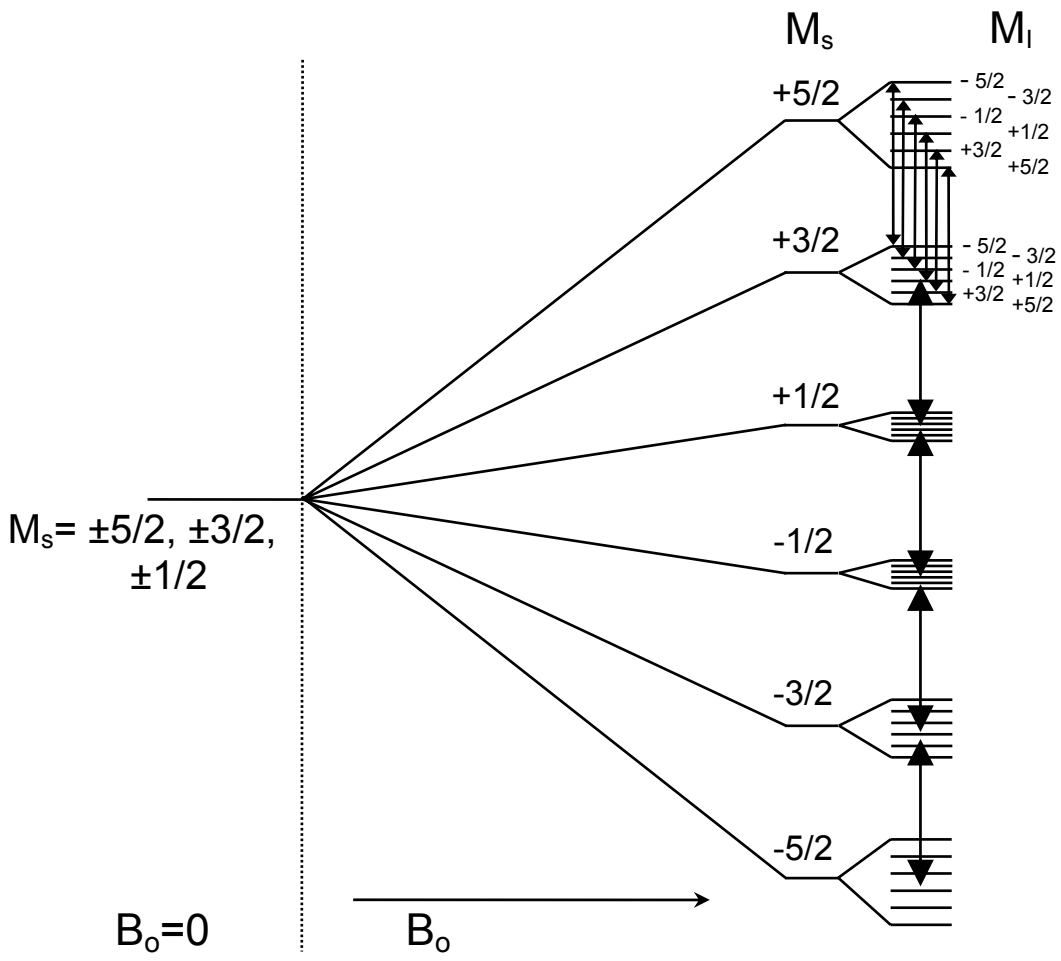

Figure 8. Zeeman and hyperfine splitting of the M_s levels of a S = 5/2, I = 5/2 system. $\Delta M_s = \pm 1$ and $\Delta M_I = 0$ allowed transitions are shown for the six transitions between the M_s states. There are 30 total allowed transitions but only six different energies due to degeneracy.

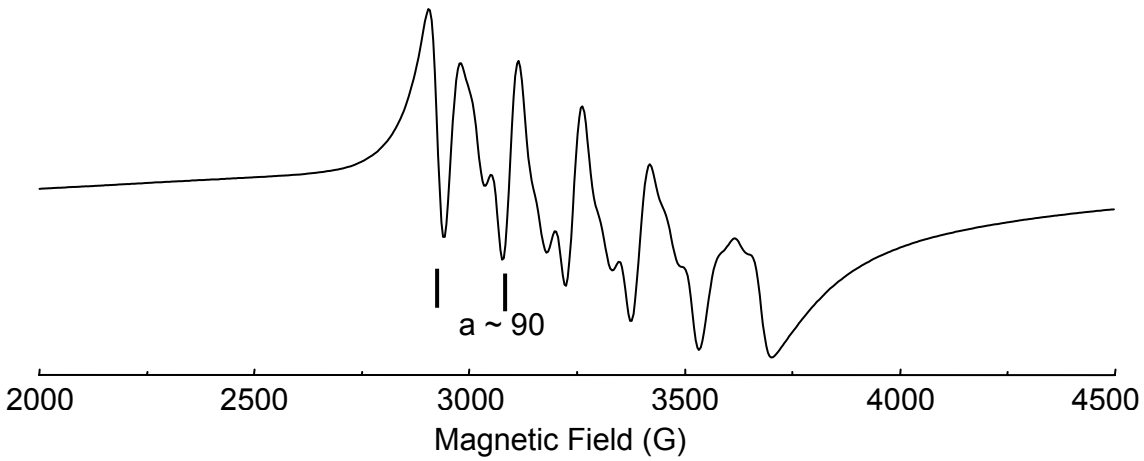

Figure 9. The EPR spectrum of $Mn(H_20)_6^{2+}$ exhibits hyperfine coupling with the Mn nuclei, I = 5/2. The six lines are separated by 90 G with a g-value of ~2. Anisotrophy in zero-field results in forbidden transitions observed in between the six allowed transitions.

produces orbital angular momentum. Spin-orbit coupling is the result of the addition of the orbital angular momentum vector to the spin angular momentum vector creating a new net magnetic moment of the unpaired electron. The new net moment depends on the direction and magnitude of each vector. Since the orbital angular momentum is determined by a wavefunction it has directionality, or anisotropy. The electron has a new magnetic moment in which the magnitude and, potentially, the direction of the vector has changed. As a result, the energy associated with the Zeeman interaction has changed producing a new g-value and a change in the vector alignment with the field produces a directional or anisotropic g-value, (g_x, g_y, g_z). Transition metal ions typically have ground states with orbital angular momentum that is partially quenched by the crystal field provided by their ligands. Only a small perturbation on the energy of the M_s values occurs lending to the treatment of first row transition metal ions as spin only systems. The octahedral high spin Mn(II) ion has a ground state with no orbital angular momentum. Some spin-orbit coupling is achieved due to the mixing of the excited state in with the ground state providing access to orbital angular momentum. Again, this is a minor perturbation due to quenching of spin-orbit coupling by the crystal field.

Anisotropy also arises from dipole-dipole interactions between electrons residing in neighboring orbitals. Coupling of the magnetic moments of two unpaired electrons removes the degeneracy of the M_s spin levels in the absence of the magnetic field. The removal of M_s degeneracy is referred to as zero-field splitting and can have a substantial effect on the EPR spectrum. This coupling is dependent upon the distance and alignment of the electron spin dipoles. In metal-ligand coordination, the orbital overlap influences the extent of dipole-dipole interaction in zero-field. When the coordination environment around a paramagnetic metal is no longer symmetrical, the dipolar coupling experienced by the unpaired electron(s) with the surrounding ligand dipoles can vary in

the x-, y-, and z-directions. The energy associated with zero-field splitting is expressed in the Hamiltonians shown in equation 6 and 7. The two zero-field parameters D, the axial splitting parameter, and E, the rhombic splitting parameter, give an idea of the distortion in symmetry about the metal center. When $S_x = S_y$, the system is purely axial and E = 0.

$$\mathbf{H} = \beta \mathbf{B_o} \cdot g_e \cdot \mathbf{S} + \mathbf{S} \cdot a \cdot \mathbf{I} + \mathbf{S} \cdot D \cdot \mathbf{S} \quad (6)$$

$$\mathbf{H}_{ZF} = D[\mathbf{S}_z^2 - \tfrac{1}{3}\mathbf{S}(\mathbf{S}+1) + E/D(\mathbf{S}_x^2 - \mathbf{S}_y^2)] = \mathbf{S} \cdot D \cdot \mathbf{S} \quad (7)$$

The removal of M_s degeneracy is illustrated in the energy diagram in Figure 10 with the separation of M_s levels designated with the axial splitting parameter, D. Zero-field perturbation on the EPR spectrum for $Mn(H_20)_6^{2+}$ is manifested as forbidden transitions observed as shoulders on the 6-line hyperfine transition shown in Figure 9. The mixing of excited and ground state wavefunctions due to zero-field splitting results in a forbidden transition with $\Delta M_s = \pm 1$ and $\Delta M_I = \pm 1$.

The metal center of binuclear metalloenzymes typically has low to no symmetry (*22*). The manifestations of lower symmetry in the EPR spectrum from paramagnetic metals include anisotropy in g- and a-values and the observation of forbidden transitions in the low field region and are attributed to zero-field splitting. As the symmetry is lowered to axial and rhombic, anisotropic g-values (g_x, g_y, and g_z) are assigned to represent the magnetic environment experienced by the electron in different directions. The Hamiltonian is expressed for effective g-values on the principle axes, and all energy expressions are applied individually to each principle direction. Anisotropy is not observed in the EPR spectrum for small molecules in liquid samples since the orientation of the molecule is randomized due to tumbling in solution and is thereby averaged out. In a single crystal, the magnetic environment in each direction can be observed by rotating the crystal onto the x-, y-, and z-axis. In a frozen liquid, the molecule resides in

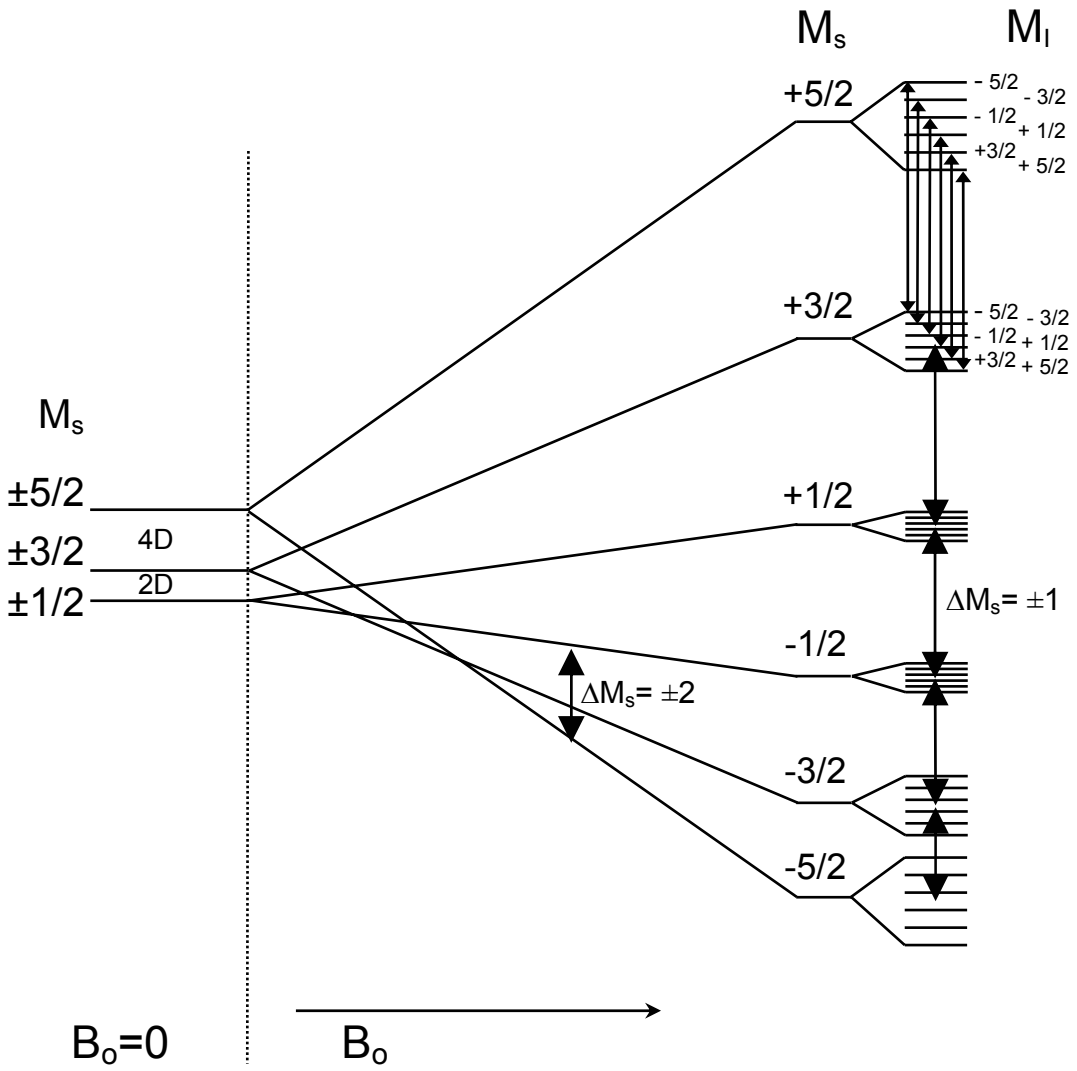

Figure 10. Zeeman and hyperfine splitting for a S = 5/2 system with zero-field anisotropy. Transitions are not degenerate. $\Delta M_s = \pm 1$, $\Delta M_I = 0$ designate allowed transitions and $\Delta M_s = \pm 2$ designate accessible forbidden transitions due to zero-field splitting, D.

all orientations and the sum of the orientations is observed in the spectrum. This is also referred to as a powder spectrum since it looks as though a crystal was ground to powder. Only one g-value with a derivative peak is observed in an isotropic spectrum and reflects high symmetry at the paramagnetic center. When the symmetry is lowered to axial symmetry, two g-values, $g_{\parallel}(g_z)$ and $g_{\perp}(g_x = g_y)$, are observed with a spectrum as an absorption peak and a derivative peak. Rhombic symmetry results in a spectrum with a positive absorption peak, derivative peak, and a negative absorption peak with g_x, g_y, and g_z centered at each peak. Anisotropy is observed in the hyperfine splitting constant as a_x, a_y, and a_z. The hyperfine splittings are centered at the g-value for the corresponding direction.

The effect of zero-field splitting on the EPR spectrum can result in observable forbidden $\Delta M_s \pm 2$ transitions. For small zero-field splittings, where $h\nu > D$, low lying M_s levels are close in energy and a double quantum transition is possible (Figure 10). Forbidden transitions typically fall in the low field region of the EPR spectrum and are referred to as half-field transitions. Other than their position in the field, these transitions have the same fine and hyperfine structure as the allowed transitions from the same spin manifold. A common method employed to confirm a half-field transition as forbidden is by increasing the spectrometer frequency. The intensity of a forbidden transition is proportional to D/H_o^2. These transitions are not observed with large zero-field splittings since the energy of excitation is less than the energy difference between the M_s levels, $h\nu << D$.

When two paramagnetic metal ions are within close proximity, the magnetic moments of the metals couple resulting in the delocalization of electron spin between the two metals and is referred to as exchange coupling. Since the magnitude of the hyperfine interaction is dependent on the distance between the electron and nuclei, the

hyperfine splitting observed in the EPR spectrum for a single metal ion is reduced by half upon delocalization of spin between two metal ions. This reduction is utilized in the identification of exchange coupled binuclear metal centers from their mononuclear metal ion counterpart. For a binuclear Mn(II) system the hyperfine interaction results in line splittings of 45 G verses 90 G observed for mononuclear Mn(II) ions. A reduction in line separation is also accompanied by an increase in the number of lines observed in the EPR spectrum, in accordance with hyperfine splitting of 2nI + 1 lines. Six lines are observed for mononuclear Mn(II), while 11 lines are expected for a symmetric exchange coupled system.

Coupling facilitated through the orbitals of a single atom ligand bridge is known as superexchange coupling. When coupling is experienced as two dipoles through space, it is called dipolar exchange coupling. The total spin for the coupled metal center is the sum of the individual metal spin states. A spin ladder for the coupled system contains spin states that range from $|S_1 + S_2|$, $|S_1 + S_2 - 1|$, $|S_1 + S_2 - 2|$, to $|S_1 - S_2|$. If the ground state is achieved when the magnetic moments of the two metals are spin-paired, the coupling is defined as antiferromagnetic, with $J < 0$. A spin ladder in which the ground state arises from coupled parallel spin moments describes a ferromagnetically coupled metal center, with $J > 0$. The spin ladder for an antiferromagnetically coupled binuclear Mn(II)-center with the effects of zero-field splitting is shown in Figure 11. The Hamiltonian for the energy associated with exchange coupling is shown in equation 8. S_1 and S_2 are the spin states for metal 1 and 2, respectively. The magnitude of the coupling is represented by the exchange coupling constant, J (cm^{-1}).

$$\mathbf{H}_{Ex} = -2J(\mathbf{S}_1 \cdot \mathbf{S}_2) \tag{8}$$

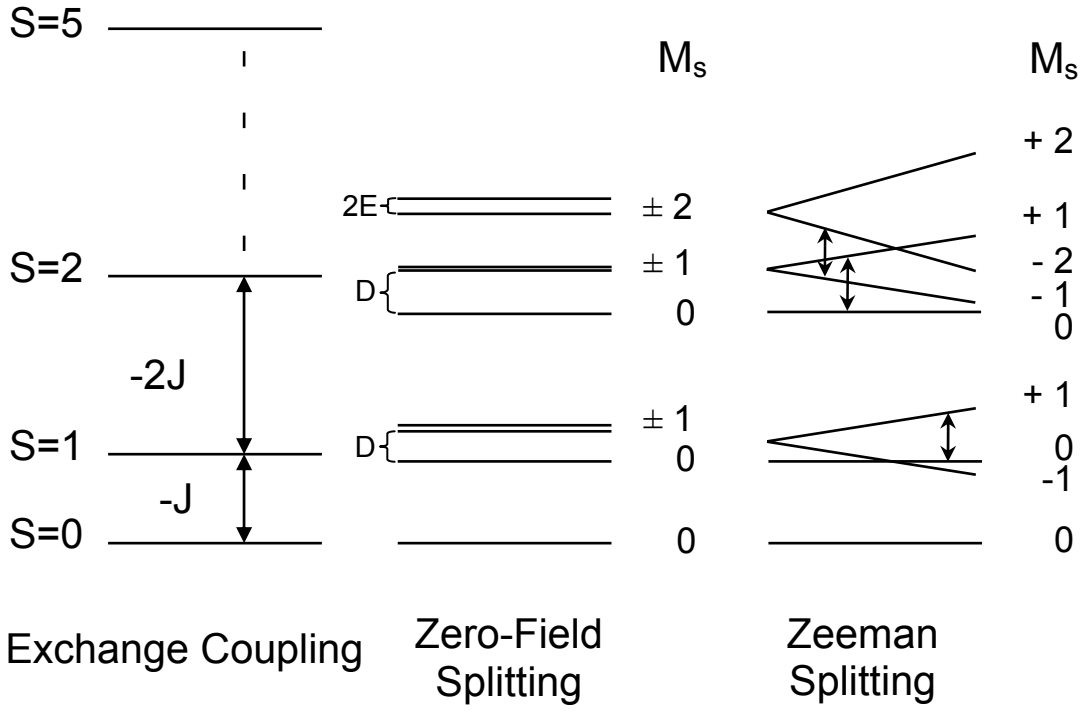

Figure 11. Antiferromagnetic exchange coupling for two S = 5/2 species resulting in a spin ladder with a total S = 5. Zero-field and Zeeman splittings are included in the energy diagram. Arrows designate some of the allowed transitions from this spin ladder, $\Delta M_s = \pm 1$. Zero-field splitting parameters, D and E, are shown.

The energy difference between spin manifolds within the ladder is expressed as the J-value and reflects the magnitude of coupling between the metals. When the exchange coupling is greater than the Zeeman interaction ($J > g_e\beta H_o$), all observed EPR transitions result from within each spin manifold. The extent of exchange coupling is dependent upon the distance between the two metals, and for superexchange, the identity of the bridging ligand and the extent of orbital overlap between the bridge and metal ions. The complete Hamiltonian for the description of a binuclear metal center is shown in equation 9.

$$\mathbf{H} = -2J\mathbf{S}_1 \cdot \mathbf{S}_2 + \mathbf{S}_1 \cdot D \cdot \mathbf{S}_2 + \sum_{i=1}^{2}[\mathbf{S}_i \cdot D_i \cdot \mathbf{S}_i + g\beta_e H_o \cdot \mathbf{S}_i + g_n\beta_n H_o \cdot \mathbf{I}_i + a_i \mathbf{S}_i \cdot \mathbf{I}_i] \quad (9)$$

Weak coupling results in easily accessed excited states via thermal population. The EPR signal arising from these spin states is readily populated and depopulated by small changes in temperature. The signal therefore exhibits a strong temperature dependence. Strong coupling resulting in large energy differences between spin states accounts for a lack of observable signal at liquid helium temperatures for antiferromagnetically coupled systems with a S = 0 ground state. The Boltzmann population equation expressing the relationship between the temperature, exchange coupling, and spin state population is shown in equation 10. The signal intensity of a transition is proportional to the population of spin state from which it arises.

$$\text{Population}_S = \frac{(2S+1)\exp([-2J(S(S+1) - S_1(S_1+1) - S_2(S_2+1))]/kT)}{\sum_S (2S+1)\exp([-2J(S(S+1) - S_1(S_1+1) - S_2(S_2+1))]/kT)} \quad (10)$$

The J-value can be determined by magnetic susceptibility or by fitting the temperature dependence of the signal intensity in the EPR spectrum with the Boltzmann equation. All paramagnetic species exhibit a temperature dependent magnetism referred to as the

Curie dependence. The signal intensity is multiplied by the temperature at which it is collected in order remove this dependence. EPR spectra for exchange coupled metal centers are typically collected near liquid helium temperature in order to observe signal from low lying excited states and to decrease broadening due to relaxation via thermal motion.

The EPR spectrum of the binuclear metal center of Mn(II)-substituted phosphotriesterase is shown in Figure 12. The complex spectrum has anisotropic g-values which reflect the rhombic symmetry of the metal center. Multiple sets of the 11-line hyperfine splittings separated by 45 G are observable at 10 K and are centered on their respective g-values. The close proximity of g-values results in the overlap of hyperfine lines so that each set of eleven is not distinguished readily. The exchange coupling constant for the binuclear Mn(II) center was determined by monitoring the temperature dependence of the hyperfine signal intensity. The J-value of -2.7 ± 0.2 cm^{-1} was determined for the S = 2 spin state (*23*). Simulation of this spectrum resulted in a D-value of -0.056 cm^{-1} and E-value of -0.0067 cm^{-1} (*23*). D-values of $|0.03|$ cm^{-1} and $|0.1|$ cm^{-1} are considered small and large values for D, respectively (*24*).

Enzyme systems with binuclear metal centers similar to the active site in PTE are shown in Figure 13. All of the enzymes shown in Figure 13 are bridged by at least one solvent bridge and one carboxylate bridge. PTE, urease, and dihydroorotase exhibit the less common carboxylated lysine residue as the second bridge for the metal center. The more common use of an aspartate or glutamate as a carboxylate bridge is observed in arginase, Mn-catalase, and lambda protein phosphatase. With the exception of Mn-catalase, these enzymes are hydrolases in which a bridging solvent molecule is typically proposed as the nucleophile for hydrolysis of substrate (*13*, *25-28*). The binuclear metal centers, shown in Figure 13, serve to accommodate substrate binding, increase the

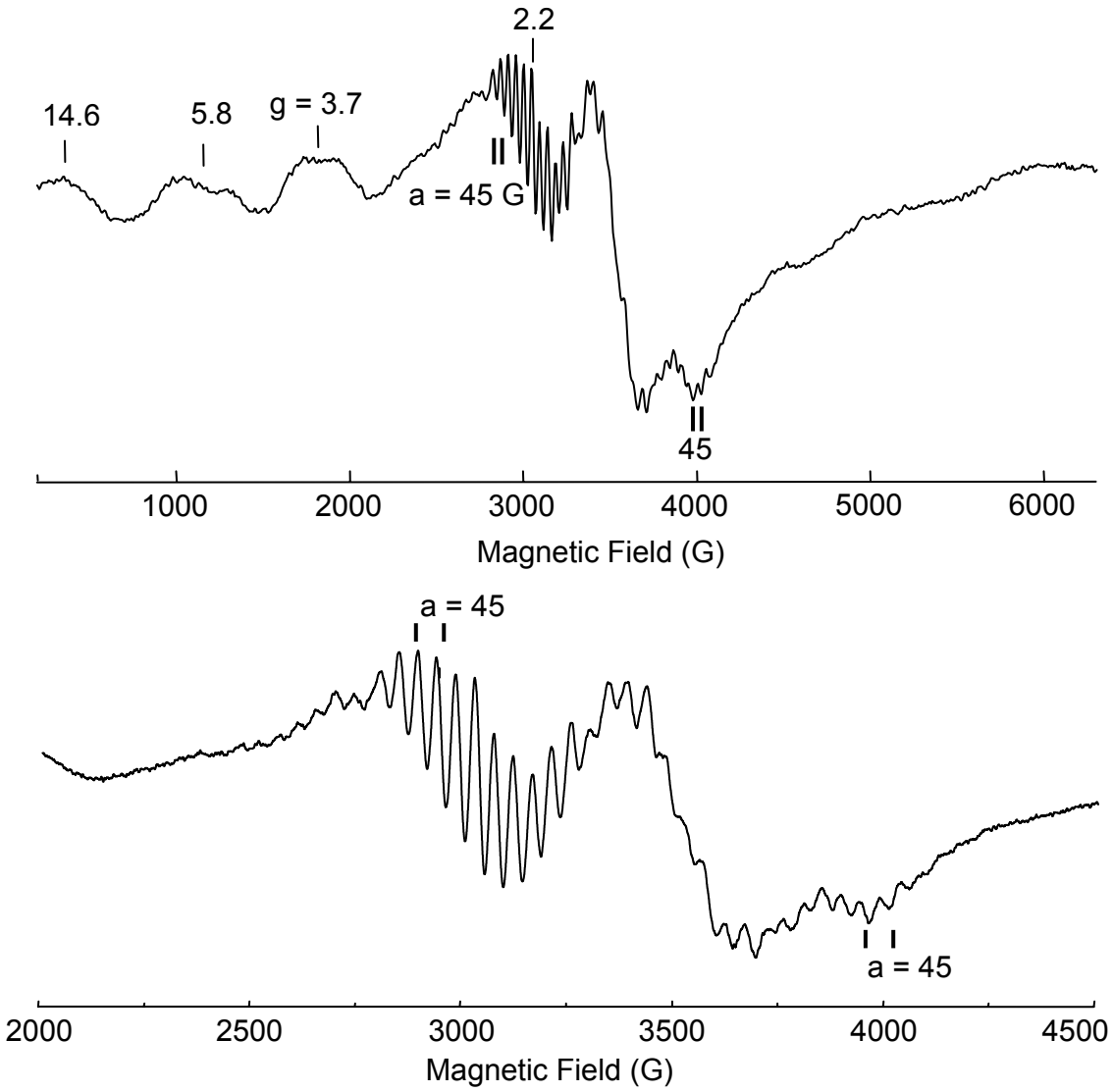

Figure 12. The EPR spectrum for the binuclear metal center of Mn(II)-substituted phosphotriesterase. Top spectrum: 200 G to 6100 G field strength. Bottom spectrum: Expansion of 2000 G to 4500 G region. The spectrum contains multiple g-values and hyperfine splittings of 45 G.

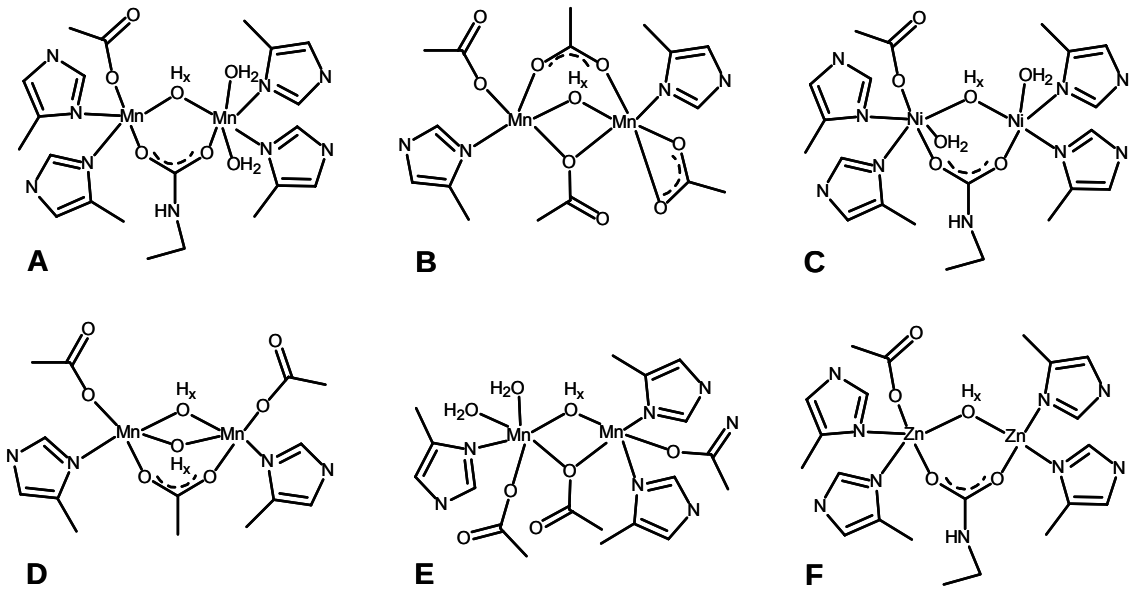

Figure 13. Metal centers of some bimetalloenzymes. (A) Mn/Mn-PTE (*5*) (B) arginase (*33*) (C) urease (*34*) (D) Mn-catalase (*33*) (E) Lambda protein phosphatase (*27*) (F) dihydroorotase (*30*). These structures have been adapted from the references indicated in parentheses.

electrophilicity of the substrate, and activate solvent to a more nucleophilic hydroxide (*13, 25-30*).

The EPR spectra for arginase, reduced manganese catalase, and lambda protein phosphatase exhibit the same features as observed for Mn(II)-substituted PTE (Figure 14) (*31, 32*). Analysis of the temperature dependence of the binuclear signal for arginase and Mn-catalase resulted in J-values of -2.0 ± 0.5 cm^{-1} for arginase and -5.6 ± 0.1 cm^{-1} for manganese catalase with phosphate present (*31*). Simulations of these EPR spectra determined D-values of -0.056 cm^{-1} and -0.051 cm^{-1} for arginase and manganese catalase, respectively (*31*). PTE, arginase, and Mn-catalase exhibit similar weak exchange coupling between the two metals and similar zero-field parameters which reflect a metal center with low symmetry (*23, 31, 33*). Figure 13 presents well characterized binuclear enzymes with active sites similar to PTE, but does not encompass all binuclear hydrolases investigated via EPR. Phosphatases and aminopeptidases, such as purple acid phosphatase and methionine aminopeptidase, have also been characterized using EPR for Fe-, Mn-, and Co- substituted enzymes (*35-39*).

EPR spectroscopy provides insight into the function of metals within an enzyme as structural, mechanistic, or both. Identification of metal, metal valence, metal clusters, and concentration can be determined by g-values, a-values, and integration of signal. Changes in ligand identity and coordination due to substrate, product, or small molecule binding at the metal center can be monitored by changes in the D-value. Modification or loss of metal bridging ligands upon change in pH, hydrogen bonding, or electrostatic interactions can be monitored by changes in the J-value. The magnitude of the J-value can also assist in bridge identification (*31*). Titration of metal with apoenzyme can provide metal binding affinities (*24, 40*). Comparison of wild type and mutant spectra

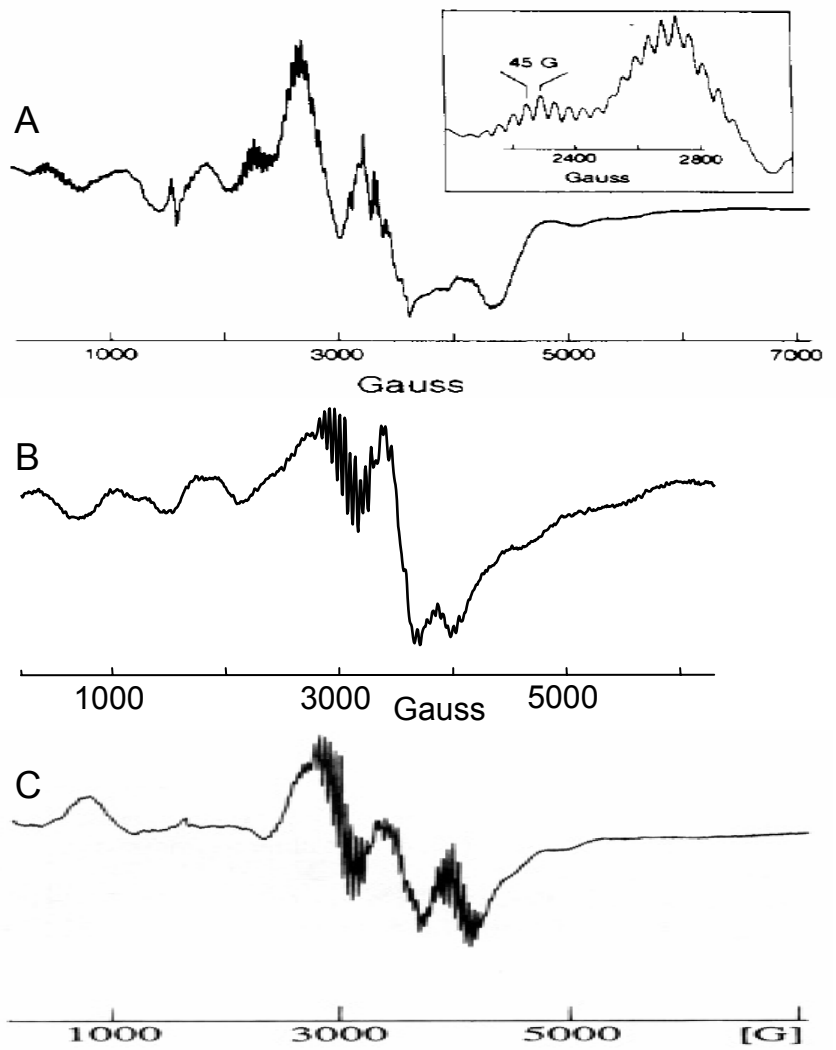

Figure 14. X-band EPR spectra for arginase, Mn/Mn-PTE, and Mn-catalase. (A) Arginase EPR spectrum at 20 K; Inset: Expansion of 2200-2800 G (Reproduced with permission from reference (*32*). Copyright 1992 Am. Chem. Soc.) (B) Mn/Mn-PTE EPR spectrum at 10 K (C) Mn-catalase EPR spectrum at 9 K (Reproduced with permission from reference (*31*). Copyright 1995 Am. Chem. Soc.)

can assist in identification of metal binding site preference within a binuclear active site (*41*).

EPR spectroscopy is a useful tool in the mechanistic evaluation of metalloenzymes. It has a well-developed theory for interpretation of often complicated spectra from unique enzyme environments. The ability to probe a metal center encased within a vast protein body arises from the intrinsic angular momentum of an unpaired electron (spin).

CHAPTER III

IDENTIFICATION OF THE HYDROXIDE BRIDGE IN THE ACTIVE SITE OF PHOSPHOTRIESTERASE*

Phosphotriesterase (PTE) catalyzes the hydrolysis of a wide range of organophosphate esters, including agricultural pesticides and chemical warfare agents (*42-44*). The enzyme has been isolated from soil bacteria, but the natural substrate for PTE is not known. PTE is a member of the amidohydrolase superfamily, which also includes urease, dihydroorotase and approximately 30 other enzymes of known specificity (*45*).

The crystal structure of Zn/Zn-PTE reveals a homodimeric protein with the active site located within a $(\beta/\alpha)_8$-barrel motif (*5*). The active site contains two divalent metal cations in unique environments. The more protein buried α-metal ion is coordinated by His-55, His-57, and Asp-301, and the solvent exposed β-metal ion is coordinated to His-201, His-230, and one or two water ligands depending upon the identity of the metal (Figure 15). The two metal ions are bridged by a carboxylated Lys-169 and a molecule from solvent that is either hydroxide or water. Both metals are required for full catalytic activity and bind in pairs to the active site (*10, 46*). Zinc is the apparent native metal ion, but substitution with Co, Cd, Mn, or Ni results in substantial catalytic activity (*10*). Kinetic studies have shown that the kinetic constants, k_{cat} and k_{cat}/K_m, are dependent upon the identity of the specific metal ions within the active site.

---

*Reproduced with permission from Samples, C. R., Howard, T., Raushel, F. M., and DeRose, V. J. Protonation of the binuclear metal center within the active site of phosphotriesterase. *Biochemistry 44*, 11005-13. Copyright 2005 American Chemical Society.

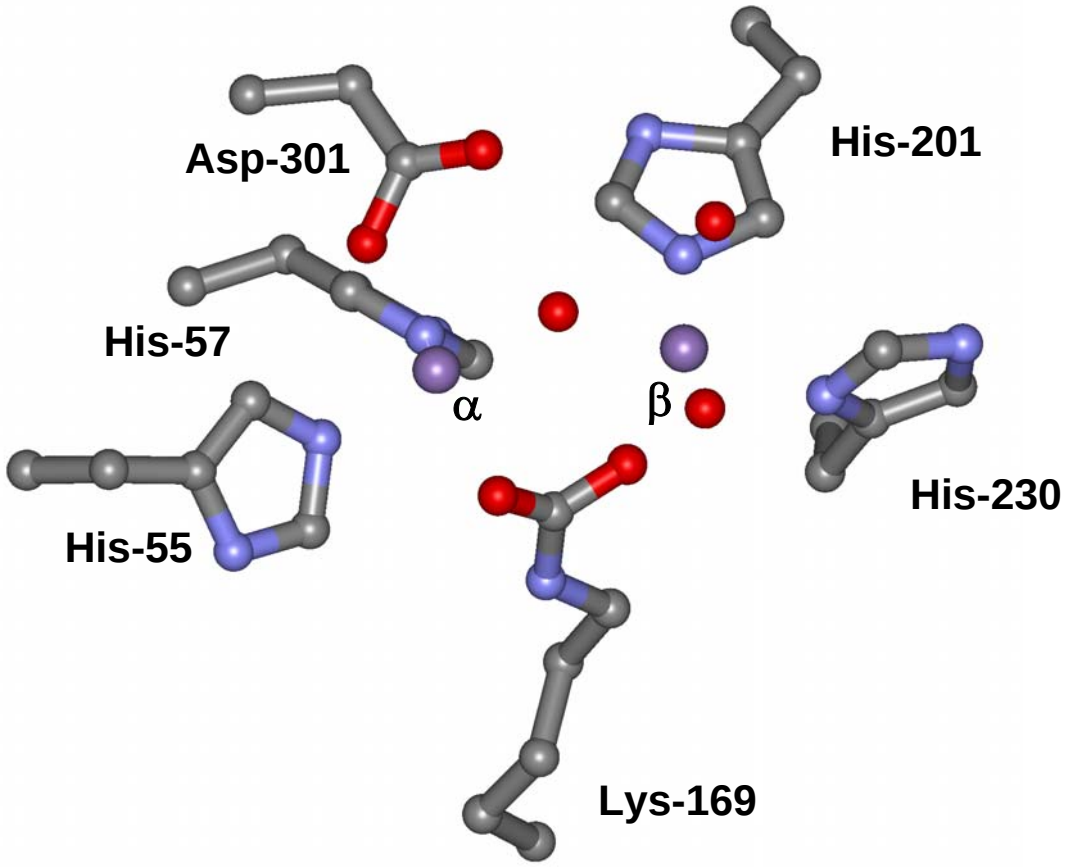

Figure 15. Representation of the binuclear metal center within the active site of Mn/Mn-PTE. The manganese ions are depicted as purple spheres. The coordinates were obtained from the PDB entry, 1i0b.

The enzymatic hydrolysis of the insecticide paraoxon is presented in Scheme 1.

Scheme 1

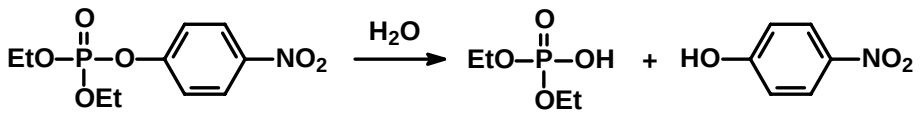

A comprehensive mechanism for the enzymatic hydrolysis of organophosphates by PTE has been proposed (*13*). In this mechanism hydroxide is activated for nucleophilic attack through a hydrogen bonding interaction with Asp-301 and ligation to the binuclear metal center (*47, 48*). The phosphoryl oxygen bond of the substrate is polarized by a direct interaction to the β-metal. The phosphotriester bond is cleaved in an S_N2-like reaction that results in the liberation of the leaving-group and the parent diester products. However, the identity of hydroxide as the solvent bridge has not been confirmed by spectroscopic methods.

The pH-rate profile for PTE shows a decrease in catalytic activity as the pH is lowered. The apparent pK_a value for the loss of catalytic activity varies from 5.8 to 8.1, depending upon the identity of the metal ions substituted within the active site (*10*). Since organophosphate substrates for PTE do not ionize in this pH range, the functional group that is protonated with the loss of catalytic activity must originate from the enzyme. The most likely candidates for this protonation site are Asp-301 and the hydroxide that has been proposed to bridge the two divalent cations. Asp-301 is hydrogen bonded to the bridging ligand and additionally coordinated to the α-metal ion. The mutation of Asp-301 to an alanine or asparagine results in the loss of substantial catalytic activity but does not significantly change the value of the kinetic pK_a (*13*).

Electron paramagnetic resonance (EPR) spectroscopy can be used to obtain unique structural and mechanistic information about metal centers within enzyme active

sites. For example, with Mn(II)-containing enzymes, EPR spectroscopy has been used to investigate inhibitor binding, metal-metal interactions, metal-metal exchange coupling, and the identity of metal-metal bridging ligands (*25, 49-51*). EPR has also been used to study metal-protein interactions and substrate binding orientations for non-manganese enzymes, such as ribonucleotide reductase and enolase, via substitution of the native metal ions with manganese (*24, 52*). Prior EPR investigations of Mn/Mn- and Cu/Cu-substituted PTE established that the structure of the metal center is binuclear in an asymmetric nitrogen and oxygen coordination environment (*53, 54*).

This paper probes the identity of the solvent bridging species by monitoring perturbations in the EPR spectrum of Mn/Mn-PTE resulting from changes in pH. The identity of the protonated species responsible for the loss in the catalytic activity of PTE was addressed via a direct comparison of the effect of pH on the kinetic constants and EPR spectra. From these studies, the solvent bridge between the two divalent cations is postulated as hydroxide and the diminution of catalytic activity at low pH is proposed to be due to the loss of the bridging nucleophile.

MATERIALS AND METHODS

Materials. Diethyl-*p*-nitrophenylphosphate (paraoxon) and all buffers were purchased from Sigma except for N-(2-hydroxyethyl)piperazine-N'-2-ethane-sulfonic acid (HEPES), which was purchased from United States Biochemical. Bacterial cell growth protocols, enzyme purification, preparation of apo-enzyme, and the reconstitution of PTE with manganese were performed as previously described (*10, 53*).

Kinetic Measurements. The values of k_{cat} and k_{cat}/K_m for Mn/Mn-PTE were determined by measuring the change in absorbance at 347 nm upon hydrolysis of paraoxon (20 - 2000 μM) to *p*-nitrophenol ($\varepsilon_{347} = 5.1 \times 10^4\ M^{-1}\ cm^{-1}$) and diethyl phosphate in 100 mM buffer at 30 °C with a $Spectra_{Max}$ PLUS 384 plate reader from

Molecular Devices. The pH was varied from 6.0 to 9.5 in increments of 0.2 and the final pH was measured at the conclusion of the enzymatic reaction. The buffers used for this investigation were: MES, pH 5.5 - 6.4; PIPES, pH 6.5 - 7.0; HEPES, pH 7.1 - 8.0; TAPS, pH 8.1 - 8.9; CHES, pH 9.0; and TABS, pH 9.1 - 9.5.

Data Analysis. The kinetic constants were obtained by fitting the data to equation 10, where v is the initial velocity, E_t is the enzyme concentration, k_{cat} is the turnover number, K_m is the Michaelis constant, and A is the concentration of substrate. The kinetic pK_a value for Mn/Mn-PTE with paraoxon as the substrate was determined by fitting the pH-rate profile to equation 11, where y is k_{cat}/K_m for the hydrolysis of paraoxon, C is the pH-independent value of y, H is the proton concentration, and K is the dissociation constant for the ionizable species (*55*). The apparent pK_a value determined from the changes in the EPR spectra as a function of pH for Mn/Mn-PTE was also obtained by fitting the data to equation 11, where y is the fraction of the total signal intensity associated with the antiferromagnetically coupled binuclear manganese in the sample.

$$v / E_t = (k_{cat} A) / (K_m + A) \quad (10)$$

$$\log y = \log (C / (1 + (H / K))) \quad (11)$$

EPR Sample Preparation. Mn/Mn-substituted PTE samples of ~1.0 mg/mL, pH 8.0, were concentrated to ~12 mg/mL using a YM-10 Centricon microconcentrator from Amicon. Removal of unbound manganese from the protein sample was accomplished by elution through a PD-10 Sephadex G-25 desalting column from Amersham. Changes in pH were achieved by exchange of the protein into 100 mM buffer at the desired pH using a PD-10 column. Samples used to observe the recovery of the binuclear signal at high pH following incubation at low pH were not treated with a PD-10 column in order

to minimize loss of labile Mn(II). These samples were diluted into concentrated buffer to achieve the desired pH. All EPR samples were initially frozen in liquid nitrogen at a concentration of 200 μM PTE containing 30% (v/v) glycerol. The protein concentrations were determined by measuring the absorbance at 280 nm using an extinction coefficient of 29,300 $M^{-1}cm^{-1}$ (*10*). The metal content was determined using furnace atomic absorption spectroscopy with a Perkin-Elmer AAnalyst 700. Mn(II) spin quantitation was determined by double integration of the derivative spectrum and comparison with standards of $MnCl_2$ at known concentration. The spin concentrations determined by double integration of the EPR signals matched the metal concentration in the samples predicted by atomic absorption.

EPR Spectroscopy. X-band EPR measurements were obtained using a Bruker ESP 300 spectrometer with a TE_{102} cavity, an Oxford Instruments liquid helium cryostat, an HP 5352B microwave frequency counter, and a Bruker ER 041XG microwave bridge. The magnetic field modulation amplitude was 20 G at a frequency of 100 kHz. EPR spectra were obtained at 10 K under non-saturating power conditions of 2 mW.

RESULTS

pH-Rate Profile. The kinetic parameters for the catalytic activity of PTE depend on the identity of the metal ions in the active site (*10*). Mn/Mn-substituted PTE is reported to have a k_{cat} of 1800 s^{-1}, a K_m of 80 μM, and a k_{cat}/K_m of 2.2 x 10^7 M^{-1} s^{-1} for the hydrolysis of paraoxon at pH 9.0 (*10*). The pH-rate profile for the hydrolysis of paraoxon by Mn/Mn-PTE is presented in Figure 16A. A pK_a value of 7.1 ± 0.06 was determined from a fit of the data for k_{cat}/K_m as a function of pH to equation 11. The data fit well to a model in which only one species is protonated and a loss in catalytic activity is observed with protonation of this species.

*pH Dependence of EPR Spectra***.** Perturbations in the spectral properties of the binuclear metal center within the active site of PTE were correlated with the catalytic power of the enzyme as a function of pH. EPR spectra of Mn/Mn-substituted enzyme were obtained as a function of pH and are presented in Figure 17. At pH 8.3, only the binuclear Mn(II) signal is observed. At pH 7.0, a mononuclear Mn(II) signal is observed at $g = 2$ in addition to the binuclear signal. As the pH decreases, the signal intensity for the coupled binuclear Mn(II) complex diminishes while the signal intensity for mononuclear Mn(II) increases. At pH 6.0, only the mononuclear Mn(II) signal is observed. The signal intensities of three hyperfine splittings from the binuclear Mn/Mn-PTE signal were averaged to quantitate the binuclear Mn/Mn-PTE signal intensity. In Figure 17, the three lines in the EPR spectrum originating from the binuclear Mn/Mn-PTE complex are designated by the thin arrows. The total manganese spin was determined for each spectrum by double integration of the derivative EPR signal. The fraction of the observed spin coupled binuclear signal for each spectrum was determined from the ratio of these measurements. The apparent pK_a associated with the pH-titration of the coupled binuclear metal complex was determined by fitting the log of the fraction of the binuclear signal intensity verses pH to equation 11 and is shown in Figure 16B. The fit of the data resulted in a pK_a value of 7.3 ± 0.1.

The diminution of the signal for the coupled binuclear metal center with decreasing pH can result from the loss of the bridging ligand that enables the exchange coupling between the two metal ions. Alternatively, one or both of the metal ions within the metal center could dissociate from the active site. However, it is unlikely that the mononuclear EPR spectra observed at low pH originates from Mn(II) that is dissociated from the active site, since a gel filtration procedure was employed that would have separated the macromolecular protein from any loosely bound Mn(II) in solution. It was

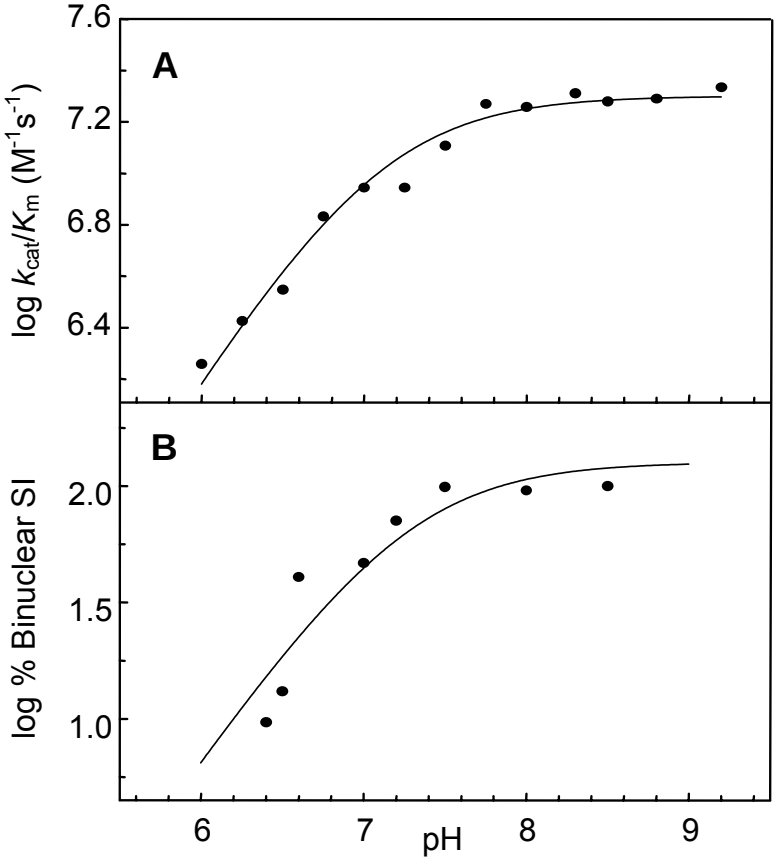

Figure 16. The pH-profiles for the hydrolysis of paraoxon and the interconversion between the binuclear and mononuclear EPR spectra. (A) The pH-rate profile for the hydrolysis of paraoxon by Mn/Mn-PTE. The experimental data were fit to equation 11 with an apparent kinetic pK_a of 7.1 ± 0.06. (B) The pH profile for the titration of the binuclear metal center within the active site of PTE. The experimental data were fit to equation 11 with an apparent pK_a of 7.3 ± 0.1. Additional details are provided in the text.

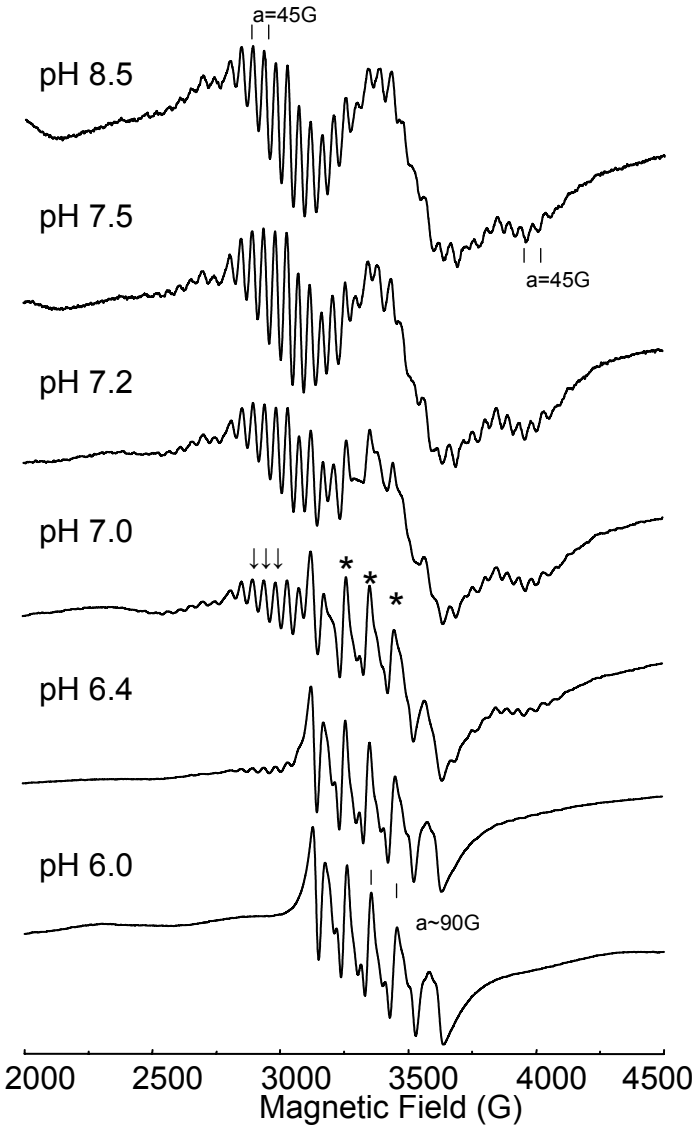

Figure 17. X-band EPR spectra of Mn/Mn-PTE at various pH values. Spectra were obtained at 2 mW power, 20 G modulation amplitude, and 10 K. Arrows designate binuclear signal and asterisks designate mononuclear signal. Additional details are provided in the text.

previously determined that metal binding to the active site of PTE is a cooperative process resulting in two metal ions per active site (*46*). The pH at which catalytic activity is lost depends on the metal identity and not the loss of metal at the active site (*10*). Therefore, both metals are expected to be present at neutral to low pH. To support this, the reversibility of the effects of pH was confirmed by monitoring the same Mn/Mn-PTE sample at pH 8.2, after lowering the pH to 6.8, and again after raising the solution pH to 8.2. Figure 18 illustrates the EPR spectrum of the enzyme before and after the change in pH. After increasing the pH to 8.2, almost complete recovery of the binuclear signal was achieved. The samples subjected to incubation at lower and then higher pH do show some remaining mononuclear Mn(II). This may be due to same adventitious Mn(II) from damaged samples; unlike the case for the EPR samples used for the spectra shown in Figure 17, the samples used to demonstrate reversibility, Figure 18, were not eluted through a desalting column. It is also possible that samples brought back to high pH were not fully equilibrated before freezing, leaving some samples that lack the bridging ligand. Despite the small fraction of unrecovered binuclear signal, the restoration of the majority of this signal indicates that formation of the binuclear Mn(II) species is dependent upon and reversible with pH. The ability to recover the binuclear signal requires both metals to be positioned in the active site and available for exchange coupling. Therefore, the effect of pH on the binuclear signal is due to the influence of pH on the protonation state of the bridging ligand which facilitates the exchange coupling between the two metals.

In order to check for weak population of the mononuclear Mn(II) signal in samples subjected to high and low pH conditions, the strong temperature dependence of the overlapping binuclear signal was utilized to diminish its population in the $g = 2$ region. The binuclear signal is temperature dependent with the greatest signal intensity

at 10 K. Spectra were collected at temperatures of 3.6 K to 200 K (Figure 19). For samples below pH 7.3, the six-line pattern of the mononuclear signal was more pronounced at higher temperatures while the binuclear signal diminished in intensity (Figure 20). The binuclear signal in samples above pH 7.3 diminished with increasing temperature, but no mononuclear signal was observed.

DISCUSSION

Identification of Hydroxide Bridge. The identity of the bridging species within the binuclear metal center of PTE is of significant interest due to its pivotal role as the species responsible for the nucleophilic attack on the substrate. Metalloproteins containing binuclear metal sites coupled by bridging oxo, hydroxide, and water ligands are not uncommon. PTE, urease, enolase, purple acid phosphatase, methane monooxygenase, and ribonucleotide reductase are well-characterized examples of these metalloproteins (*5, 36, 56-61*). When the metal center is paramagnetic, the magnetic properties can provide structural information on the identity of the bridging ligand. Magnetic coupling of metal centers is often facilitated by their bridging ligands through a superexchange mechanism. The sign and magnitude of the exchange coupling constant, *J*, are influenced by the bridge identity, metal identity, terminal ligand identity, metal-bridge-metal angle, metal-metal distance, metal-bridge distance, and in-plane bridge-metal alignment (*62-67*).

Structural and spectroscopic properties of model complexes with bridging oxygen ligands can aid in understanding the identity of the bridging ligand in PTE. The strength of the exchange interaction generally varies with the protonation state of the bridging oxygen as $O^{-2} > OH^{-} > OH_2$ (*68-71*). The exchange coupling constant for the *S* = 2 spin manifold of Mn/Mn-PTE was reported as $J = -2.7 \pm .02$ cm^{-1} ($H_{ex} = -2JS_1 \cdot S_2$) (*23*). Exchange coupling constants observed for dimanganese(II) complexes with a

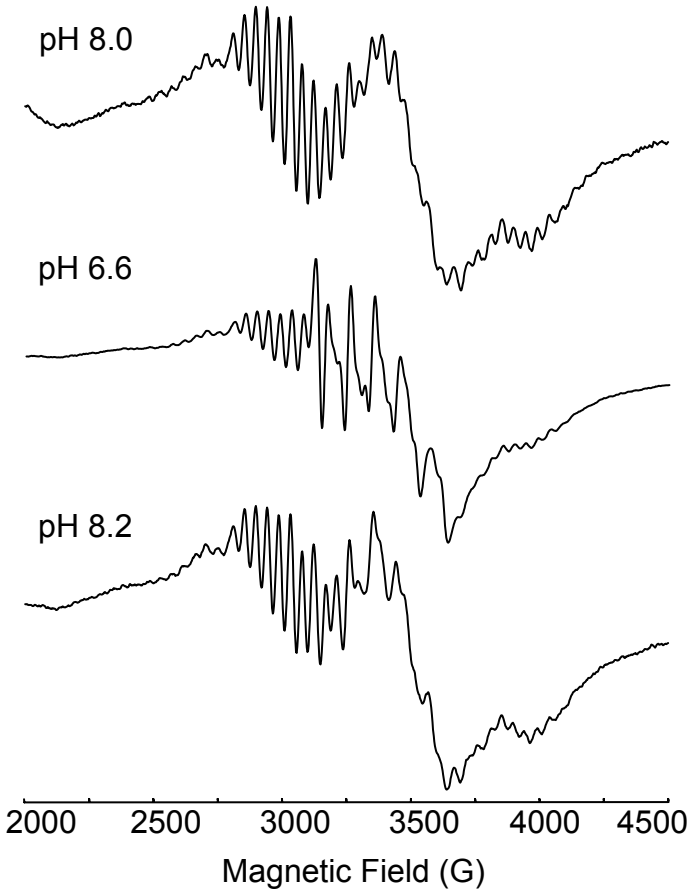

Figure 18. X-band spectra of a sample of Mn/Mn-PTE at pH 8.0, lowered to pH 6.8, and raised to pH 8.2. EPR conditions are 2 mW power, 20 G modulation amplitude, and 10 K.

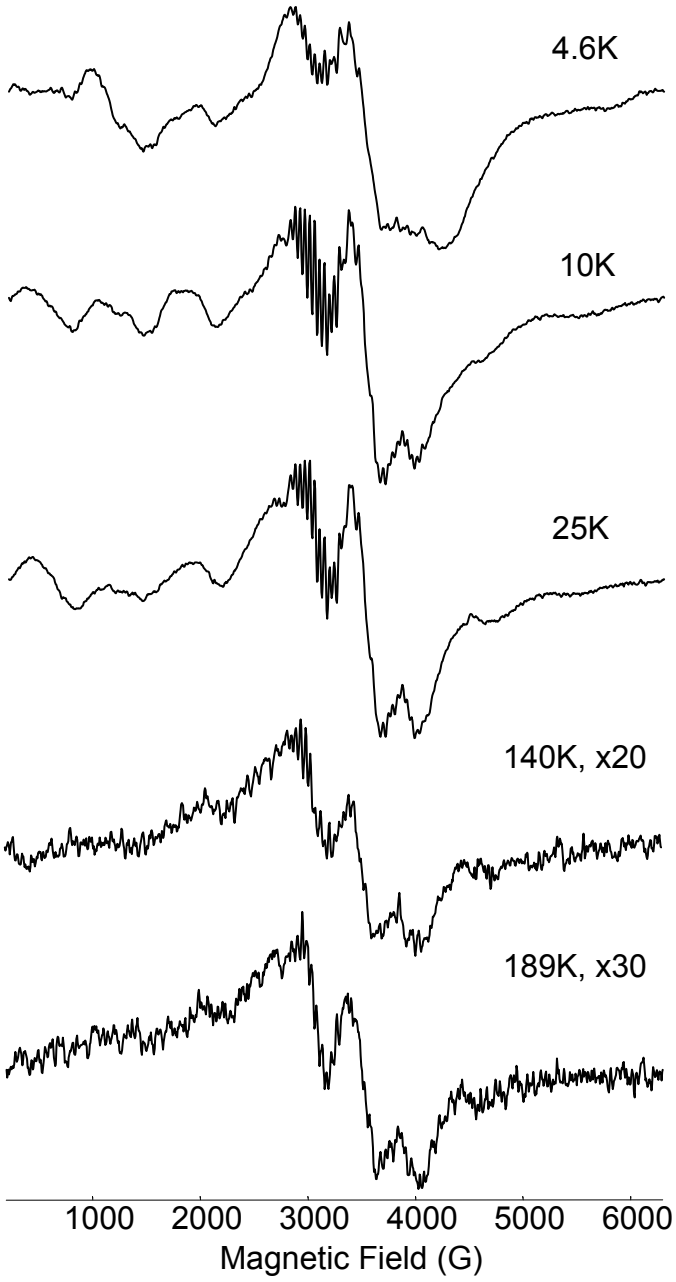

Figure 19. EPR spectra of Mn/Mn-PTE at pH 8.0 collected at various temperatures. EPR conditions are 2 mW power and 20 G modulation amplitude.

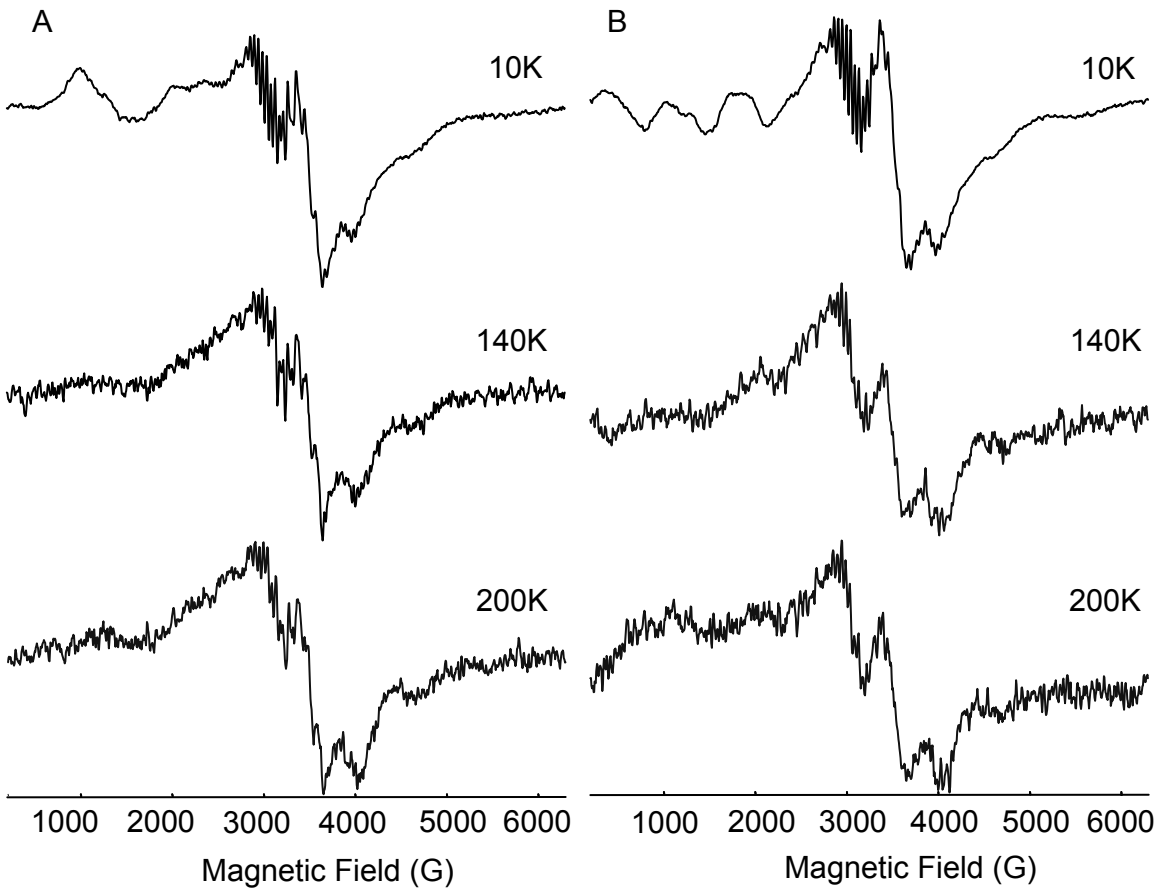

Figure 20. EPR spectra of Mn/Mn-PTE at 10 K, 140 K, and 200 K. A) Spectra of Mn/Mn-PTE at pH 7.2. B) Spectra of Mn/Mn-PTE at pH 8.0. Mononuclear Mn(II) species is observed in spectra collected for the sample at pH 7.2. No mononuclear Mn(II) species is observed in spectra collected for the sample at pH 8.0. EPR conditions are 2 mW power and 20 G modulation amplitude.

hydroxide bridge range from -2.5 cm^{-1} for a complex with no other bridging species to -9 cm^{-1} for complexes with two additional carboxylate bridges (*31, 69*). The *J*-value of -2.7 ± .02 cm^{-1} is reasonable for a dimanganese(II) complex with a hydroxide bridge and one carboxylate bridge. The metal-bridge distances determined for the X-ray crystal structure for Mn/Mn-PTE are 2.0 and 2.1 Å the α- and β-metal ions, respectively. The reported average distance of 2.0 Å for Mn(II)-μOH^- and 2.5 Å for a Mn(II)-μOH_2 model complexes are supportive of a hydroxide bridge for the binuclear metal center in the active site of PTE (*25, 31, 69*).

In order to further investigate the identity of the bridging solvent in PTE, EPR was used to evaluate changes within the metal center due to changes in pH. From kinetic measurements it is concluded that the loss in catalytic activity occurs upon protonation of a single species. The pK_a associated with this site is influenced by the identity of the metal ions bound to the active site of PTE (*10*). Four potential models for protonation sites and their consequences are presented in Figure 21. If protonation of the binuclear metal center occurs without the loss of the bridging species, as shown in Figures 21A and 21B, the exchange coupling constant, *J*, would be expected to decrease and increase in magnitude, respectively. In Figure 21A, protonation of the hydroxide bridge would result in a shift of electron density from the bridging oxygen-metal bonds to the new oxygen-hydrogen bond, resulting in a decrease in exchange coupling. In Figure 21B, protonation of Asp-301 would disrupt the hydrogen bonding interaction between the oxygen of Asp-301 and the hydrogen of the hydroxide bridge. This interaction would increase the electron density on the oxygen of the hydroxide bridge and result in an increase in exchange coupling. Changes in *J* would be revealed as changes in the temperature dependence of the binuclear Mn(II) EPR signal. No binuclear signal was observed, over a range of temperatures, for samples poised below

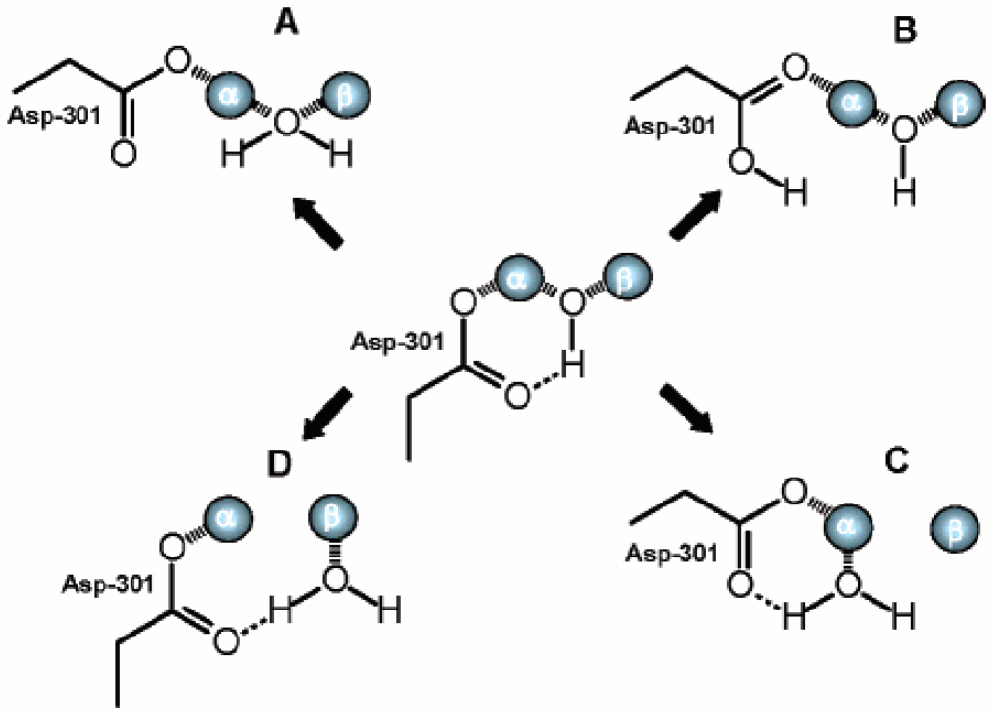

Figure 21. Models for the pH-dependence of PTE catalytic activity. The active form of PTE is placed in the center and protonation of the bridging hydroxide or Asp-301 are considered. (A) bridging water; (B) protonated Asp-301; (C) water ligation on the α-metal; (D) water ligation on the β-metal.

pH 6.4. Instead, only a mononuclear Mn(II) signal was observed at these pH values that differs from free Mn(II) in solution (Figure 22). Due to the absence of the binuclear signal, the models presented in Figures 21A and 21B are ruled out. The absence of a binuclear signal at low pH indicates the loss of the bridging species due to the protonation of the proposed hydroxide bridge. Water ligation could occur to either the α- or β-metal, as presented in Figures 21C and 21D, respectively. The ability to regain the binuclear signal after raising the pH supports the reversible protonation of the hydroxide bridge.

The EPR signals from Mn/Mn-PTE at low pH values resemble those from mononuclear Mn(II), and yet the ability to recover the binuclear signal upon raising the pH suggests that the Mn(II) ions remain in the PTE active site and in close proximity. The loss of binuclear signal at pH values of 7.25 and lower is not attributed to protonation at the carboxylated lysine since the pK_a of a carboxyl-oxygen ligating a metal would be less than 4. Exchange coupling through this bridge is expected to be minimal, however, due to the high negative electron density on the metal ligating oxygens (*12*). There are few EPR studies of singly bridged dimanganese(II) compounds. The active site of xylose isomerase contains two divalent metal ions that are bridged by a single carboxyl group. In the investigation of xylose isomerase from *Streptomyces rubiginosus* by Witzel and co-workers, the EPR spectra for the $Mn(II)_2$-substituted xylose isomerase showed no exchange coupling (*72*). In an effort to model dinuclear metal sites containing a single carboxyl bridge, Sakiyama and co-workers synthesized a dimanganese(II) center with each metal ligated by five nitrogens and the oxygen of the bridging acetate (*73*). Weak antiferromagnetic coupling was observed via magnetic susceptibility with a coupling constant of -0.37 cm^{-1}. The EPR spectrum of the compound at 4 K showed a broad line centered at g = 1.96 and smaller features at lower

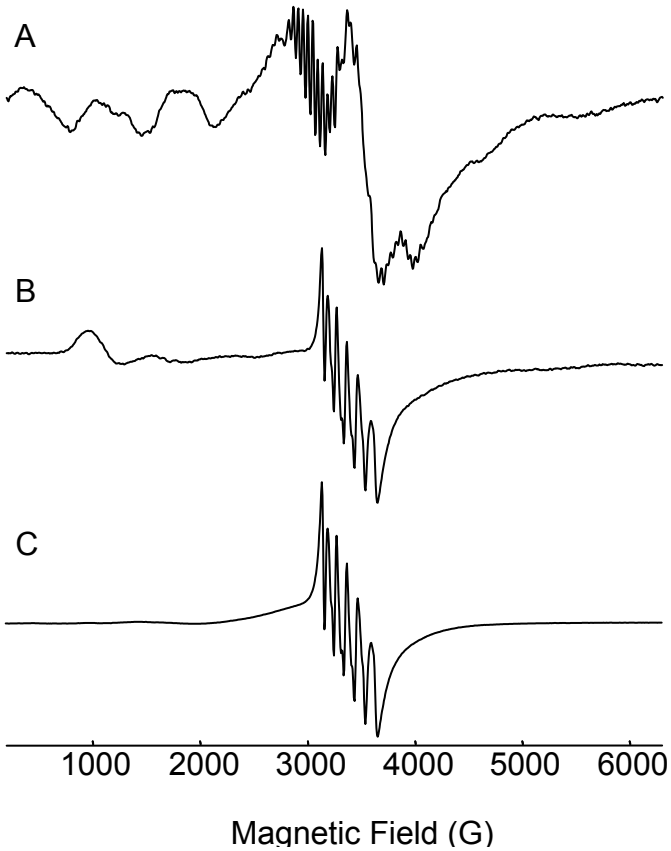

Figure 22. EPR spectra of bound Mn(II) within the active site of PTE and free Mn(II) in solution. (A) Mn/Mn-PTE at pH 8.0 (B) Mn/Mn-PTE at pH 6.4 (C) $MnCl_2$ in water. EPR conditions are 2 mW power and 20 G modulation amplitude.

and high fields. As an example of another weakly coupled system, weak ferromagnetic exchange coupling of 0.33 cm^{-1} was determined for the dichloro-bridged manganese(II) complex, $[Mn(\mu\text{-}Cl)(2,2'\text{-bi-imidazoline})_2]_2Cl_2$ (*74*). In solution this compound exhibited an EPR signal similar to that observed for mononuclear Mn(II) although the integrity of the cluster could not be verified. It is possible that, upon protonation of the Mn/Mn-PTE hydroxide bridge at low pH, the Mn(II) ions are retained with very weak or no coupling, giving rise to the signals observed here, and are easily recoupled upon increasing pH.

Molecular simulation studies of the Zn/Zn- and Cd/Cd-substituted forms of the active site within PTE by Krauss *et al.* and Ornstein *et al.* have also determined that hydroxide is the most likely species to bridge the binuclear metal center (*75, 76*). Krauss *et al.* found that protonation of the bridging hydroxide resulted in water ligation to the β-metal position, which is illustrated in Figure 21D (*75*). Kinetic studies have demonstrated that the α-metal has the greatest influence on the pK_a for substrate turnover as a function of pH. A Zn/Cd-PTE hybrid was prepared with Zn and Cd ions in the α- and β-metal sites, respectively (*5, 13, 77*). The kinetic pK_a of the Zn/Cd PTE hybrid most closely resembled the pK_a of the Zn/Zn-substituted enzyme relative to the Cd/Cd-substituted enzyme (*13*). The water ligand after protonation of the bridging hydroxide is therefore expected to reside primarily on the α-metal. The present work supports the protonation of the bridging hydroxide to a bound water molecule as indicated in Figures 21C and 21D. The localization of the water molecule on the α-metal is preferred based upon the kinetic properties of the Zn/Cd-hybrid (*13*).

Molecular simulations by Ornstein and coworkers on the thermodynamics of protonation by the bridging hydroxide for Zn- and Cd-substituted PTE produced pK_a values of 5.1 and 8.4, respectively (*76*). These simulations are comparable to the

previously reported experimental kinetic pK_a values of 5.8 for Zn/Zn-PTE and 8.1 for Cd/Cd-PTE (*10*). Thus, the calculations by Ornstein and coworkers also support the proposal that the site of protonation within the binuclear metal center of PTE is the bridging hydroxide. The protonation of this group results in the loss of catalytic activity.

In this investigation pK_a values of ~7.2 ± 0.1 were determined for the protonation of the bridging hydroxide with the Mn/Mn-substituted PTE from both kinetic data and EPR spectra as a function of pH. The pK_a values of water bound to simple Mn-complexes have values between 10 and 11 (*12*). The pK_a of water is lowered upon metal coordination due to charge delocalization onto the metal center. Water coordination to two manganese ions further decreases the pK_a of water (*12, 78, 79*). The pK_a values of 7.1 and 7.3 obtained from the kinetic and EPR data are therefore reasonable values for water coordinated to both metals within the active site of Mn/Mn-PTE.

In the investigation of rat liver arginase by Dismukes and coworkers, an exchange-coupled dimanganese metal center was observed by EPR. The exchange coupling constant for the complex of arginase with borate is -2.0 ± 0.5 cm^{-1} (*25*). The two metals have unique ligand coordination environments resulting in an asymmetric environment like that observed in PTE. However, the identities of the metal ligands are different, including an additional carboxylate bridge in the active site of arginase. No changes in the EPR signal of Mn/Mn-arginase were observed at pH values as low as 6.3 by Dismukes, Ash and coworkers (*25*). The bridging molecule from solvent bound to the binuclear metal center for arginase was therefore concluded to be a water ligand. A kinetic pK_a of 7.5 reflecting loss in arginase catalytic activity at low pH was assigned to His-141 (*25*). The pK_a of a solvent molecule bridging two divalent metals is influenced by the electron withdrawing capability of those metals. The addition of a negatively charged carboxylate bridge to the metal center would lessen this electron withdrawing

capability. Therefore, it is possible that the additional carboxylate bridge in arginase results in a predominantly aqua species instead of the hydroxyl species found in PTE. The metal-bridging oxygen distance of ~2.4 Å observed in the X-ray crystal structure of arginase also supports a bridging water ligand. These findings greatly differ from the pH-dependent EPR spectrum of PTE that exhibits reversibility and the metal-bridging oxygen distances in PTE that correlate with a bridging hydroxide ligand.

The Mn/Mn-PTE EPR spectrum exhibits exchange coupling that is facilitated through a hydroxide bridge. Protonation of the bridging hydroxide results in the loss of the exchange coupling between the two divalent cations and the loss of catalytic activity. The reversible protonation of the bridging hydroxide has an apparent pK_a of 7.3 based upon changes in the EPR spectrum of Mn/Mn-PTE with alterations in pH. The pH-rate profile for the hydrolysis of paraoxon by Mn/Mn-PTE shows the requirement of a single function group that must be unprotonated with a pK_a of 7.1. The comparable pK_a values are proposed to result from the protonation of the same ionizable species.

CHAPTER IV

INVESTIGATION OF INHIBITOR-METAL INTERACTION AT THE ACTIVE SITE OF PHOSPHOTRIESTERASE

Phosphotriesterase from *Pseudomonas diminuta* is a zinc metalloenzyme found in soil bacteria capable of organophosphate hydrolysis at rates approaching the diffusion controlled limit (*43*). Interest in PTE for degradation of chemical warfare agents and disposal of pesticides supports the need to understand the mechanism by which it performs hydrolysis. The hydrolysis of the insecticide paraoxon is shown in Scheme 1. While the natural substrate has not been identified, a variety of organophosphates are hydrolyzed by the enzyme. Inhibition has been observed with phosphotriesters with poor leaving groups, phosphonates, and reaction products (*80*). Crystallization of enzyme with inhibitor has provided insight into the stereochemical selectivity of the enzyme as well as implication of substrate binding at the metal center (*81*).

Scheme 1

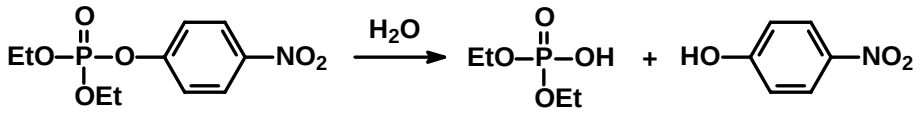

Each subunit of the 72 kDa PTE homodimer contains a binuclear metal active site that resides within a $(\beta/\alpha)_8$ - TIM barrel motif (*82*). Two unique metal sites are observed with the α-metal coordinated by two histidines and an aspartate and the β-metal coordinated by two histidines and one or two water ligands depending on the metal identity (*5*). The metals are bridged by a carboxylated lysine and a hydroxyl bridge. Both metals are required for full catalytic activity and bind to the enzyme in

pairs (*10, 46*). Substitution of the Zn ions at the active site with Mn, Co, Ni, or Cd results in the retention of catalytic activity (*10*).

Previous work has established key components in the catalytic mechanism. Binding of substrate is proposed to occur at the β-metal site based on crystal structures of PTE with inhibitor (*47, 81*). Polarization of the phosphoryl-oxygen bond of substrate by the metal center was determined by comparison of phosphate and thiophosphate triester substrates (*13*). Hydrolysis of the substrate occurs via a S_N2 type mechanism observed as the net inversion of stereochemistry at the phosphorus center (*48*). The nucleophile involved in the cleavage of the phosphoester bond was identified as the hydroxide bridging the two metals through the correlation of results from EPR and kinetic studies (*10, 23*). These findings bring to light three major components of the PTE mechanism that utilize the metal center. 1) The metal center increases the electrophilicity of the phosphorus center by polarization of the phosphoryl oxygen bond. 2) The metal center provides the nucleophile for hydrolysis by lowering the pK_a of coordinated water. 3) The metal center in conjunction with the active site binding pockets serves to position the substrate creating optimal interactions between the nucleophile and electrophile.

The influence of substrate binding on the metal center and its consequential effect on the hydroxyl bridge has not been thoroughly investigated. Weakening of the hydroxyl bridge bond to the β-metal of dihydroorotase upon substrate binding is proposed based on the crystal structure of the enzyme with substrate and product bound at different subunits (*30*). A weakening of the hydroxide-metal bond in PTE would result in a more potent nucleophile in close proximity to the phosphorus center of the substrate. Under crystallographic conditions, the hydroxyl bridge is present in Zn/Zn-PTE with inhibitor at the metal center (*47, 81*).

Here, the effects of inhibitor and product binding on the magnetic properties of the metal center and the hydroxyl bridge are investigated by electron paramagnetic resonance spectroscopy (EPR). Spectra of Mn/Mn-PTE are evaluated to determine complex formation at the metal center upon addition of the following: diisopropyl methyl phosphonate (DIMP), triethyl phosphate (TEP), and diethyl phosphate (DEP), Scheme 3.

Scheme 3

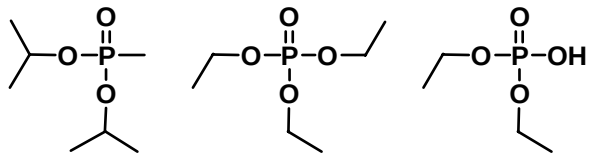

MATERIALS AND METHODS

Materials. Diisopropyl methyl phosphonate (DIMP), triethyl phosphate (TEP), and all buffers were purchased from Sigma except for N-(2-hydroxyethyl)piperazine-N'-2-ethane-sulfonic acid (HEPES), which was purchased from United States Biochemical. Diethyl phosphate (DEP) was synthesized in the laboratory by Dr. Yingchun Li. Bacterial cell growth protocols, enzyme purification, preparation of apo-enzyme, and the reconstitution of PTE with manganese were performed as previously described (*10*).

Kinetic Measurements. The values of k_{cat} and k_{cat}/K_m for Mn/Mn-PTE were determined by measuring the change in absorbance at 347 nm upon hydrolysis of paraoxon (20 - 2000 μM) to *p*-nitrophenol ($\varepsilon_{347} = 5.1 \times 10^4\ M^{-1}\ cm^{-1}$) and diethyl phosphate in 100 mM buffer at 30 °C with a $Spectra_{Max}$ PLUS 384 plate reader from Molecular Devices. The inhibition constants for DIMP and DEP were determined by measuring the change in absorbance at 400 nm upon hydrolysis of paraoxon in the

presence of each compound (0.1 – 14 mM). The buffers used for this investigation were HEPES, pH 8.0 and CHES, pH 9.0.

Data Analysis. The kinetic constants were obtained by fitting the data to equation 12, where v is the initial velocity, V_{max} is the maximum velocity, K_m is the Michaelis constant, and A is the concentration of substrate. The K_i values for DIMP and DEP with Mn/Mn-PTE in the presence of paraoxon as the substrate were determined by fitting data to equation 13, where I is the concentration of inhibitor and K_i is the inhibition constant for a competitive inhibitor.

$$v = (V_{max} A)/ (K_m + A) \quad (12)$$

$$v = V_{max} A / (K_m (1 + I / K_i) + A) \quad (13)$$

PTE EPR Sample Preparation. Mn/Mn-substituted PTE samples of ~1.0 mg/mL, pH 8.0, were concentrated to ~20 mg/mL using a YM-10 Centricon microconcentrator from Amicon. All protein was loaded onto a PD-10 Sephadex G-25 desalting column from Amersham in order to remove unbound metal from the protein sample. All EPR samples were frozen in liquid nitrogen at concentrations of 100 to 200 μM PTE (3.6 mg/ml to 7.3 mg/ml) containing ~30% (v/v) glycerol in 50 mM HEPES at pH 8.0. EPR samples containing DIMP, TEP, or DEP were frozen after the samples set on ice for 30 minutes. The protein concentrations were determined by measuring the absorbance at 280 nm using an extinction coefficient of 29,300 $M^{-1}cm^{-1}$.

EPR Spectroscopy. X-band EPR measurements were obtained using a Bruker ESP 300 spectrometer with a TE_{102} cavity, an Oxford Instruments liquid helium cryostat, an HP 5352B microwave frequency counter, and a Bruker ER 041XG microwave bridge. The frequency modulation was 100 kHz and the modulation amplitude was 15 G for the samples containing DIMP and TEP and 20 G for all other samples. EPR spectra

were obtained at 10 K, unless designated otherwise, under non-saturating power conditions of 2 mW. Temperature dependent studies were performed from 3.6 K to 60 K for all samples.

RESULTS

Kinetic Constants. The K_m and k_{cat} associated with the hydrolysis of paraoxon by Mn/Mn PTE is 306 ± 25 μM and 3,440 s^{-1}. The k_{cat}/K_m obtained for paraoxon is $1.12x10^7$ $M^{-1}s^{-1}$. The substrate saturation curve shown in Figure 23 was fit to equation 12 to obtain the kinetic parameters. The inhibition of PTE by DIMP and DEP was determined by monitoring hydrolysis of paraoxon at varied concentrations of each. K_i values were obtained from fitting equation 13 to the data in Figure 24. The K_i values determined for DIMP and DEP are 17.1 ± 0.6 mM and 30.2 ± 2.3 mM, respectively.

EPR Spectrum of Mn/Mn-PTE. The EPR spectrum of Mn/Mn-PTE is complex and consists of multiple sets of 11-line splittings separated by 45 G (Figure 25A). Splittings of 45 G are indicative of spin-coupled Mn(II) systems. These binuclear systems are distinctly different from uncoupled, mononuclear Mn(II) EPR spectra, which consist of a six-line pattern separated by 90 G and typically centered at g = 2. Figure 26A is an expansion of the low-field region of Figure 25A. Three broad absorbances are observed with g-values of 14.6, 5.8, and 3.7. The binuclear signal arises from exchange coupling of the two metals through the hydroxide bridge (*23*). Spectra reflecting the temperature dependence of the enzyme signal are shown in Figure 27. The arrows designate the three peaks from the binuclear signal whose signal intensity was monitored over the temperature range of 3.6 – 55 K. The average signal intensity of these three peaks was multiplied by temperature, to remove the signal Curie dependence, and plotted verses temperature in Figure 28. The binuclear signal has previously been

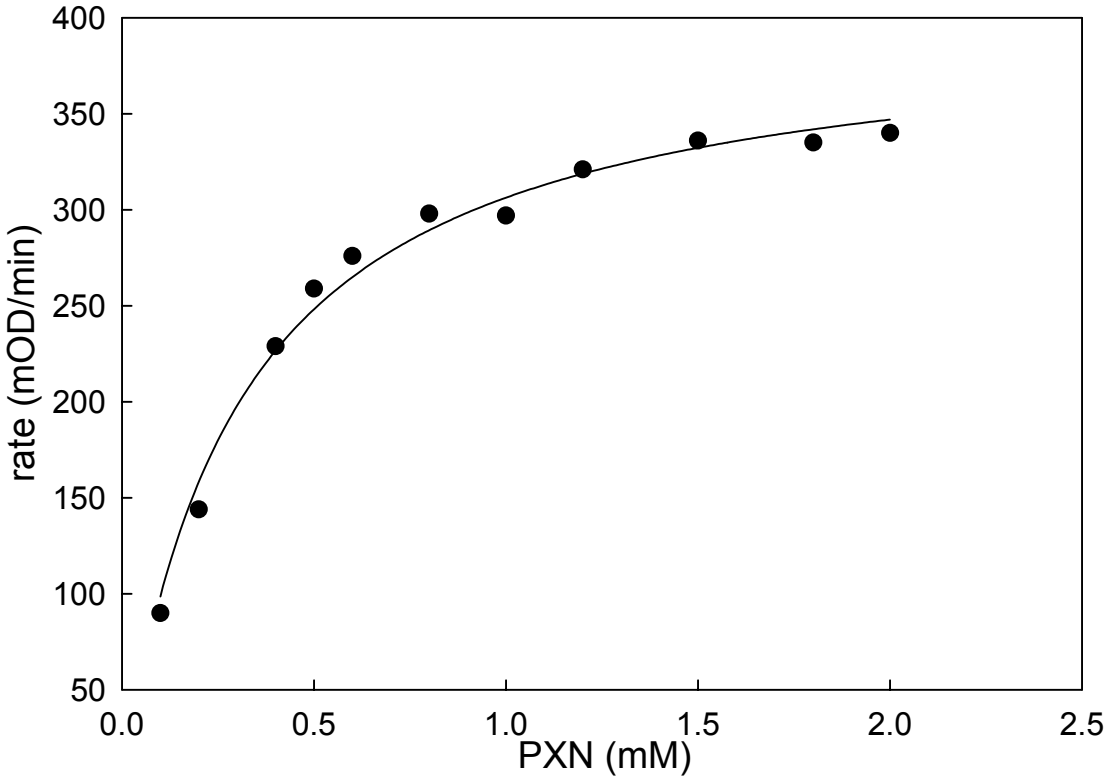

Figure 23. Mn/Mn-PTE saturation curve with paraoxon as the substrate. The kinetic parameters determined were K_m value of 306 ± 25 μM, k_{cat} value of 3,440 s^{-1}, and k_{cat}/K_m value of 1.12x10^7 $M^{-1}s^{-1}$. Assay conditions: 100 mM CHES, pH 9.0, 800 μM $MnCl_2$.

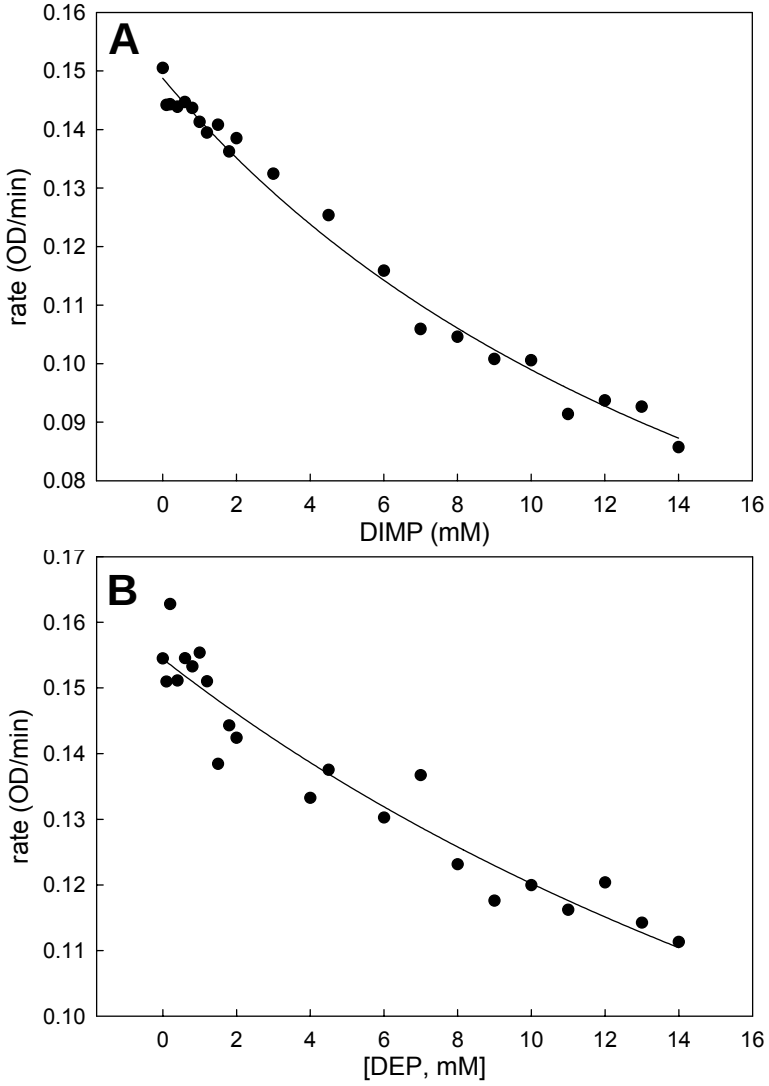

Figure 24. Determination of K_i ,values for DIMP and DEP with Mn/Mn-PTE. (A) DIMP K_i =17.1 ±0.6 mM (B) DEP K_i = 30.2 ±2.3 mM. Assay conditions: 200 μM MnPTE, 100 mM CHES buffer, pH 9.0, 800 μM $MnCl_2$, 50 μM paraoxon.

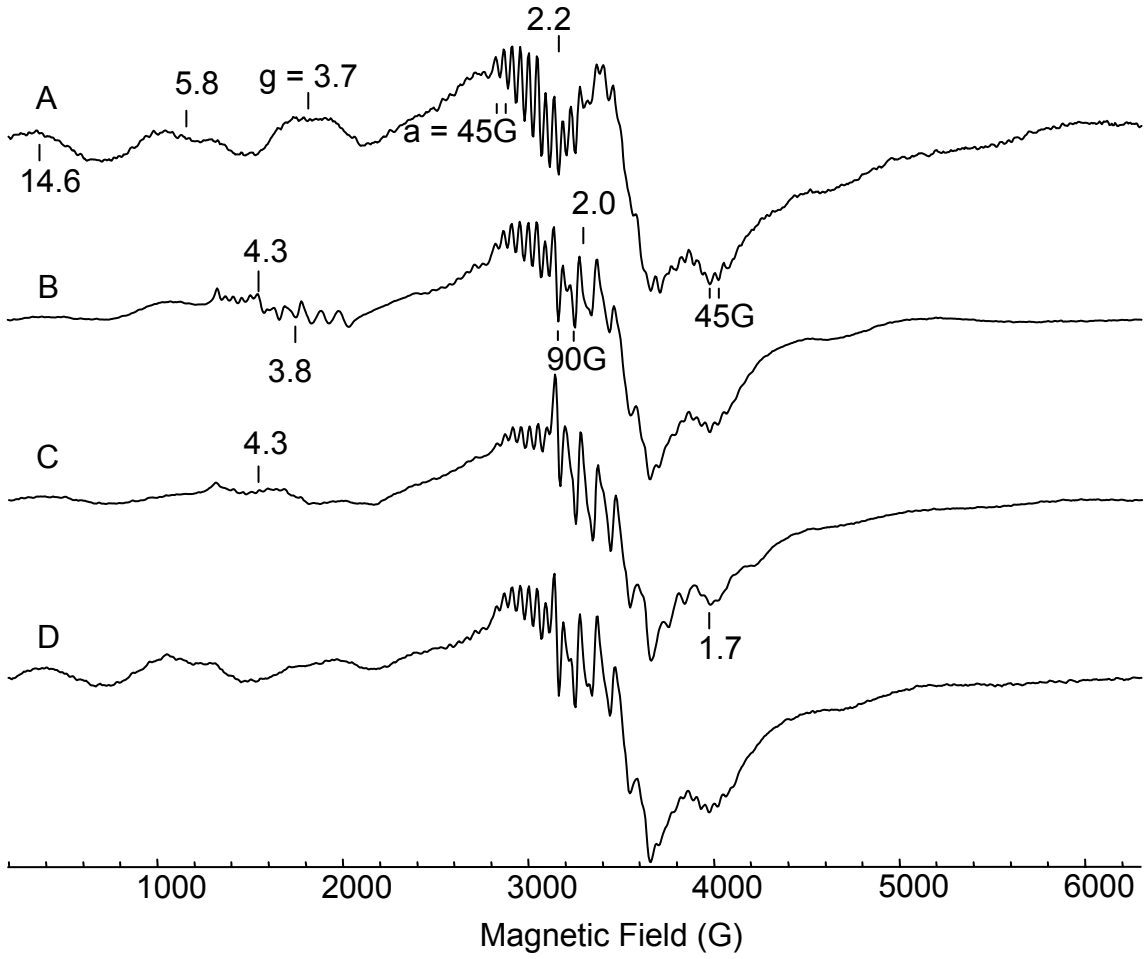

Figure 25. EPR spectrum of Mn/Mn-PTE upon addition of inhibitors and product. (A) 200 μM Mn/Mn-PTE, 3 scans (B) 200 μM Mn/Mn-PTE, 171 mM DIMP, 10 scans (C) 130 μM Mn/Mn-PTE, 350 mM TEP, 20 scans (D) 115 μM Mn/Mn-PTE, 350 mM DEP, 20 scans. All samples in 50 mM HEPES buffer, pH 8.0. EPR conditions: temperature 10 K, microwave power 2 mW, modulation amplitude 20 G.

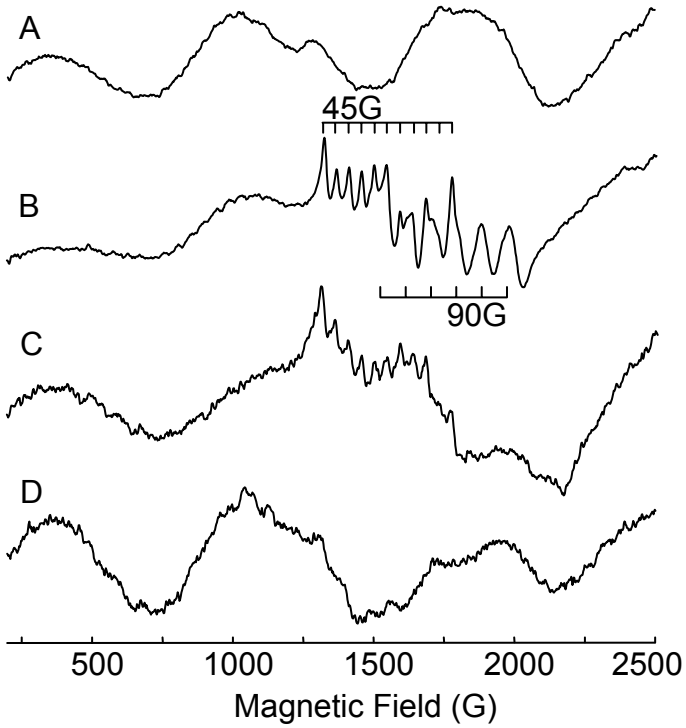

Figure 26. Expanded region of the EPR spectrum of Mn/Mn-PTE upon addition of inhibitors and product. (A) 200 μM MnPTE, 30 scans, modulation amplitude 20 G (B) 200 μM Mn/Mn-PTE, 171 mM DIMP, 20 scans, modulation amplitude 15 G (C) 130 μM Mn/Mn-PTE, 350 mM TEP, 30 scans, modulation amplitude 15 G (D) 115 μM Mn/Mn-PTE, 350 mM DEP, 20 scans, modulation amplitude 20 G. All samples in 50 mM HEPES buffer, pH 8.0. EPR conditions: temperature 10 K, microwave power 2 mW.

assigned to originate from the S = 2 spin manifold via simulation of the experimental spectrum (*23*). The thermal population and depopulation of this spin state can be monitored by the gain and loss of the binuclear signal at g = 2.2. Only a few peaks of the binuclear signal are observed at 3.6 K (Figure 27) indicating that most of the spin associated with this feature resides in a lower spin state. Upon raising the temperature, the multiple 11-line splittings of the Mn/Mn-PTE spectrum are observed with the greatest signal intensity approaching 20 K. The reduction of this signal above 20 K is observed and results from the depopulation of the spin state from which it arises. The strength of the exchange coupling between two metals is reflected in the ease of thermal population of spin states and monitored by the temperature dependence of the signal intensity arising from a given spin state. The temperature dependence of multiple signals within a spectrum can also be utilized in identifying signals that arise from different spin states. The signal intensities of the broad signals at g = 14.6, 5.8, and 3.7 and the multiple 11-line splittings exhibit different temperature dependencies which demonstrates a spectrum composed of signals from multiple spin states. The signal temperature dependence can aid in spin state assignment when spectral simulations are performed. The spectral simulation of Mn/Mn-PTE resulted in the assignment of the binuclear signal at g = 2.2 to the S = 2 spin state. Signals readily observed at 3.6 K are attributed to the S = 1 spin state.

*EPR Spectrum of Mn/Mn-PTE*DIMP*. Diisopropyl methyl phosphonate (DIMP), a sarin analogue, was added to Mn/Mn-PTE at a concentration ten-fold greater than the kinetically determined K_i value. The addition of DIMP to the enzyme resulted in two major changes in the EPR spectrum. The first change is the loss of the binuclear signal at 2.2 and a resulting gain in mononuclear signal at g = 2.0 (Figure 25B). The second change is the appearance of two new signals at g = 4.3 and g = 3.8 (Figure 25B

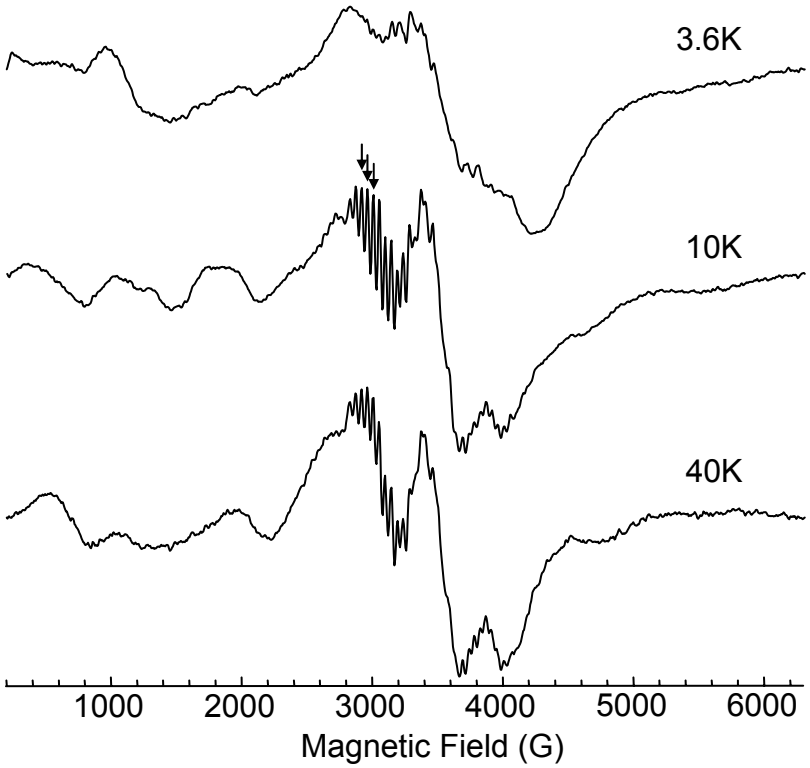

Figure 27. EPR spectrum of Mn/Mn-PTE at various temperatures. 200 μM Mn/Mn-PTE in 50 mM HEPES buffer, pH 8.0. Arrows designate peaks used to monitor signal intensity at each temperature. EPR conditions: 3 scans, microwave power 2 mW, modulation amplitude 20 G.

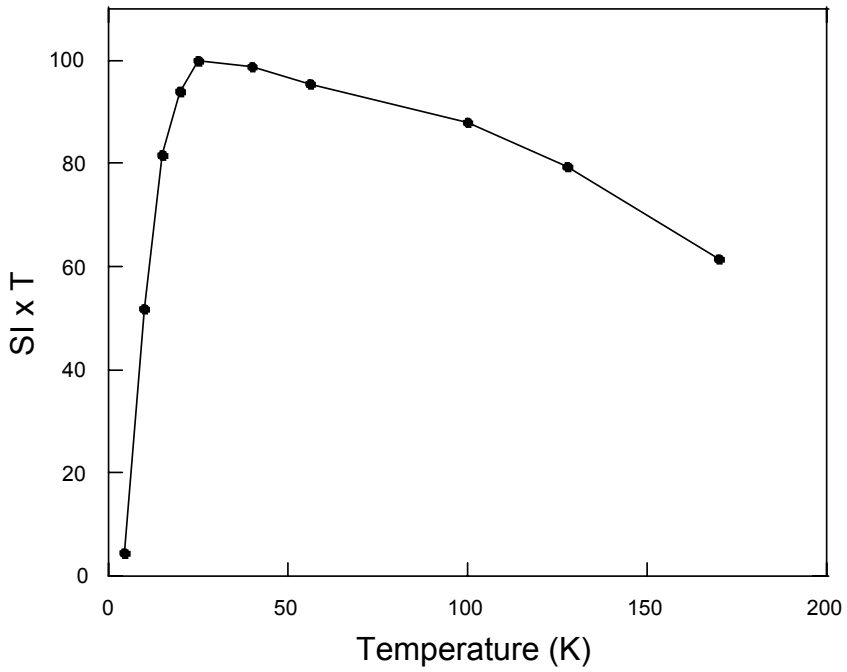

Figure 28. Temperature dependence of the binuclear signal at g = 2.2 of Mn/Mn-PTE. EPR conditions: microwave power 2 mW, modulation amplitude 20 G.

and 26B). The signal centered at g = 4.3 consists of 11 lines separated by 45 G indicative of the spin-coupled Mn(II) center. The second signal centered at g = 3.8 has 6 lines separated by 90 G reflecting an uncoupled, mononuclear Mn(II) center. These signals indicate that both mononuclear Mn(II) and binuclear centers are present in the DIMP treated sample.

EPR samples from the same stock of Mn/Mn-PTE were prepared with and without the addition of DIMP. The EPR signal for this stock of enzyme without DIMP is presented in Figure 25A and 26A, and does not show residual mononuclear Mn(II). The thermal stability and optimal kinetic activity of Mn/Mn-PTE at pH 8.0 do not support the spontaneous dissociation of Mn(II) from the active site. DIMP is not expected to chelate the Mn(II) ions from the enzyme active site since it lacks chelating functional groups. Therefore, the mononuclear Mn(II) EPR signals observed upon addition of DIMP are assigned to bound Mn(II) remaining in the active site and all changes in the spectrum report on interactions of DIMP with the metal center.

The EPR spectrum of PTE with the addition of DIMP reflects more than one active site species in the EPR sample. The decrease of the binuclear signal at g = 2.2 and appearance of mononuclear signal at g = 2.0 represent an active site species in which binding of DIMP results in breaking of the hydroxide bridge. The loss of binuclear signal in the EPR spectrum has previously been observed in Mn/Mn-PTE samples at lower pH and was determined to result from the loss of the hydroxide bridge which facilitated the coupling between the two metals (*23*). Temperature dependent spectra for Mn/Mn-PTE*DIMP (Figure 29) were collected and analyzed for the binuclear signal at g = 2.2 in the same manner as described for the Mn/Mn-PTE sample. The binuclear signal intensities at g = 2.2 and 4.3 for Mn/Mn-PTE*DIMP and Mn/Mn-PTE were plotted verses temperature (Figure 30). The temperature dependence for the binuclear

signal at g = 2.2 in the Mn/Mn-PTE*DIMP sample is nearly identical to that of Mn/Mn-PTE without addition of DIMP. Therefore, the binuclear signal at g = 2.2 reports on a relatively undisturbed binuclear center. Unlike the temperature dependence of the binuclear signal at g = 2.2, the binuclear signal at g = 4.3 exhibits a strong signal intensity at 3.6 K with maximum intensity around 4.6 K (Figure 29 and 30). A loss in signal intensity is observed above 7 K. The new signal at g = 4.3 is assigned to the S = 1 spin state based on the appearance of this binuclear signal at the lower temperature of 3.6 K and the enhanced temperature dependence of this signal relative to the Mn/Mn-PTE signal. The appearance of this signal is a subtle indication of DIMP association with the active site.

The appearance of both the binuclear and mononuclear Mn(II) EPR signals at g = 4.3 and 3.8 are assigned as $\Delta M_s = \pm 2$ forbidden transitions. The forbidden transition for the binuclear signal occurs between the M_s -1 and +1 levels within the S = 1 spin manifold. The mononuclear signal is assigned to the transition between the M_s -5/2 and (-1/2) levels. These half-field or forbidden transitions are observed for paramagnetic species in low symmetry environments. An increase in the zero-field parameter, D, reflects the lowering of symmetry at the metal center upon binding of DIMP and results in the observation of these forbidden transitions. The appearance of mononuclear Mn(II) EPR signal with additional half-field features at g = 3.8 does not appear to be due to the loss of hydroxyl bridge alone. An EPR spectrum of Mn/Mn-PTE at pH 6.0 reflects the loss of the hydroxyl bridge in the active site. No forbidden half-field transitions are observed in the spectrum. Therefore, the appearance of the new mononuclear signal is due to the presence of DIMP and not just loss of the hydroxyl bridge. The observation of forbidden transitions corresponding to both binuclear and mononuclear centers suggests that DIMP binding occurs at metal centers with and without the hydroxide

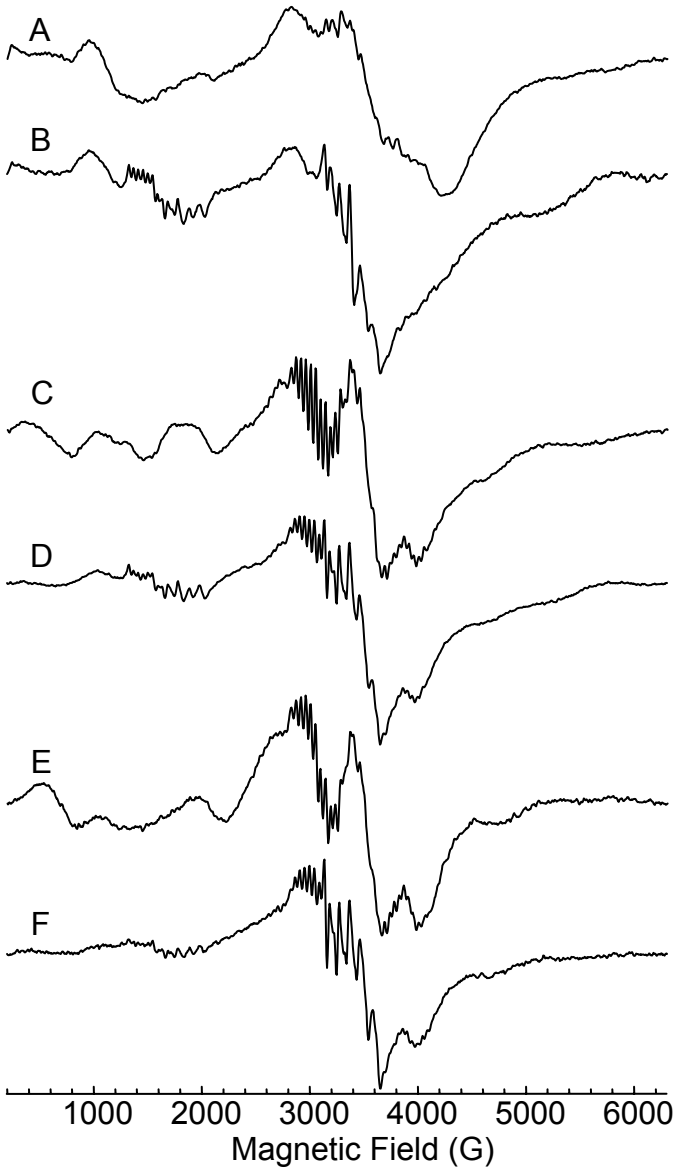

Figure 29. EPR spectra of Mn/Mn-PTE with and without the inhibitor DIMP at various temperatures. (A, C, E) 200 μM Mn/Mn-PTE, 10 scans (B, D, F) 200 μM Mn/Mn-PTE with 171 mM DIMP added, 3 scans (A, B) 3.6 K (C, D) 10 K (E, F) 40 K. All samples in 50 mM HEPES buffer, pH 8.0. EPR conditions: microwave power 2 mW, modulation amplitude 20 G.

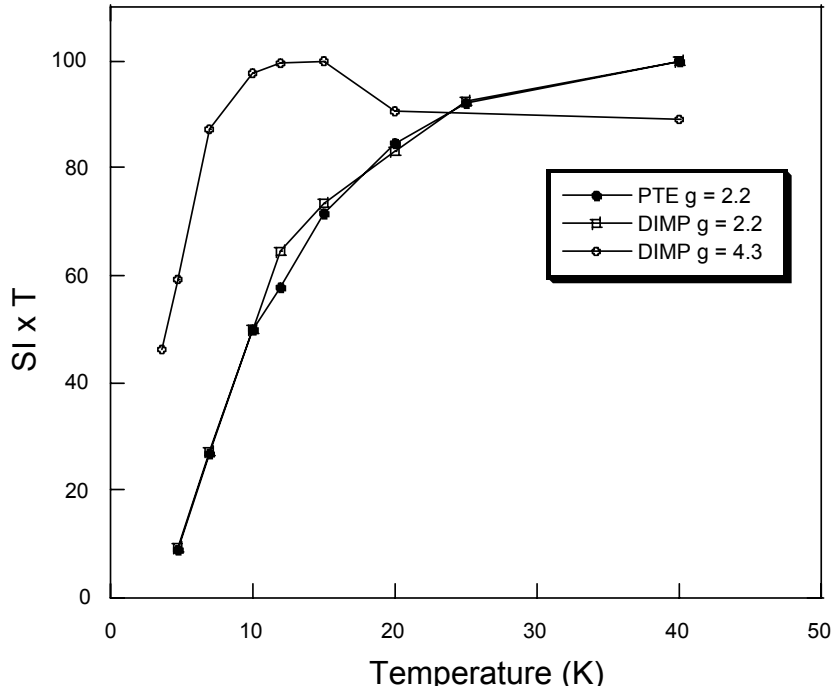

Figure 30. Temperature dependence of the binuclear signal at g = 2.2 and g = 4.3 of Mn/Mn-PTE*DIMP and Mn/Mn-PTE samples. EPR conditions: microwave power 2 mW, modulation amplitude 20 G.

bridge present. These two active site species account for all species observed in the EPR spectrum for Mn/Mn-PTE*DIMP. The decrease in the broad absorbances at g = 14.6, g = 5.8, and g = 3.7 in the spectrum (Figure 25B) is attributed to a distribution of zero field splitting energies resulting from variations in metal-ligand coordination among the multiple species in the sample. This distribution of energies is referred to as D-strain and can broaden transitions to the extent of loss of observable signal.

*EPR Spectrum of Mn/Mn-PTE*TEP.* The inhibitor triethyl phosphate (TEP) was added to Mn/Mn-PTE at a final concentration of 350 mM which exceeds ten times the K_i values previously determined for Zn(II)- and Cd(II)-substituted PTE (*80*). The addition of TEP to the enzyme resulted in three major changes in the EPR spectrum (Figure 25C and 26C). The first change is the decrease of binuclear signal at g = 2.2 and gain of mononuclear signal at g = 2.0 which is attributed to the loss of the hydroxide bridge upon addition of TEP. The second change is the appearance of a forbidden transition at g = 4.3 consisting of an 11-line splitting separated by 45 G indicative of a spin-coupled Mn(II) center. Unlike the Mn/Mn-PTE*DIMP spectrum, no half-field feature from a mononuclear signal is observed at g = 3.8. The binuclear signal at g = 4.3 is readily observed at 3.6 K with a maximum intensity around 4.7 K and decreases in intensity above 7 K (Figure 31). The temperature dependence of the binuclear signals at g = 2.2 and 4.3 for Mn/Mn-PTE with and without TEP are plotted in Figure 32. The temperature dependence of the binuclear signal at g = 2.2 corresponds with the temperature dependence observed for Mn/Mn-PTE indicating that the exchange coupling in the binuclear center is unchanged. As observed for the Mn/Mn-PTE*DIMP sample, an enhanced temperature dependence is observed for the binuclear signal at g = 4.3, and it is assigned to the S = 1 spin state. The signal is assigned to the forbidden transition between the M_s -1 and +1 levels within the S = 1 manifold and reflects binding of TEP to

the spin-coupled metal center. The appearance of a forbidden transition upon inhibitor binding results from an increase in zero-field splitting parameter upon lowered symmetry at the metal center. The binuclear signal at g = 4.3 in the Mn/Mn-PTE*DIMP spectrum appears stronger than in the Mn/Mn-PTE*TEP spectrum (Figure 29D and 31D) and is due to a greater concentration of binuclear species in the sample, which is observed by comparing the amount of binuclear signal at g = 2.2 in the two samples. The absence of the half-field feature for a mononuclear Mn(II) signal at g = 3.8 in the Mn/Mn-PTE*TEP spectrum suggests a higher symmetry at the uncoupled metal center than observed for the Mn/Mn-PTE*DIMP sample. This may result from a weaker coordination of TEP to the mononuclear Mn(II) metal center due to distance or a difference in position about the metal center. Broadening of transitions at g = 14.6, g = 5.8, and g = 3.7 is observed in the Mn/Mn-PTE*TEP spectrum (Figure 25C) and is attributed to an increase in D-strain.

The third change in the EPR spectrum of Mn/Mn-PTE*TEP is the appearance of a new signal at g = 1.7 observed at temperatures from 3.6 K to 15 K (Figure 31). This signal is not present in the spectrum from the original enzyme stock shown in Figure 25A. Therefore, this new signal is not due to a change in the stock enzyme sample. The temperature dependence of this signal could not be accurately determined due to the presence of underlying binuclear signal of Mn/Mn-PTE. In an attempt to characterize this new EPR signal, the temperature was held constant at 3.6 K, where there is little population of the signal from the binuclear Mn/Mn-PTE, and the power at which the sample was collected was varied from 5 μW to 80 mW (Figure 33). At 5 μW, the only appreciable signal remaining is the mononuclear Mn(II) signal at g = 2.0. As power is increased, the signal in question begins to appear and dominates the spectrum at 80 mW

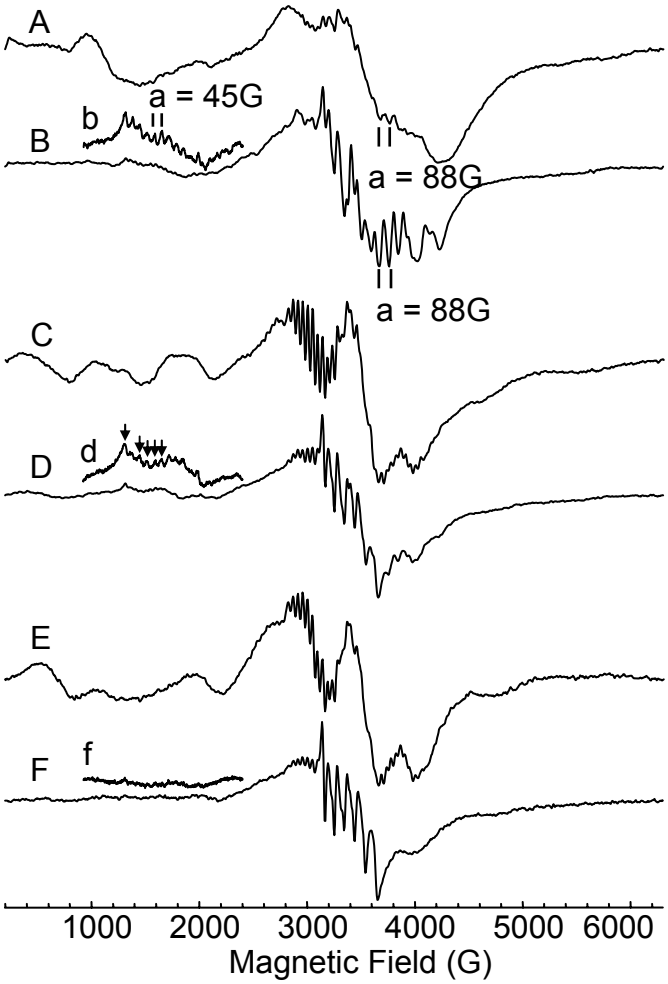

Figure 31. EPR spectra of Mn/Mn-PTE with and without the inhibitor TEP at various temperatures. (A, C, E) 200 μM Mn/Mn-PTE, 10 scans (B, D, F) 130 μM Mn/Mn-PTE with 350 mM TEP added, 5 scans (A, B) 3.6 K (C, D) 10 K (E, F) 40 K. Inset: (b, d, f) Expanded region of 2000 to 4500 G, 20 scans, arrows designate peaks used to determine signal intensity. All samples in 50 mM HEPES buffer, pH 8.0. EPR conditions: microwave power 2 mW, modulation amplitude 20 G.

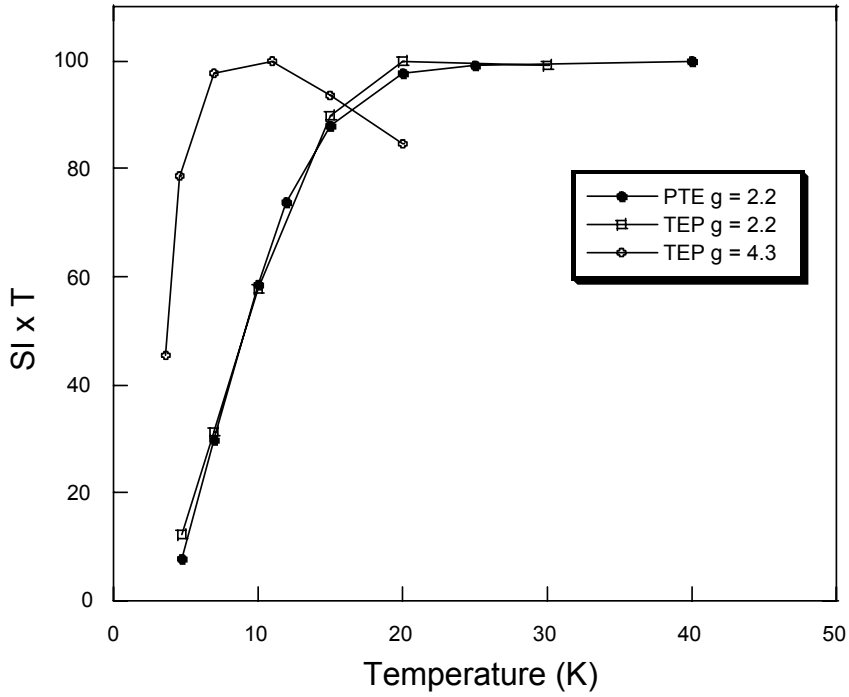

Figure 32. Temperature dependence of the binuclear signal at g = 2.2 and g = 4.3 of Mn/Mn-PTE*TEP and Mn/Mn-PTE samples. EPR conditions: microwave power 2 mW, modulation amplitude 20 G.

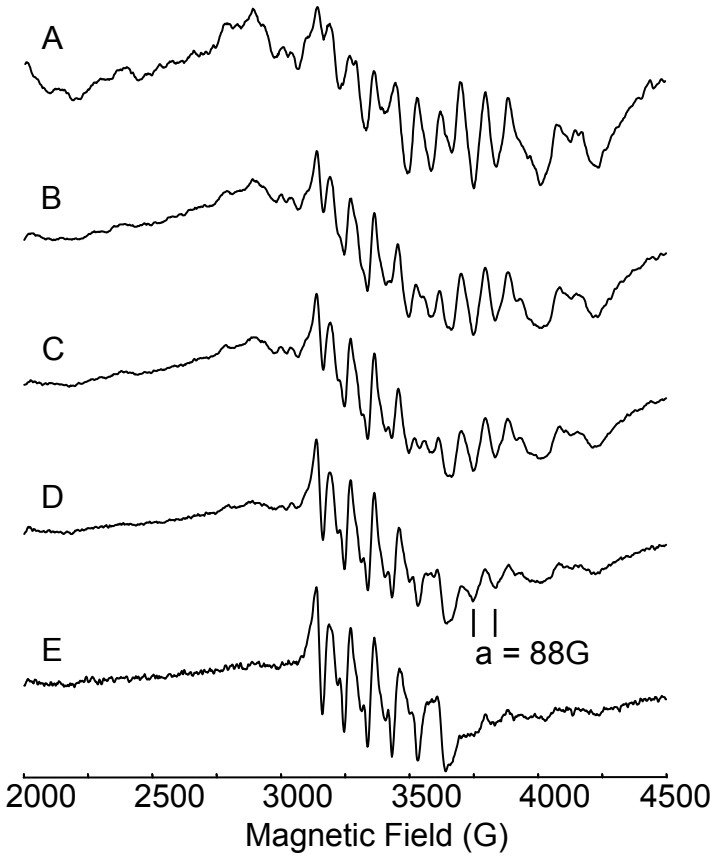

Figure 33. EPR spectra of Mn/Mn-PTE*TEP sample at various powers. (A) 80 mW (B) 2 mW (C) 0.6 mW (D) 0.08 mW (E) 0.005 mW. 130 μM Mn/Mn-PTE and 350 mM TEP in 50 mM HEPES buffer, pH 8.0. EPR conditions: temperature 10 K, modulation amplitude 20 G, 5 scans.

power with the mononuclear signal still present. Two peaks from the new signal at g = 1.7 do not overlap with the mononuclear signal at g = 2.0. The two peaks are separated by 88 G. Splittings of 88 G are observed for mononuclear Mn(II) in a six-line pattern typically centered at g = 2. The number of splittings for this new signal cannot be determined due to the overlap of the mononuclear signal at g = 2.0. While the signal is distinctive from the six-line mononuclear signal at g = 2.0, analysis of this signal is inconclusive due to the inability to separate the two signals. Upon closer inspection of an untreated Mn/Mn-PTE sample at 3.6 K, two peaks separated by 88 G and lying at the same field position as those observed for the new signal were identified. These two peaks are almost lost in the dominant absorbance of a broad signal spanning the g = 1.7 region. Binding of TEP to the metal center of Mn/Mn-PTE may increase the D-strain in the system and broaden this signal allowing the hyperfine splittings at g = 1.7 to be observed. Aside from the two peaks, the origin of the features in this signal as Mn/Mn-PTE or Mn/Mn-PTE*TEP cannot be distinguished.

*EPR Spectrum of Mn/Mn-PTE*DEP.* Diethyl phosphate (DEP), a product of paraoxon hydrolysis, was added to the enzyme at a final concentration exceeding ten-fold the K_i value determined for the product. The EPR spectrum at 10 K reveals a loss of the binuclear signal at g = 2.2 and the appearance of mononuclear signal at g = 2.0 (Figure 25D and 26D). While this result is also observed upon addition of both DIMP and TEP to the enzyme, the spectrum of enzyme with DEP is unchanged in the low field region where forbidden transitions at g = 4.3 and 3.8 were observed in the presence of the inhibitors (Figure 26D). The loss of binuclear signal and gain in the mononuclear Mn(II) signal is assigned to the loss the hydroxyl bridge. No additional changes are observed in the EPR spectrum. The absence of forbidden transitions in the Mn/Mn-PTE*DEP spectrum suggests that the interaction between the product and the metal

center differs from the interaction between the inhibitors and enzyme active site. The spectra obtained at different temperatures are shown in Figure 34 and the temperature dependence of the binuclear signal at g = 2.2 is plotted in Figure 35. The temperature dependence of the binuclear signal in the Mn/Mn-PTE*DEP sample is similar, but not identical to the dependence exhibited by the enzyme stock. The Mn/Mn-PTE*TEP and Mn/Mn-PTE*DEP samples were made using the same stock of enzyme. For further comparison, the temperature dependence of the signal at g = 2.2 for Mn/Mn-PTE, Mn/Mn-PTE*DEP, and Mn/Mn-PTE*TEP are plotted in Figure 35. It is not clear why there is a slight temperature deviation in the temperature dependence of the Mn/Mn-PTE binuclear signal when DEP is added.

DISCUSSION

Four EPR spectra have been presented in order to investigate the interaction of inhibitor and product with the metal center of Mn/Mn-PTE. The goal of this study is to further an understanding of the mechanism by which organophosphate hydrolysis occurs within the active site of PTE. A schematic representation summarizing the different species present within the active site of Mn/Mn-PTE upon addition of inhibitor or product is shown in Figure 36. Concentrations surpassing 10-fold the K_i value for each inhibitor and product produced a sufficient amount of species within the active site to observe the influence of each on the metal center. The use of substrates to trap further intermediates was attempted without success due to complete turnover of substrate by enzyme. The solubility of substrates at millimolar concentrations was another limitation in the use of substrates in this EPR investigation.

Inhibitor Binding at the Metal Center of Mn/Mn-PTE. The EPR spectra for Mn/Mn-PTE*DIMP and Mn/Mn-PTE*TEP reflect two species in which inhibitor is bound at the metal center. The first species is represented in Figure 36A as inhibitor

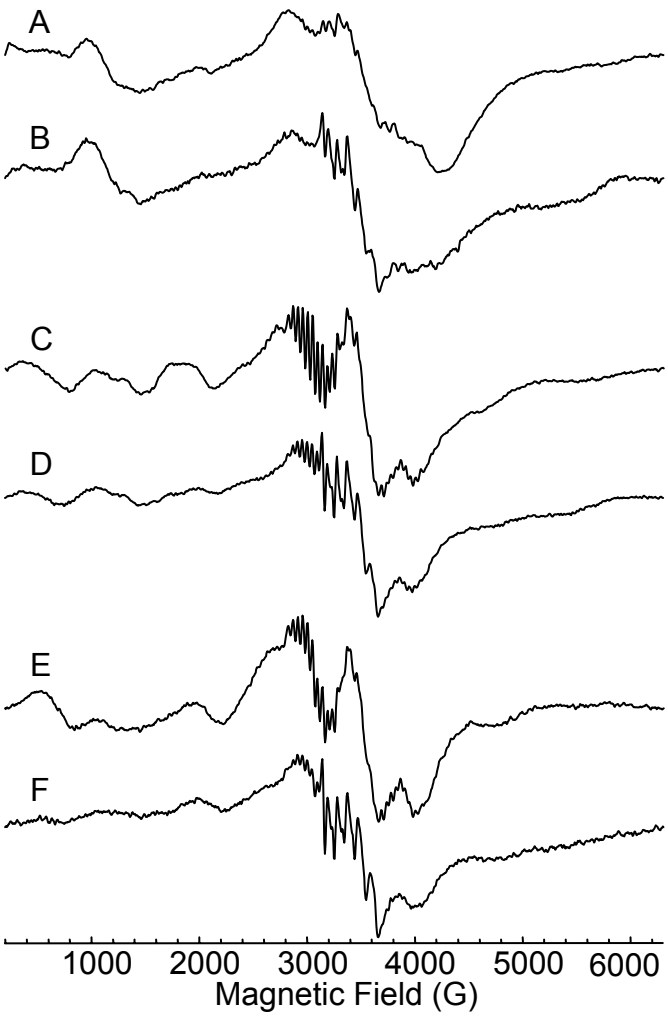

Figure 34. EPR spectra of Mn/Mn-PTE with and without the inhibitor DEP at various temperatures. (A, C, E) 200 μM Mn/Mn-PTE, 10 scans (B, D, F) 115 μM Mn/Mn-PTE with 350 mM DEP added, 8 scans (A, B) 3.6 K (C, D) 10 K (E, F) 40 K. All samples in 50 mM HEPES buffer, pH 8.0. EPR conditions: microwave power 2 mW, modulation amplitude 20 G.

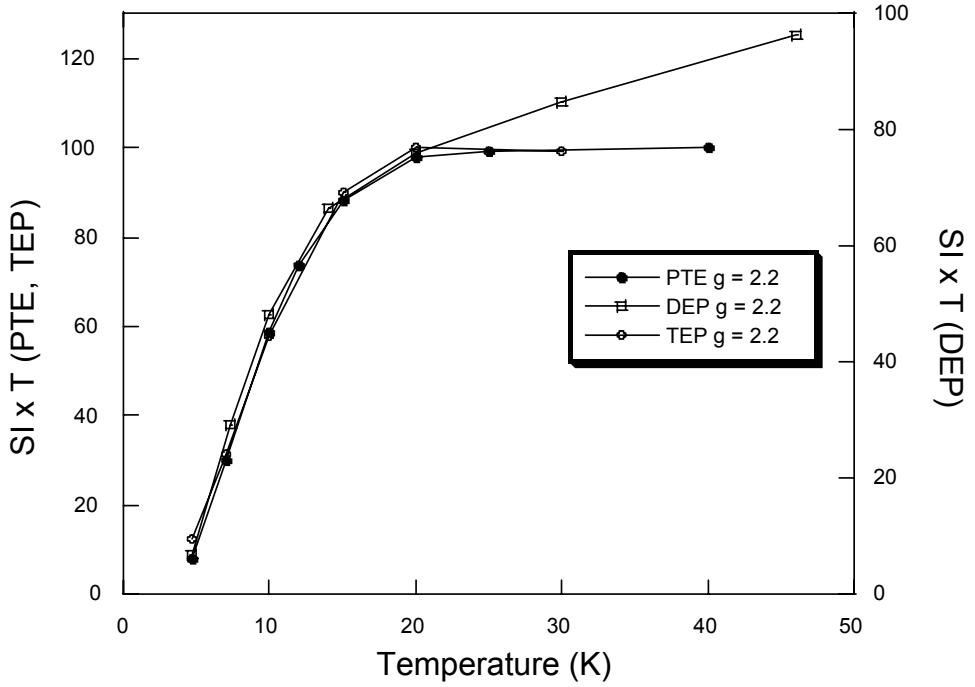

Figure 35. Temperature dependence of the binuclear signal at g = 2.2 of Mn/Mn-PTE*DEP and Mn/Mn-PTE samples. EPR conditions: microwave power 2 mW, modulation amplitude 20 G.

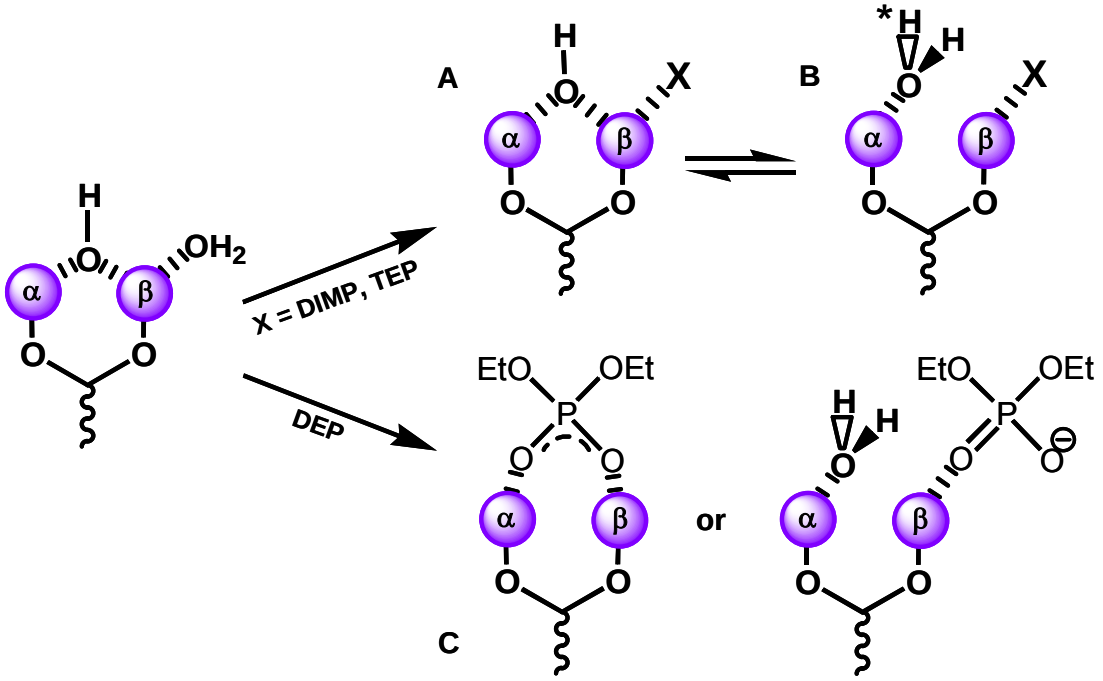

Figure 36. Proposed binding of DIMP, TEP, and DEP to the metal center. (far left) The resting state of the enzyme is represented by the active site metals with a terminally bound water ligand and the hydroxyl and carboxyl bridges. (A) Terminal water is displaced by DIMP or TEP. (B) Terminal water is displaced by DIMP or TEP with loss of the hydroxyl bridge to a terminally bound water or *hydroxide. (C) Two possible binding modes: DEP forms a bidentate bridge displacing the hydroxyl bridge and the terminally bound water; DEP displaces terminal water with loss of the hydroxyl bridge.

bound to the metal center with the hydroxyl bridge present. In both spectra of inhibited enzymes, an 11-line hyperfine splitting separated by 45 G associated with an exchange-coupled Mn(II) center is observed at g = 4.3 as a forbidden transition (Figure 25B,C and 26B,C). The appearance of this forbidden transition indicates that a bridging species is present that experiences an electronic environment that has lower symmetry in the presence of inhibitor. This signal has been observed for other binuclear enzymes, such as bacterophage λ protein phosphatase and dinitrogenase reductase-activating glycohydrolase, and in dinuclear Mn(II) complexes (*40, 49, 83*). The temperature dependence of this signal is enhanced in comparison to the binuclear signal at g = 2.2 for Mn/Mn-PTE, which arises from the S = 2 spin manifold, and is assigned to a transition from the lower S = 1 spin manifold. A new set of allowed transitions with enhanced temperature dependence are not observed in the spectra. This indicates that a new species associated with weaker exchange coupling and an energetically different spin manifold is not represented in the sample.

The observed double quantum transition indicates an increase in the zero-field parameter associated with the exchange coupled Mn(II) center. The increase in zero-field splitting is attributed to the replacement by phosphonate of a water ligand coordinated to one of the metals. Crystal structures of PTE with DIMP and TEP reveal that the phosphoryl oxygen of the inhibitors is present in place of a water ligand (*47*). Unlike the smaller water ligand, binding of inhibitor at the active site is dictated by three binding pockets and may orient this ligand differently at the metal than the water (*81*). This difference may result in a ligand field with lower symmetry and an increase in the zero-field parameter. The resolved hyperfine of this transition may indicate a more rigid metal-metal distance upon inhibitor binding. Spectral simulations preformed by Hendrich and coworker for an exchange coupled Mn(II) complex demonstrated that

reduction in the variation of metal-metal distance, or r-strain, in the simulation resulted in the resolution of hyperfine not otherwise observed in the experimental spectrum of a binuclear complex (*83*).

It is not possible to distinguish to which metal the inhibitors are bound from these spectra alone. Crystal structures of Zn/Zn-PTE with DIMP and TEP bound in the active site reveal the presence of the hydroxyl bridge and the phosphoryl oxygen of each inhibitor to be 2.5 Å and 3.4 Å from the β-metal, respectively (*47*). The phosphoryl center of DIMP is 3.3 Å from the oxygen of the undisturbed hydroxyl bridge. Binding of the inhibitor at the β-metal places the phosphorus center in line with the hydroxyl bridge which would facilitate nucleophilic attack for hydrolysis of substrate. Binding of substrate to metal is supported by kinetic studies in which substrate hydrolysis was influenced by polarization of the phosphoryl-oxygen resulting from direct ligation to the metal center (*13*).

The second species present in the Mn/Mn-PTE*DIMP and Mn/Mn-PTE*TEP samples is represented in Figure 36B. The binding of inhibitor to the metal center with loss of the hydroxyl bridge is identified by the loss of the multiple 11-line hyperfine splittings separated by 45 G at g = 2.2 arising from exchange-coupled Mn(II) center and gain of the six-line hyperfine splitting of 90 G from mononuclear Mn(II) ions at g = 3.8 and 2.0. The signal at g = 3.8 is observed in the Mn/Mn-PTE*DIMP spectrum and arises from a double quantum transition indicating one or both Mn(II) ions has lowered symmetry. The EPR spectrum reflecting the loss of the hydroxyl bridge in the absence of inhibitor has been observed for Mn/Mn-PTE at low pH and does not exhibit forbidden transitions; therefore, the signal at g = 3.8 in the Mn/Mn-PTE*DIMP spectrum is due to inhibitor binding. DIMP bound to the uncoupled metal center increases the zero-field parameter enabling the observation of the double quantum transition. As mentioned

previously, the increase in zero-field parameter is attributed to the coordination of the phosphonate in place of a water ligand. EPR spectra of other binuclear metalloenzymes with double quantum transitions from a mononuclear Mn(II) ion have been observed for ribonucleotide reductase, methionyl aminopeptidase, and bacteriophage λ phosphoprotein phosphatase (*38, 41, 84*).

The EPR spectrum for bacteriophage λ phosphoprotein phosphatase (λPP) showed an increase in the observed forbidden transition upon a single O/N atom substitution in the ligand field via an asparagine (oxygen) to histidine (nitrogen) mutation (*85*). While there is not a crystal structure for this mutant, the effects of this substitution on a binuclear metal center can be inferred from the crystal structures of wild-type arginase and the mutant, H101N (*86*). Minor differences were observed between nitrogen and oxygen ligation at the binuclear center. The EPR spectrum for the asparagine to histidine mutation demonstrates the ability to observe small changes in ligand field by EPR spectroscopy. Therefore, it is reasonable to assign a change in the ligand field upon displacement of water with DIMP in Mn/Mn-PTE to the observed EPR spectral changes.

The absence of the forbidden transition at g = 3.8 for a mononuclear signal distinguishes the binding of TEP as slightly different from that observed for DIMP. This may be due to a weaker coordination of TEP at the metal center. The crystal structures of enzyme with inhibitor have shown that the phosphoryl oxygen of TEP is located 1 Å further from the β-metal than the phosphoryl oxygen of DIMP (*47*). A weaker coordination would reduce the zero-field parameter so that only allowed transitions are observed.

A change in the equilibrium between the bridged and non-bridged hydroxyl species upon inhibitor binding is reflected in the EPR spectrum of Mn/Mn-PTE with two

different inhibitors. The observation of both species indicates that the equilibrium no longer favors the bridged species. The replacement of terminally bound water with a phosphonate could result in an electronic difference that destabilizes the bridged species. The stabilization of the non-bridged species may result from an adjustment in the metal-metal distance. The shift in equilibrium induced by inhibitor binding suggests substrate binding at the metal center would induce an analogous shift in equilibrium resulting in a terminally bound hydroxyl poised for nucleophile attack on the substrate.

Influence of Product on the Metal Center of Mn/Mn-PTE. The presence of DEP at the metal center is indicated by the decrease of binuclear signal and gain in mononuclear signal around g = 2. The decrease of the exchange coupled Mn(II) signal reflects loss of the hydroxyl bridge. The absence of observed forbidden transitions suggests that the change in the zero-field parameter or ligand field is negligible compared to the change in ligand field with DIMP or TEP present. A reduction in the exchange coupling upon addition of phosphate has also been observed by EPR for the dimanganese center of λPP. The overall spectrum for λPP was less affected by phosphate addition in comparison to spectra of single point mutation of residues coordinated to the metal core. The Mn/Mn-PTE*DEP and λPP*phosphate spectra reveal the disruption of the solvent bridge by a phosphate and a less pronounced effect on the ligand field than observed with other coordinating ligands. Potential binding of DEP as either monodentate or bidentate ligation to the metal center without the hydroxyl bridge is presented in Figure 36C.

Support for the bidentate binding of DEP is found in the crystal structure of PTE from *Agrobacterium radiobacter* in which catalytic hydrolysis of substrate resulted a bidentate coordination of the product, dimethyl thiophosphate, at the metal center (*87*). Binding of this product revealed the phosphoryl sulfur bound 2.5 Å from the β-metal,

which is consistent with the phosphoryl oxygen position of DIMP at the β-metal. In the former case, the hydroxyl bridge is present with product bound, and in the latter case, this is also observed in the crystal structures of PTE with DIMP and TEP. The EPR data presented in this work supports a shift in equilibrium toward comparable amounts of bridge and non-bridged hydroxyl species present upon binding of DIMP or TEP, and does not exclude the same shift in equilibrium upon product binding. Therefore, bridged and non-bridged hydroxyl species may be equally represented with product bound.

Crystal structures of other binuclear enzymes with phosphate and sulfate bound at the active site support binding represented in Figure 36C. Bidentate coordination of phosphate has been observed for purple acid phosphatase (*88, 89*). Crystal structures of purple acid phosphatase and λPP with sulfate bound exhibit both terminal and bridged coordination to the metal center (*27, 90*).

This work concludes that binding of inhibitor occurs at the metal center and results in an increase of non-bridged hydroxyl species. These results in conjunction with kinetic and crystallographic data suggest that substrate binding via the phosphoryl oxygen at the β-metal weakens the hydroxyl bridge coordination to the β-metal. This loss of coordination would increase the nucleophilic character of the bridge and result in a stronger nucleophile for hydrolysis.

CHAPTER V

IRON(II)-SUBSTITUTED PHOSPHOTRIESTERASE

Phosphotriesterase, a member of the amidohydrolase superfamily, hydrolyzes of a wide variety of organophosphates used as pesticides and chemical warfare agents. Hydrolysis of these nerve agents by PTE occurs at rates approaching the diffusion control limit and may be promising in the prevention of acetylcholinesterase inactivation. The enzyme has a binuclear zinc(II) active site consisting of four histidine residues, an aspartate residue, a carboxylated lysine bridge, and a hydroxyl bridge (*5*). The metal center facilitates substrate binding and activation of the solvent for nucleophilic attack. The hydroxyl bridge has been identified as the attacking nucleophile in hydrolysis (*23*). Substitution of the native metal with Co(II), Mn(II), Ni(II), or Cd(II) sustains the catalytic activity of the enzyme (*10*). Both metals are required for activity and bind to the active site with similar affinities (*10, 46*). The rate of substrate turnover has been observed to be as high as 10^4 s^{-1} with catalytic efficiencies of 10^7 M^{-1} s^{-1}. Interestingly, substitution of the enzyme with Fe(II) or Cu(II) has not resulted in activity toward the hydrolysis of organophosphate triesters (*10*). In previous studies, catalytic activity for Fe(II)-substituted PTE was investigated under aerobic conditions leaving open the possibility of inactivation of the enzyme by Fe(II) oxidation. This work investigates the catalytic activity of Fe(II)-substituted PTE under anaerobic conditions.

MATERIALS AND METHODS

Materials. All chemicals were purchased from Sigma except for N-(2-hydroxyethyl)piperazine-N'-2-ethane-sulfonic acid (HEPES), which was purchased from

United States Biochemical. Bacterial cell growth protocols, enzyme purification, and preparation of apoenzyme were performed as previously described (*10, 54*).

Reconstitution of Apoenzyme. Degassed enzyme and solutions were placed under argon in a refrigerated 2MBraun glove box. Oxygen was removed from the enzyme and solution stocks by placing them under vacuum while stirring. The stocks were considered degassed when the release of gas from solution was no longer observed for ~10 minutes. All glassware was washed in 30% nitric acid to avoid metal contamination. Apoenzyme was reconstituted in the glove box upon addition of Fe(II) or Zn(II) from 50 mM $Fe(NH_4)_2(SO_4)_2$ or 50 mM $ZnCl_2$ stock solutions. The iron stock solution was made in the glove box using $Fe(NH_4)_2(SO_4)_2$ stored under nitrogen and degassed double distilled water. After reconstitution, the enzyme was loaded onto a PD10 column to remove metal not bound to the enzyme. Hydrolase activity was assayed for the apo-, reconstituted, and PD-10 treated protein using the substrate paraoxon under both aerobic and anaerobic conditions. In one case, additional Fe(II) was added to the reconstituted protein. After 24 hours, the enzyme was loaded onto a PD-10 column. Hydrolase activity was assayed for the samples in which Fe(II) was added to the reconstituted and PD-10 treated protein.

Metal Analysis. The metal content of all samples was determined using a Perkin Elmer DRCII inductively coupled plasma mass spectrometer. Samples were run in triplicate. All metal concentrations were within the range of the standards, 2 - 200 ppb.

Assay Conditions. The specific activity, units/mg, was determined by monitoring the change in absorbance at 400 nm upon hydrolysis of 1 mM paraoxon to *p*-nitrophenol ($\varepsilon_{400} = 1.7 \times 10^4\ M^{-1}\ cm^{-1}$) and diethyl phosphate in 100 mM HEPES buffer at 25 °C. One unit of activity is defined as the hydrolysis of 1.0 μmol of paraoxon per minute. Assays performed under aerobic conditions were monitored with a $Spectra_{Max}$ PLUS 384

from Molecular Devices. The SI 400 spectrometer from Spectral Instruments was used for assaying activity under argon in a non-refrigerated 2MBraun glove box. Hydrolysis of paraoxon by Co(II)-substituted PTE was monitored under aerobic and anaerobic conditions as a control for instrumental comparison.

RESULTS

Attempt 1. The catalytic activities and metal contents of Fe(II)- and Zn(II)-substituted PTE are presented in Table 2. The first reconstitution experiment was performed under aerobic conditions. Fe(II) was added to the apoenzyme and stored at 4°C for 24 hours. An initial contamination of 0.2 equivalent Zn(II) per active site was present in the apoenzyme sample. After reconstitution, the enzyme stock was divided in half. Additional Fe(II) was added to one half and the sample was stored for another 24 hours. Treatment of both samples with the desalting column resulted in 92% and greater retention of metal present in the reconstituted samples. The elution of samples through a PD-10 column introduced additional Zn(II) contamination. Therefore, the slight increase in specific activity expressed in U/mg observed in these samples is attributed to an increase in Zn(II) contamination. The increase in activity is less than what is expected for the equivalents of Zn(II) present in the sample based on previously reported values for Zn/Zn-PTE. This may reflect the presence of a Zn/Fe-PTE species.

Attempt 2. After addition of Fe(II), the protein was stored for 15 days at 4°C before removal of unbound metal. Greater than 90% of the Fe(II) present in the reconstituted sample was retained by the enzyme. An initial contamination of 0.2 equivalent Zn per active site was present in the apoenzyme sample. The Zn(II) content after elution through a PD-10 column was similar to the apoenzyme and considered constant. The Fe(II)-reconstituted enzyme has a specific activity of 200 U/mg, as observed for samples reconstituted in attempt 1.

Table 2. The catalytic activities and metal binding for apoenzyme, metal reconstituted enzyme, and metal reconstituted enzyme after elution through a desalting column.

Attempt 1 - (under air)	U/mg x10^3 ±0.1	Eq. Zn/PTE*	Eq. Fe/PTE*	Reconstitution
apo-PTE	0.04	0.2	0.0	
Reconstituted Fe-PTE	0.2	0.1	0.5	1 day
PD-10 Fe-PTE	0.4	0.7	0.5	
Reconstituted Fe-PTE (additional Fe)	0.2	0.4	1.3	
PD-10 Fe-PTE (additional Fe)	0.4	0.6	1.2	
Attempt 2 - (under argon)				
apo-PTE	0.07	0.2	0.0	
Reconstituted Fe-PTE	0.2	0.1	2.0	15 days
PD-10 Fe-PTE	0.2	0.2	1.8	
Attempt 3 - (under argon)				
apo-PTE (Fe reconstitution)	0.2	0.3	0.0	
Reconstituted Fe-PTE	0.2	0.2	1.0	3 days
PD-10 Fe-PTE	0.2	0.2	0.8	
apo-PTE (Zn reconstitution)	0.1	0.3	0.0	
Reconstituted Zn-PTE	1.7	1.6	0.0	3 days
PD-10 Zn-PTE	2.2	1.8	0.0	

* Equivalent per monomer

Attempt 3. In order to remove the 0.2 equivalent Zn(II) per active site present in the apoenzyme samples, 1,10-phenanthroline was add to the enzyme stock solution. The chelator was separated from the enzyme by elution through a PD-10 column. Removal of Zn(II) was unsuccessful with 0.2 equivalent Zn(II) per active site retained in the apoenzyme samples. The enzyme was split into two samples for reconstitution with Fe(II) and Zn(II). After addition of metal, the enzyme was stored for 3 days at 4°C before elution through a PD-10 column. Greater than 80% of the Fe(II) and 100% of the Zn(II) remained bound to the enzyme. In this case, the activity of the Fe(II) reconstituted enzyme is comparable to the "apoenzyme" that has Zn contamination. By contrast, the activity of the Zn(II) reconstituted enzyme increased greater than ten fold with a specific activity of ~2,000 U/mg that corresponds with previously reported values (*10*). The Zn(II) reconstituted enzyme is catalytically active, while the Fe(II) reconstituted enzyme is considered inactive.

DISCUSSION

Reconstitution and activity of Fe-substituted PTE was evaluated under both aerobic and anaerobic conditions. Greater than 80% of Fe(II) that was added to apoenzyme remained bound under both aerobic and anaerobic conditions. Under aerobic conditions, an increase of the apoenzyme activity was observed for enzyme containing 0.5 equivalents of Fe(II) per monomer. No change in activity was observed upon increasing the Fe(II) content to 1.3 equivalents. Under anaerobic conditions, an increase in activity of only 3 times that of the apoenzyme was observed with 2 equivalents Fe(II) present per monomer. An increase in activity is not observed upon reconstitution under anaerobic conditions or upon an increase in equivalent of Fe(II) bound. The activities observed for the Zn(II)-reconstituted enzyme were comparable to previously reported values obtained under aerobic conditions (*10*). These results

confirm the integrity of the reconstituted and PD-10 treated enzymes, and show that Fe(II)-reconstituted activity is < 10 % of that found for the Zn(II)-reconstituted enzyme.

It is not obvious why Fe/Fe-PTE is not catalytically active. The coordination of Fe(II) in the active site is not expected to differ greatly from the environment of transition metals that exhibit activity. The radius of an Fe(II) ion is 0.76 Å, which falls between the radii of 0.74 Å and 0.97 Å for Zn(II) and Cd(II) ions, respectively (*91*). The Fe(II) ion is a borderline hard/soft metal (*92*). Reconstitution of PTE with hard and soft metals has been demonstrated with Mn(II) and Cd(II)-substituted enzymes (*5*). Crystal structures of Zn/Zn-, Mn/Mn-, Cd/Cd-, and Zn/Cd-subsituted PTE reveal both distorted trigonal bipyramidal and distorted octahedral metal geometries (*5*). In biological systems, Fe(II) is often observed with these symmetries, therefore, the coordination environment provided by PTE is expected to accommodate the Fe(II) ion (*93, 94*). While the magnetic coupling of the Fe/Fe-PTE center has not been determined, a coupled metal center does not guarantee catalytic activity for PTE. Cu(II)-substituted PTE is not catalytically active but does have a spin-coupled Cu(II) center as determined by EPR (*54*). The coordination of water to two Fe(II) or Cu(II) ions is expected to lower the pK_a of water and produce the hydroxyl bridge required for catalytic activity (*94*).

Enzymes with binuclear metal centers have demonstrated catalytic activity with Fe(II) ions. However, most of these enzymes either contain a mixed valent metal center or undergo a change in oxidation state during catalytic turnover of substrate. The enzymes that have the former include purple acid phosphatase and glyoxalase II, and those that exhibit the later include methane monooxygenase, ribonucleotide reductase, and hemerythrin (*35, 61, 95-97*). Enzymes which contain divalent metal centers that undergo no change in oxidation state include urease, dihydroorotase, and arginase (*25, 28, 98*). Urease and dihydroorotase, members of the amidohydrolase superfamily, have

no reported catalytic activity upon reconstitution of apoenzyme with Fe(II) ions (*30, 99*). Hellerman and coworker have reported that arginase may be catalytically activated with Fe(II), but extensive characterization of the Fe(II)-substituted enzyme has not been preformed (*100*). The present work concludes Fe/Fe-PTE is not catalytically active, but can bind up to 2 equivalent Fe(II) ions per active site.

CHAPTER VI

CONCLUSIONS

In this work, EPR spectroscopy was utilized to probe the metal center of Mn/Mn-PTE in order to further understanding of the mechanism for organophosphate hydrolysis by the enzyme. This was accomplished by the investigation of the solvent bridge identity, evaluation of inhibitor and product binding to the metal center and assessment of the activity and metal bind of Fe(II)-substituted PTE.

The presence of a solvent bridge between the two metals within the active site was previously identified by X-ray crystallography, but the protonation state of the bridge was unknown (*5*). EPR spectroscopy was utilized to monitor the effects of low pH on the solvent bridge of Mn(II)-substituted PTE and correlate this with a kinetic pK_a for the enzyme. The binuclear EPR signal associated with a spin coupled Mn(II) center is readily observed at catalytically active pH of 7.5 and higher. As the pH is lowered to 6.0, the intensity of the binuclear signal is reduced indicating that the bridging solvent is no longer present to facilitate spin coupling between the two metals. Protonation of the bridge distinguishes it as a bridging hydroxide and not a bridging water. The concentration of the hydroxyl bridged enzyme, representing the deprotonated state, was determined at several pH values by quantitation of the binuclear EPR signal. These values obtained over a range of pH values were utilized to determine a pK_a value of 7.3 ± 0.1 for the bridge. This value correlates with the kinetic pK_a of 7.1 ± 0.1 determined from the pH-rate profile for Mn/Mn-PTE. The kinetic profile revealed that the protonation of a single species within the active site was responsible for reduction in catalytic activity at low pH. The agreement between the EPR and kinetic pK_a values

identifies the hydroxyl bridge as the protonated species responsible for reduction of activity at low pH.

Reversible protonation of the hydroxyl bridge was demonstrated by the conversion of mononuclear signal to binuclear signal upon raising the pH of the sample. This result indicates that the two Mn(II) ions remain in the active site or at least in close proximity after loss of the bridging hydroxide species.

The notable influence of metal identity on the catalytic activity and substrate affinity for the enzyme suggested substrate may bind to the metal center (*10*). In lieu of the extreme efficiency in substrate hydrolysis by PTE, inhibitors were used to evaluate binding of substrate to the metal center and access implications for substrate-metal interaction. Changes in the EPR spectrum upon addition of the inhibitors diisopropyl methyl phosphonate (DIMP) and triethyl phosphate (TEP) were examined to confirm inhibitor binding to the metal center and identify the influence of inhibitor on the hydroxyl bridge and metal center. In both cases, the appearance of forbidden EPR transitions in the EPR spectra of the binuclear center upon inhibitor addition reflected lower symmetry about the metal center upon inhibitor coordination. The reduction in the amount of binuclear Mn(II) signal and appearance of mononuclear Mn(II) signal that includes a forbidden transition upon DIMP coordination reflected the loss of the hydroxyl bridge and appearance of a uncoupled metal center with lower symmetry. The temperature dependence of each spectrum was utilized to search for changes in the strength of the exchange coupling in inhibitor bound bridged PTE, as well as, to identify the spin manifold from which the forbidden transitions arise. The strength of the exchange coupling between the metals was unchanged from that observed for Mn/Mn-PTE in the absence of inhibitor; therefore, inhibitor binding induces a change in symmetry and a more facile loss of the bridge, but no change in the bridging itself. The

temperature dependences of the forbidden transitions are distinctly different from that observed for the S > 2 binuclear signal, and therefore, the forbidden transitions are assigned to arise from the S = 1 spin manifold. A complete evaluation of the origin of the transitions, forbidden and allowed, observed in the inhibitor spectra would require the collection of multiple-temperature and multiple-frequency data for spectral simulations, which was not preformed in this work.

The EPR spectra for the two inhibitors differ slightly from one another. A mononuclear signal arising from a forbidden transition is observed in the EPR spectrum upon coordination of the DIMP to the metal center, but is not observed with TEP. The absence of this forbidden transition suggests a less distorted metal center upon TEP binding indicating that this coordination between TEP and the metal is weaker than observed with DIMP. Another possibility is that the binding of TEP results in a metal coordination environment that is closer to octahedral symmetry than observed for DIMP. Consistent with an expected difference, the crystal structures for these two inhibitors complexed with PTE reveal the oxygen from TEP to be 1 Å further from the β-metal than DIMP (*47*). The sensitivity of EPR is demonstrated in the differentiation between the coordination of the two inhibitors.

Only one change was observed in the EPR spectrum of Mn/Mn-PTE upon addition of reaction product, diethyl phosphate (DEP). The binding of product could not be confirmed, but the presence of DEP significantly reduced the amount of hydroxyl bridge present. The loss of the hydroxyl bridge was identified by a reduction of binuclear signal and appearance of mononuclear signal. The effect on the bridge observed for both inhibitor and product provides a valuable insight into the influence of binding on the stability of the bridged species. These data suggest that substrate and inhibitors both shift the equilibrium in PTE toward the non-bridged species. The loss of

coordination of the bridge at one of the metals would increase the nucleophilic character of the hydroxyl while sustaining close proximity of the hydroxide to substrate.

The third interest of this work is the inactive Fe(II)-substituted PTE. The roles of the metals have been identified as generation of the bridging hydroxide, substrate binding, and positioning of two within close proximity to one another for ease of nucleophilic attack by the hydroxyl bridge. While Zn(II) is the native metal and the metal with the greatest affinity for the active site, it is Co(II)-substituted PTE that exhibits the highest activity (*10*). Zn(II), Co(II), Mn(II), Ni(II), and Cd(II) exhibit catalytic efficiencies that approach the diffusion controlled limit and rates for substrate turnover that are 10^3 s^{-1} or higher (*10*). However, Fe(II)- and Cu(II)-substituted PTE have been found to be inactive (*10, 54*). In this work the activity of Fe/Fe-PTE was accessed under anaerobic conditions as well as the binding of Fe(II) to the enzyme.

While PTE was found to bind up to two equivalent Fe(II) per active site, significant increase in activity due to Fe(II) binding was not observed. While metal selectivity may be expected to be based on availability and electronic attributes such as charge, redox potential, and size, comparison of the aforementioned metals gives no outstanding attribute that characterizes the selection of activating metals by PTE. It is not obvious why Fe(II) or Cu(II) are set apart from the five other transition metals that so readily activate PTE. This work rules out insufficient metal binding or oxidation to Fe(III) as potential reasons for lack of activity in Fe(II)-PTE.

This work has established that a hydroxyl bridge facilitates the exchange coupling between the two metals in PTE and is the species protonated at low pH that results in decreased catalytic activity. The use of EPR has also confirmed that inhibitor binding occurs at the metal center and results in a shift towards a non-bridged species. This change is proposed to reflect a weakening of the hydroxyl-metal bond at one metal

which would result in a stronger nucleophile for hydrolytic attack of substrate. This result is also observed for the active site with product present.

REFERENCES

1. Organophosphate pesticides in food A primer on reassessment of residue limits, (Accessed on 2005) www.epa.gov/pesticides/op/primer.htm.
2. Moore, D. H., Clifford, C. B., Crawford, I. T., Cole, G. M., and Baggett, J. M. (1995) Review of nerve agent inhibitors and reactivators of acetylcholinesterase, in *Enzymes of the Cholinesterase Family*, (Quinn, D. M., Ed.), Plenum Press, New York.
3. Raushel, F. M. (2002) Bacterial detoxification of organophosphate nerve agents, *Curr Opin Microbiol 5*, 288-295.
4. Munnecke, D. M. (1976) Enzymatic hydrolysis of organophosphate insecticides, a possible pesticide disposal method, *Applied and Environmental Microbiology 32*, 7-13.
5. Benning, M. M., Shim, H., Raushel, F. M., and Holden, H. M. (2001) High resolution X-ray structures of different metal-substituted forms of phosphotriesterase from *Pseudomonas diminuta*, *Biochemistry 40*, 2712-2722.
6. Benning, M. M., Hong, S. B., Raushel, F. M., and Holden, H. M. (2000) The binding of substrate analogs to phosphotriesterase, *J. Biol. Chem. 275*, 30556-60.
7. Vanhooke, J. L., Benning, M. M., Raushel, F. M., and Holden, H. M. (1996) Three-dimensional structure of the zinc-containing phosphotriesterase with the bound substrate analog diethyl 4-methylbenzylphosphonate, *Biochemistry 35*, 6020-5.
8. Omburo, G. A., Kuo, J. M., Mullins, L. S., and Raushel, F. M. (1992) Characterization of the zinc binding site of bacterial phosphotriesterase, *J. Biol. Chem. 267*, 13278-83.

9. Shim, H., and Raushel, F. M. (2000) Self-assembly of the binuclear metal center of phosphotriesterase, *Biochemistry 39*, 7357-64.

10. Omburo, G. A., Kuo, J. M., Mullins, L. S., and Raushel, F. M. (1992) Characterization of the zinc binding site of bacterial phosphotriesterase, *J Biol Chem 267*, 13278-13283.

11. Omburo, G. A., Mullins, L. S., and Raushel, F. M. (1993) Structural characterization of the divalent cation sites of bacterial phosphotriesterase by ^{113}Cd NMR spectroscopy, *Biochemistry 32*, 9148-55.

12. Dismukes, G. C. (1996) Manganese enzymes with binuclear active sites, *Chem Rev 96*, 2909-2926.

13. Aubert, S. D., Li, Y., and Raushel, F. M. (2004) Mechanism for the hydrolysis of organophosphates by the bacterial phosphotriesterase, *Biochemistry 43*, 5707-15.

14. Lewis, V. E., Donarski, W. J., Wild, J. R., and Raushel, F. M. (1988) Mechanism and stereochemical course at phosphorus of the reaction catalyzed by a bacterial phosphotriesterase, *Biochemistry 27*, 1591-7.

15. Donarski, W. J., Dumas, D. P., Heitmeyer, D. P., Lewis, V. E., and Raushel, F. M. (1989) Structure-activity relationships in the hydrolysis of substrates by the phosphotriesterase from *Pseudomonas diminuta*, *Biochemistry 28*, 4650-5.

16. Caldwell, S. R., Newcomb, J. R., Schlecht, K. A., and Raushel, F. M. (1991) Limits of diffusion in the hydrolysis of substrates by the phosphotriesterase from *Pseudomonas diminuta*, *Biochemistry 30*, 7438-44.

17. Kuo, J. M., and Raushel, F. M. (1994) Identification of the histidine ligands to the binuclear metal center of phosphotriesterase by site-directed mutagenesis, *Biochemistry 33*, 4265-72.

18. Dumas, D. P., and Raushel, F. M. (1990) Chemical and kinetic evidence for an essential histidine in the phosphotriesterase from *Pseudomonas diminuta*, *J. Biol. Chem. 265*, 21498-503.

19. Hong, S. B., and Raushel, F. M. (1999) Stereochemical constraints on the substrate specificity of phosphotriesterase, *Biochemistry 38*, 1159-65.

20. Chen-Goodspeed, M., Sogorb, M. A., Wu, F., Hong, S. B., and Raushel, F. M. (2001) Structural determinants of the substrate and stereochemical specificity of phosphotriesterase, *Biochemistry 40*, 1325-1331.

21. Chen-Goodspeed, M., Sogorb, M. A., Wu, F., and Raushel, F. M. (2001) Enhancement, relaxation, and reversal of the stereoselectivity for phosphotriesterase by rational evolution of active site residues, *Biochemistry 40*, 1332-1339.

22. Wilcox, D. E. (1996) Binuclear metallohydrolases, *Chem. Rev. 96*, 2435-2458.

23. Samples, C. R., Howard, T., Raushel, F. M., and DeRose, V. J. (2005) Protonation of the Binuclear Metal Center within the Active Site of Phosphotriesterase, *Biochemistry 44*, 11005-13.

24. Pierce, B. S., Elgren, T. E., and Hendrich, M. P. (2003) Mechanistic implications for the formation of the diiron cluster in ribonucleotide reductase provided by quantitative EPR spectroscopy, *J. Am. Chem. Soc. 125*, 8748-59.

25. Khangulov, S. V., Sossong, T. M., Jr., Ash, D. E., and Dismukes, G. C. (1998) L-arginine binding to liver arginase requires proton transfer to gateway residue His141 and coordination of the guanidinium group to the dimanganese(II,II) center, *Biochemistry 37*, 8539-50.

26. Benini, Rypniewski, Wilson, Ciurli, and Mangani. (2001) Structure-based rationalization of urease inhibition by phosphate: novel insights into the enzyme mechanism, *Journal of Biological Inorganic Chemistry 6*, 778-790.

27. Voegtli, W. C., White, D. J., Reiter, N. J., Rusnak, F., and Rosenzweig, A. C. (2000) Structure of the bacteriophage lambda Ser/Thr protein phosphatase with sulfate ion bound in two coordination modes, *Biochemistry 39*, 15365-74.

28. Porter, T. N., Li, Y., and Raushel, F. M. (2004) Mechanism of the dihydroorotase reaction, *Biochemistry 43*, 16285-92.

29. Shin, H., Evis, C., and Christianson, D. W. (2004) Design of amino acid aldehydes as transition-state analogue inhibitors of arginase, *J. Am. Chem. Soc. 126*, 10278-10284.

30. Thoden, J. B., Phillips, G. N., Jr., Neal, T. M., Raushel, F. M., and Holden, H. M. (2001) Molecular structure of dihydroorotase: a paradigm for catalysis through the use of a binuclear metal center, *Biochemistry 40*, 6989-6997.

31. Khangulov, S. V., Pessiki, P. J., Barynin, V. V., Ash, D. E., and Dismukes, G. C. (1995) Determination of the metal ion separation and energies of the three lowest electronic states of dimanganese (II,II) complexes and enzymes: catalase and liver arginase, *Biochemistry 34*, 2015-25.

32. Reczkowski, R. S., and Ash, D. E. (1992) EPR evidence for binuclear Mn(II) centers in rat liver arginase, *J. Am. Chem. Soc. 114*, 10992-10994.

33. Christianson, D. W. (1997) Structural chemistry and biology of manganese metalloenzymes, *Prog. Biophys. Molec. Biol. 67*, 217-252.

34. Jabri, E., and Karplus, P. A. (1996) Structures of the *Klebsiella aerogenes* urease apoenzyme and two active-site mutants, *Biochemistry 35*, 10616-10626.

35. Smoukov, S. K., Quaroni, L., Wang, X., Doan, P. E., Hoffman, B. M., and Que, L., Jr. (2002) Electron-nuclear double resonance spectroscopic evidence for a hydroxo-bridge nucleophile involved in catalysis by a dinuclear hydrolase, *J. Am. Chem. Soc. 124*, 2595-603.

36. Averill, B. A., Davis, J. C., Burman, S., Zirino, T., Sanders-Loehr, J., Loehr, T. M., Sage, J. T., and Debrunner, P. G. (1987) Spectroscopic and magnetic studies of the purple acid phosphatase from bovine spleen, *J. Am. Chem. Soc. 109*, 3760-3767.

37. Merkx, M., Pinkse, M. W. H., and Averill, B. A. (1999) Evidence for nonbridged coordination of *p*-nitrophenyl phosphate to the dinuclear Fe(III)-M(II) center in bovine spleen purple acid phosphatase during enzymatic turnover, *Biochemistry 38*, 9914-9925.

38. Copik, A. J., Nocek, B. P., Swierczek, S. I., Ruebush, S., Jang, S. B., Meng, L., D'Souza V, M., Peters, J. W., Bennett, B., and Holz, R. C. (2005) EPR and X-ray crystallographic characterization of the product-bound form of the MnII-loaded methionyl aminopeptidase from *Pyrococcus furiosus*, *Biochemistry 44*, 121-9.

39. Bennett, B., and Holz, R. C. (1997) EPR studies on the mono- and dicobalt(II)-substituted forms of the aminopeptidase from *aeromonas proteolytica*. Insight into the catalytic mechanism of dinuclear hydrolases, *J. Am. Chem. Soc. 119*, 1923-1933.

40. Rusnak, F., Yu, L., Todorovic, S., and Mertz, P. (1999) Interaction of bacteriophage lambda protein phosphatase with Mn(II): evidence for the formation of a $[Mn(II)]_2$ cluster, *Biochemistry 38*, 6943-52.

41. White, D. J., Reiter, N. J., Sikkink, R. A., Yu, L., and Rusnak, F. (2001) Identification of the high affinity Mn^{2+} binding site of bacteriophage lambda

phosphoprotein phosphatase: effects of metal ligand mutations on electron paramagnetic resonance spectra and phosphatase activities, *Biochemistry 40*, 8918-29.

42. Donarski, W. J., Dumas, D. P., Heitmeyer, D. P., Lewis, V. E., and Raushel, F. M. (1989) Structure-activity relationships in the hydrolysis of substrates by the phosphotriesterase from *Pseudomonas diminuta*, *Biochemistry 28*, 4650-4655.
43. Dumas, D. P., Caldwell, S. R., Wild, J. R., and Raushel, F. M. (1989) Purification and properties of the phosphotriesterase from *Pseudomonas diminuta*, *J. Biol. Chem. 264*, 19659-19665.
44. Li, W. S., Lum, K. T., Chen-Goodspeed, M., Sogorb, M. A., and Raushel, F. M. (2001) Stereoselective detoxification of chiral sarin and soman analogues by phosphotriesterase, *Bioorg. Med. Chem. 9*, 2083-2091.
45. Holm, L., and Sander, C. (1997) An evolutionary treasure: unification of a broad set of amidohydrolases related to urease, *Proteins 28*, 72-82.
46. Shim, H., and Raushel, F. M. (2000) Self-assembly of the binuclear metal center of phosphotriesterase, *Biochemistry 39*, 7357-7364.
47. Benning, M. M., Hong, S. B., Raushel, F. M., and Holden, H. M. (2000) The binding of substrate analogs to phosphotriesterase, *J. Biol. Chem. 275*, 30556-30560.
48. Lewis, V. E., Donarski, W. J., Wild, J. R., and Raushel, F. M. (1988) Mechanism and stereochemical course at phosphorus of the reaction catalyzed by a bacterial phosphotriesterase, *Biochemistry 27*, 1591-1597.
49. Antharavally, B. S., Poyner, R. R., and Ludden, P. W. (1998) EPR spectral evidence for a binuclear Mn(II) center in dinitrogenase reductase-activating glycohydrolase from *Rhodospirillum rubrum*, *J. Am. Chem. Soc. 120*, 8897-8898.

50. Kanyo, Z. F., Scolnick, L. R., Ash, D. E., and Christianson, D. W. (1996) Structure of a unique binuclear manganese cluster in arginase, *Nature 383*, 554-7.

51. Meier, A. E., Whittaker, M. M., and Whittaker, J. W. (1996) EPR polarization studies on Mn catalase from *Lactobacillus plantarum*, *Biochemistry 35*, 348-60.

52. Poyner, R. R., Cleland, W. W., and Reed, G. H. (2001) Role of metal ions in catalysis by enolase: an ordered kinetic mechanism for a single substrate enzyme, *Biochemistry 40*, 8009-17.

53. Chae, M. Y., Omburo, G. A., Lindahl, P. A., and Raushel, F. M. (1993) Antiferromagnetic coupling in the binuclear metal cluster of manganese-substituted phosphotriesterase, *J. Am. Chem. Soc. 115*, 12173-12174.

54. Chae, M. Y., Omburo, G. A., Lindahl, P. A., and Raushel, F. M. (1995) Utilization of copper as a paramagnetic probe for the binuclear metal center of phosphotriesterase, *Arch. Biochem. Biophys. 316*, 765-772.

55. Meister, A., Ed. (1982) *Methods in Enzymology*, Vol. 87, pp 390-405, John Wiley & Sons, Inc., New York.

56. Khangulov, S. V., Barynin, V. V., Voevodskaya, N. V., and Grebenko, A. I. (1990) ESR spectroscopy of the binuclear cluster of manganese ions in the active center of manganese-catalase from *Thermus thermophilus*, *Biochim. Biophys. Acta 1020*, 305-310.

57. Un, S., Dorlet, P., Voyard, G., Tabares, L. C., and Cortez, N. (2001) High-field EPR characterization of manganese reconstituted superoxide dismutase from *Rhodobacter capsulatus*, *J. Am. Chem. Soc. 123*, 10123-4.

58. Clark, P. A., and Wilcox, D. E. (1989) Magnetic properties of the nickel enzymes urease, nickel-substituted carboxypeptidase A, and nickel-substituted carbonic anhydrase, *Inorg. Chem. 28*, 1326-1333.

59. Larsen, T. M., Wedekind, J. E., Rayment, I., and Reed, G. H. (1996) A carboxylate oxygen of the substrate bridges the magnesium ions at the active site of enolase: structure of the yeast enzyme complexed with the equilibrium mixture of 2-phosphoglycerate and phosphoenolpyruvate at 1.8 Å resolution, *Biochemistry 35*, 4349-58.

60. Fox, B., Hendrich, M. P., Surerus, K. K., Andersson, K. K., Froland, W. A., Lipscomb, J. D., and Munck, E. (1993) Mössbauer, EPR, and ENDOR studies of the hydroxylase and reductase components of methane monooxygenase from *Methylosinus trichosporium* OB3b, *J. Am. Chem. Soc. 115*, 3688-3701.

61. Davydov, R., Kuprin, S., Graslund, A., and Ehrenberg, A. (1994) Electron paramagnetic resonance study of the mixed-valent diiron center in *Escherichia coli* ribonucleotide reductase produced by reduction of radical free protein R2 at 77 K, *J. Am. Chem. Soc. 116*, 11120-11128.

62. Wieghardt, K. (1989) The active sties in manganese-containing metalloproteins and inorganic model complexes, *Angew. Chem., Int. Ed. Engl. 28*, 1153-1172.

63. Weihe, H., and Gudel, H. U. (1997) Quantitative interpretation of the goodenough-kanamori rules: a critical analysis, *Inorg. Chem. 36*, 3632-3639.

64. Hotzelmann, R., Wieghardt, K., Florke, U., Haupt, H. J., Weatherburn, D. C., Bonvoisin, J., Blondin, G., and Girerd, J. J. (1992) Spin exchange coupling in asymmetric heterodinuclear complexes containing the μ-oxo-bis(μ-acetato)dimetal core, *J. Am. Chem. Soc. 114*.

65. Brunold, T. C., Gamelin, D. R., and Solomon, E. I. (2000) Excited-state exchange coupling in bent Mn(III)-O-Mn(III) complexes: dominance of the π/σ superexchange pathway and its possible contributions to the reactivates on binuclear metalloproteins, *J. Am. Chem. Soc. 122*, 8511-8523.

66. Delfs, C. D., and Stranger, R. (2000) Magnetic exchange in $[Mn_2(\mu\text{-}O)_3(tmtacn)_2]^{2+}$: metal-metal bonding or superexchange?, *Inorg. Chem. 39*, 491-5.

67. Reed, G. H., and Markham, G. D. (1984) *Biological Magnetic Resonance*, Vol. 6, Plenum Press, New York.

68. Ruiz, E., Alemany, P., Alvarez, S., and Cano, J. (1997) Structural modeling and magneto-structural correlations for hydroxo-bridged copper(II) binuclear complexes, *Inorg. Chem. 36*, 3683-3688.

69. Bossek, U., and Wieghardt, K. (1989) Bioinorganic model complexes for the active-site in manganese containing catalases – the crystal structures of $[L_2Mn^{II}{}_2(\mu\text{-}OH)(\mu\text{-}O_2CCH_3)_2](PF_6)\cdot CH_3OH$ and $\{L'_2Mn^{III}{}_2(\mu\text{-}O)(\mu\text{-}O_2CCH_3)_2](I_3)I\cdot H_2O$, *Inorg. Chem. 31*, 21-26.

70. Sakiyama, H., Tamaki, H., Kodera, M., Matsumoto, N., and Okawa, H. (1993) Dinuclear manganese (II) complexes of 2,6-bis[2-(dialkylamino)-ethyliminomethyl]-4-methylphenolate(l-)-synthesis, structure, and magnetism, *J. Chem. Soc., Dalton Trans.*, 591-595.

71. Caneschi, A., Ferraro, F., Gatteschi, D., Chiaro Melandui, M., Rey, P., and Sessoli, R. (1989) Synthesis, structure, and magnetic properties of a dinuclear manganese (II) complex with one μ-aqua and 2 μ-carboxylato bridges, *Angew. Chem., Int. Ed. Engl. 28*, 1365.

72. Bogumil, R., Kappl, R., Huttermann, J., Sudfeldt, C., and Witzel, H. (1993) X- and Q-band EPR studies on the two Mn^{2+}-substituted metal-binding sites of D-xylose isomerase, *Eur. J. Biochem. 213*, 1185-92.

73. Adams, H., Bailey, N. A., Debaecker, N., Fenton, D. E., Kanda, W., Latour, J.-M., Okawa, H., and Sakiyama, H. (1995) A dinuclear (μ-carboxylato)manganese(II) complex derived from a macrocyclic ligand: a structural model for active sites in natural systems, *Angew. Chem. Int. Ed. Engl.*, 2535-2537.

74. van Albada, G. A., Mohamadou, A., Driessen, W. L., de Gelder, R., Tanase, S., and Reedijk, J. (2004) A dinuclear Mn(II) chloro-bridged compound with a weak ferromagnetic Mn-Mn interaction synthesis, structure, EPR, and magnetism of $[Mn(\mu\text{-}Cl)(2,2'\text{-bi-imidazoline})_2]_2Cl_2$, *Polyhedron 23*, 2387-2391.

75. Krauss, M. (2001) *Ab initio* structure of the active site of phosphotriesterase, *J. Chem. Inf. Comput. Sci. 41*, 8-17.

76. Zheng, F., Zhan, C.-G., and Ornstein, R. L. (2002) Theoretical determination of two structural forms of the active site in cadmium-containing phosphotriesterases, *J. Phys. Chem. B 106*, 717-722.

77. Omburo, G. A., Mullins, L. S., and Raushel, F. M. (1993) Structural characterization of the divalent cation sites of bacterial phosphotriesterase by ^{113}Cd NMR spectroscopy, *Biochemistry 32*, 9148-9155.

78. Sivaraja, M., Stouch, T. R., and Dismukes, G. C. (1992) Solvent structure around cations determined by ^{1}H ENDOR spectroscopy and molecular dynamics simulation, *J. Am. Chem. Soc. 114*, 9600-9602.

79. Blanchard, S., Blain, G., Riviere, E., Nierlich, M., and Blondin, G. (2003) Temperature dependence of X- and Q-band EPR spectra of the dinuclear

manganese(II) complex $[(NO_2Bpmp)Mn_2(\mu\text{-}OAc)_2]^+$: determination of the exchange constant and of the spin parameters for the S=1, 2, and 3 spin states, *Chem. Eur. J. 9*, 4260-8.

80. Hong, S. B., and Raushel, F. M. (1997) Inhibitors directed towards the binuclear metal center of phosphotriesterase, *J. Enzyme Inhib. 12*, 191-203.

81. Vanhooke, J. L., Benning, M. M., Raushel, F. M., and Holden, H. M. (1996) Three-dimensional structure of the zinc-containing phosphotriesterase with the bound substrate analog diethyl 4-methylbenzylphosphonate, *Biochemistry 35*, 6020-6025.

82. Benning, M. M., Kuo, J. M., Raushel, F. M., and Holden, H. M. (1994) Three-dimensional structure of phosphotriesterase: an enzyme capable of detoxifying organophosphate nerve agents, *Biochemistry 33*, 15001-15007.

83. Golombek, A. P., and Hendrich, M. P. (2003) Quantitative analysis of dinuclear manganese(II) EPR spectra, *J. Magn. Reson. 165*, 33-48.

84. Pierce, B. S., and Hendrich, M. P. (2005) Local and global effects of metal binding within the small subunit of ribonucleotide reductase, *J. Am. Chem. Soc. 127*, 3613-23.

85. Reiter, N. J., White, D. J., and Rusnak, F. (2002) Inhibition of bacteriophage lambda protein phosphatase by organic and oxoanion inhibitors, *Biochemistry 41*, 1051-9.

86. Cama, E., Emig, F. A., Ash, D. E., and Christianson, D. W. (2003) Structural and functional importance of first-shell metal ligands in the binuclear manganese cluster of arginase I, *Biochemistry 42*, 7748-58.

87. Jackson, C., Kim, H. K., Carr, P. D., Liu, J. W., and Ollis, D. L. (2005) The structure of an enzyme-product complex reveals the critical role of a terminal

hydroxide nucleophile in the bacterial phosphotriesterase mechanism, *Biochim. Biophys. Acta 1752*, 56-64.

88. Klabunde, T., Strater, N., Frohlich, R., Witzel, H., and Krebs, B. (1996) Mechanism of Fe(III)-Zn(II) purple acid phosphatase based on crystal structures, *J. Mol. Biol. 259*, 737-48.

89. Guddat, L. W., McAlpine, A. S., Hume, D., Hamilton, S., de Jersey, J., and Martin, J. L. (1999) Crystal structure of mammalian purple acid phosphatase, *Structure Fold. Des. 7*, 757-67.

90. Lindqvist, Y., Johansson, E., Kaija, H., Vihko, P., and Schneider, G. (1999) Three-dimensional structure of a mammalian purple acid phosphatase at 2.2 Å resolution with a mu-(hydr)oxo bridged di-iron center, *J. Mol. Biol. 291*, 135-47.

91. Cotton, F. A., and Wilkinson, G. (1988) *Advanced Inorganic Chemistry*, 5th ed., Wiley, New York.

92. Pearson, R. G. (1963) Hard and soft acids and bases, *J. Am. Chem. Soc. 85*, 3533-3539.

93. Tshuva, E. Y., and Lippard, S. J. (2004) Synthetic models for non-heme carboxylate-bridged diiron metalloproteins: strategies and tactics, *Chem. Rev. 104*, 987-1012.

94. Holm, R. H., Kennepohl, P., and Solomon, E. I. (1996) Structural and functional aspects of metal sites in biology, *Chem. Rev. 96*, 2239-2314.

95. Schilling, O., Wenzel, N., Naylor, M., Vogel, A., Crowder, M., Makaroff, C., and Meyer-Klaucke, W. (2003) Flexible metal binding of the metallo-β-lactamase domain: glyoxalase II incorporates iron, manganese, and zinc in vivo, *Biochemistry 42*, 11777-11786.

96. Whittington, D. A., and Lippard, S. J. (2001) Crystal structures of the soluble methane monooxygenase hydroxylase from *Methylococcus capsulatus (Bath)* demonstrating geometrical variability at the dinuclear iron active site, *J. Am. Chem. Soc. 123*, 827-38.

97. Stenkamp, R. E. (1994) Dioxgen and hemerythrin, *Chem. Rev. 94*, 715-726.

98. Estiu, G., and Mertz, K. M. (2004) Enzymatic catalysis of urea decomposition: elimination or hydrolysis?, *J. Am. Chem. Soc. 126*, 11832-11842.

99. Park, I., and Hausinger, R. P. (1996) Metal ion interactions with urease and ured-urease apoprotein, *Biochemistry 35*, 5345-5352.

100. Hellerman, L. A., and Perkins, M. E. (1935) Activation of enzymes III. The role of metal ions in the activation of arginase. The hydrolysis of arginine induced by certain metal ions with urease, *J. Biol. Chem. 112*, 175-194.

VITA

Cynthia Renee Samples received her B.S. in chemistry from Harding University in May of 1999. She began her graduate career in chemistry at Texas A&M University in the fall of 1999. She later joined the DeRose research group in the summer of 2000 and began collaborative work with the Raushel research group in the fall of 2000. She received her Ph.D. in chemistry from Texas A&M University in December 2005. Her permanent address is in the care of Dr. Frank Raushel at Texas A&M University, Department of Chemistry, mail stop 3255, College Station, TX 77843.